UNIVERSITY OF OKLAHOMA

GRADUATE COLLEGE

# THE UNIQUE GEOMETRIES AND ILLUMINATIONS OF PROTOPLANETARY DISKS AND THEIR POTENTIAL EXOPLANETS

A DISSERTATION

SUBMITTED TO THE GRADUATE FACULTY

in partial fulfillment of the requirements for the

Degree of

DOCTOR OF PHILOSOPHY

By

Evan A. Rich
Norman, Oklahoma
2019

THE UNIQUE GEOMETRIES AND ILLUMINATIONS OF
PROTOPLANETARY DISKS AND THEIR POTENTIAL EXOPLANETS

A DISSERTATION APPROVED FOR THE
HOMER L. DODGE DEPARTMENT OF PHYSICS AND ASTRONOMY

BY

Dr. John Wisniewski, Chair

Dr. Nathan Kaib

Dr. Kieren Mullen

Dr.Michael Sitko

Dr. Kerry Magruder

To my Mom and Dad who first inspired me to investigate the natural world around me and gave me the resources to succeed.

And to my wife Sarah who makes all of this all worth while.

# Acknowledgements

Much of the work in this dissertation could not have been done without the native Hawaiian's sharing their island and mountain with the astronomical community. I would like to recognize the significant cultural role and reverence that the summit of Maunakea has always had within the indigenous Hawaiian community. I am most fortunate to have the opportunity to conduct astronomical observations from their mountain.

This work was performed as part of the larger SEEDS project. Specifically, I would like to acknowledge help from Dr. Thayne Currie, Dr. Misato Fukagawa, Dr. Carol Grady, Dr. Jun Hashimoto, Dr. Micheal Sitko, and Dr. John Tobin.

And finally I would like to acknowledge my advisor Dr. John Wisniewski who has worked tirelessly to ensure I had every opportunity to succeed.

# Table of Contents

# List of Tables

# List of Figures

# Abstract

The discovery of new protoplanetary disk structures can help reveal the dynamics of the young planetary systems and potentially point to planet formation within the disk. In my dissertation, I present investigations of three stellar/substellar systems; DoAr 28, VHS J125601.92-125723.9 (VHS 1256), and HD 163296. First, I will discuss the first near-IR scattered light detection of the protoplanetary disk around DoAr 28. I modeled both the observed SED and H-band PI imagery of the system and found that our best fit models have a partially depleted inner gap from the dust sublimation radius out to ∼8 au. Second, I present and analyze Subaru/IRCS $L'$ and $M'$ images of the nearby M dwarf VHS 1256, which was recently claimed to have a ∼11 $M_J$ companion (VHS 1256 b). I found that the central star is a binary and conclude that VHS 1256 is most likely a very low mass (VLM) hierarchical triple system. Finally, I present Subaru/HiCIAO H-band imagery, Subaru/SCExAO near-IR imagery, and HST/STIS optical imagery of the protoplanetary disk around HD 163296. I demonstrate that the new Subaru/HiCIAO and HST/STIS imagery exhibits disk illumination variability on timescales $< 3$ months, possibly due to a non-axisymmetric distribution of dust clouds. show that our SCExAO/CHARIS observations fail to recover the previously identified 6–7 $M_{\rm J}$ planetary candidate. Additionally, I did not detect the predicted launch of a new HH-knot nor did I detect any of the previously observed HH-knots, suggesting a potential change in the jet of HD 163296.

# Chapter 1

# Introduction

## 1.1 Protoplanetary Disks

Protoplanetary disks are material around protostellar stars that are composed of optically thick dust and gas. The exact shape of the dust and gas evolves with time, but typically it consists of a disk rotating at keplerian velocities around the star and the disk scale height above the mid-plane increases with radius causing a flared shape. Planets form within these disks, thus by studying the disks themselves we can learn more about the planet formation process. Protoplanetary disks evolve from high density interstellar medium (ISM) material to debris disks systems such as our own Solar System. The disks themselves form from the collapse of the giant molecular cloud are a consequence of conservation of angular momentum. The disks are composed initially of gas and ISM dust grains originating in a giant molecular cloud. The molecular cloud collapses to form the protostar and disk which is fed by an accreting envelope around the star. Material from the disk accretes onto the star due to internal friction in the disk, and due to the conservation of angular momentum, some material is ejected through outflows (e.g., jets, Herbig-Haro Knots).

The evolution of protoplanetary disks is diagramed in Figure 1.1, reproduced from Figure 6 in Williams & Cieza (2011). Once the disk has formed from the collapse of the giant molecular cloud, the disk takes a flared shape that extendes from the sublimation radius from the star to 100's of AU as shown in sub-figure a) of Figure 1.1. At this stage shown in the sub-figure, material is accreting onto the star, flux from the star is causing evaporative flow, and the dust particles in the

disk are ISM size dust grains. As the disk evolves, the dust coagulates forming larger and larger dust grains which settle to the mid-plane of the disk as shown in sub-figure b) of Figure 1.1. Eventually, accretion will cease and gaps will appear in the disk which are possible signs of planet formation. Finally, light from the star will photoevaporate the disk (sub-figure c) in Figure 1.1) leaving only the larger processed dust grains and planets as a debris disk (sub-figure d) in Figure 1.1).

Classification of protoplanetary disks is typically done by their spectral energy distribution (SED) which roughly denotes their evolutionary status ranging from class 0 to class III disks. Primarily, they are classified based on their spectral energy distribution (SED) in the near-IR, though classification in the radio can also occur (Williams & Cieza, 2011). For Class 0 disks, most of systems mass is part of the accreting envelope where the dust and gas is still in-falling on to the disk and the central protostar. There is no optical flux but strong near-IR and radio emission from the dusty envelope and disk. Next, the systems evolve into class I disks where the protostars have formed and its mass is $>$ the envelope mass and the disk mass. The SED consists of a blackbody from the protostar and strong IR and radio emission from the disk and envelope. Class I disks last 0.5 Myr (Evans et al., 2009). Class II young stellar objects (YSO's) are where the $M_{disk}/M_{star}$ 1% and the envelope has either been accreted or dissipated. I will primarily discuss this evolutionary stage of protoplanetary disks in this work. After the embedded phase, the disk lifetime is approximately 2-3 Myrs depending on the spectral type of the star (Williams & Cieza, 2011). Finally, there are Class III YSO's where the dust in the disk has been processed leaving only larger dust grains along the mid-plane. These are typically referred to as debris disks where the gas from the system has dissipated (Williams & Cieza, 2011). An interesting evolutionary period of protoplanetary disks are transitional disks, first classified

by the Infrared Astronomical Satellite (IRAS), that exhibit little to no near-IR ($< 10\ \mu m$) excess above the blackbody of the star but still show significant excess above the blackbody of the star beyond 10 $\mu m$ (Strom et al., 1989c; Wolk & Walter, 1996). Followup imaging campaigns have verified that the lower near-IR excess is due to radial gaps in the disk (Marsh et al., 1995). The causes of these gaps remain unknown and still is an element of much investigation.

A variety of mechanisms cause the observed evolution of protoplanetary disks. The ultimate death of protoplanetary disks is through photo-evaporation (Clarke et al., 2001) where FUV, EUV, and X-ray's from the central source push the dust and gas of the system away of the illuminated sides of the disk. The small dust grains coagulate together and form larger dust larger grains, which the process is referred to as grain-growth (Dullemond & Dominik, 2005). This process will eventually lead to planetesimals and the formation of planets, which is discussed further in section 1.2. These larger dust grains settle to the mid-plane of the disk causing stratification with larger dust grains at the mid-plane of the disk and smaller (e.g., ISM dust grains) at the surface of the disk. Finally, the forming planets themselves can affect the disk by inducing spiral density waves, gaps and rings in the disk (Zhu et al., 2011). The latter has most famously been seen through the advent of high-resolution sub-mm imaging with Atacama Large Millimeter/submillimeter Array (ALMA) with images of protoplanetary disks such as TW Hydrae (Andrews et al., 2016) and HD 163296 (Isella et al., 2018). While there has been a large amount of theoretical and modeling work done to help explain how planets can create these rings in protoplanetary disks, directly imaging a planet within one of these gaps has remained elusive. There have been a variety of claims of a planetary detection within a gap (e.g., LaKl 15 b; Thalmann et al. 2016, PDS 70 b; Keppler et al. 2018, HD 163296 b; Guidi et al. 2018), however

many of these observations have been disputed by follow-up observations. Discovery of more planetary objects within gaps are needed to determine the effect the planet has on the disk and vice versa.

Several direct imaging studies have been performed looking at young exoplanets and/or the protoplanetary disks around the stars (VLT/NACO; Nielsen et al. 2008, Gemini/NICI; Biller et al. 2013; Nielsen et al. 2013; Gemini/GPI; (Macintosh et al., 2014), VLT/SPHERE; (Beuzit et al., 2008; Vigan et al., 2016)). One of the most recent planet and disk imaging surveys to finish is the Strategic Exploration of Exoplanets and Disks with Subaru (SEEDS) survey (Tamura , 2009; Tamura, 2016), which primarily used the near-IR scattered light imager HiCIAO (Hodapp et al., 2008) mounted on the Subaru telescope. Several protoplanetary disks in the survey were imaged including AB Aur (Hashimoto et al., 2011) with its spiral arm structures, HD 142527 (Fukagawa et al., 2006), and LkCa 15 (Thalmann et al., 2010) with its very complicated disk structure. The plethora of disk structure can be extrapolated to indicate planet formation (Takami et al., 2014; Tamura, 2016).

## 1.2 Exoplanet Formation and Detection

One fundamental question that modern astronomy has yet to answer is how do planets form? A plethora of dedicated planet surveys have occurred over the years such as the those using the Kepler Space Telescope (Borucki et al., 2009, 2010, 2011) or the California Planet Search (Howard et al., 2010; Wright et al., 2011) resulting in more than $\sim$3,000 exoplanets known to date (exoplanets.org). Trends in the occurrence of these discovered planets have been identified. It has been found that Jovian-mass planets occur more often around A-dwarf stars than M-dwarf stars (Johnson et al., 2010). Additionally, there have been several notable trends

of planet occurrence and host star metallicity (Gonzalez, 1997; Fischer & Valenti, 2005). However, such surveys and subsequent investigations utilize the transit and radial velocity methods for detecting the existence of planets around these stars, which is currently biased towards low orbital separations. Direct imaging techniques allow us to investigate the occurrence of planets around close by stars at wider orbital separations and directly investigate their atmospheres. Additionally, these same techniques used to investigate the occurrence of planets at high orbital separations also allow us to investigate the dust and gas environment around young close by stars. Thus by studying close by, young stars, we can look for young exoplanets and investigate the interplay between the forming planets and the protoplanetary disk around the central host star. The SEEDS survey also investigated a number of brown dwarf and exoplanet discoveries including GJ 504 b (Kuzuhara et al., 2013), $\kappa$ And b (Carson et al., 2013), GJ 758 B (Thalmann et al., 2009), Pleiades HII 3441 b (Konishi et al., 2016), and ROXs 42B b (Currie et al., 2014a).

Giant planet formation is proposed to occur via one of two mechanisms. First, core accretion (Pollack et al., 1996) is where dust coagulates together in the midplane of the protoplanetary disk and grows from ISM size dust grains to km size planetesimals. Second, disk instability or gravitational instability (Boss, 2001), is a mechanism where the protoplanetary disk fragments and forms planets, similar to the star formation process. Due to coagulation of the dust in the core accretion mechanism, it is expected that systems with higher metalicity form more planets which have been seen for systems with planets at low orbital separation (e.g., Gonzalez 1997; Fischer & Valenti 2005). Currently, it is thought that when disk fragmentation does occur, it creates brown dwarf or stellar companions both well over the deuterium burning limit (Kratter & Lodato 2016 and citations therein).

## 1.3 Dissertation Summary

This dissertation contains a detailed investigation of three stellar/sub-stellar systems, DoAr 28, VHS 1256, and HD 163296, to better understand the formation of exoplanets and the environment. First, I present the scattered light detection of the protoplanetary disk around DoAr 28 in Chapter 2 which is reproduced by permission of the American Astronomical Society from the following publication: Rich, E. A., Wisniewski, J. P., Mayama, S., et al. 2015, AJ, 150, 86, "Near-IR Polarized Scattered Light Imagery of the DoAr 28 Transitional Dis". Next in Chapter 3, I will present the discovery of a new Hierarchical Triple System and evidence against a new exoplanet hosted by an M-dwarf. Chapter 3 is reproduced by permission of the American Astronomical Society from the following publication: Rich, E. A., Currie, T., Wisniewski, J. P., et al. 2016, ApJ, 830, 114, "Thermal Infrared Imaging and Atmospheric Modeling of VHS J125601.92-125723.9 b: Evidence for Moderately Thick Clouds and Equilibrium Carbon Chemistry in a Hierarchical Triple Syste". In Chapter 4 I will present comparisons of new Subaru/HiCIAO 2011 data of HD 163296 to other direct imaging epochs and show that the disk illumination varies on timescales $< 4$ years. Additionally, I will present evidence that a planetary candidate within HD 163296 is not real. Chapter 4 is reproduced by permission of the American Astronomical Society from the following publication: Rich, E. A., Wisniewski, J. P., Currie, T., et al. 2019, ApJ, Accepted, "The Time Variable Scattered Light Morphology of the HD 163296 Protoplanetary Disk". Finally, in Chapter 5 I will present new HST/STIS observations of HD 163296 and compare them to 1998 HST/STIS observations of the same object and show that the disk illumination varies even faster than previous observations ($< 3$ months). Additionally, we see no evidence of the jet associated with HD 163296 and we do not detect any new launches of HH-knots from HD

163296.

## 1.4 List of Abbreviations:

### 1.4.1 Telescopes, Instruments, and Organizations

- Advanced Camera for Surveys (ACS)
- American Association of Variable Star Observers (AAVSO)
- Apache Point Observatory (APO)
- ARC Echelle Spectrograph (ARCES)
- Atacama Large Millimeter/submillimeter Array (ALMA)
- Broad-band Array Spectrograph System (BASS)
- Coronagraphic High Angular Resolution Imaging Spectrograph (CHARIS)
- the Coronagraphic Imager with Adaptive Optics (CIAO)
- Gemini Planet Imager (GPI)
- High Contrast Instrument for the subaru next generation Adaptive Optics (HiCIAO)
- Hubble Space Telescope (HST)
- Infrared Telescope Facility (IRTF)
- Nasmyth Adaptive Optics System Near-Infrared Imager and Spectrograph (NaCo)
- Near-Infrared Cronoagraphic Imager (NICI)

- Space Telescope Instrument and Spectrograph (STIS)
- Spectro-Polarimetric High-contrast Exoplanet REsearch instrument (SPHERE)
- Strategic Exploration of Exoplanets and Disks with Subaru (SEEDS)
- Subaru Coronagraphic Extremem Adaptive Optics (SCExAO)
- Submillimeter Array (SMA)
- Vary Large Array (VLA)
- Very Large Telescope (VLT)

### 1.4.2 Astronomical Abbreviations

- Adaptive Optics (AO)
- Algorithms for Calibration, Optimization Registration, and Nulling the Star in Angular Differential Imaging (ACORNS-ADI)
- Angular Differential Imaging (ADI)
- Field of View (FOV)
- Full Width Half Max (FWHM)
- Herbig-Haro knot (HH-knot)
- Interstellar Medium (ISM)
- Laser Guide Star (LGS)
- Locally Optimized Combination of Images (LOCI)
- Monte Carlo Radiative Transfer (MCRT)

- Natural Guide Star (NGS)
- Point Spread Function (PSF)
- Polarized Intensity (PI)
- Position Angle (PA)
- quad Polarized Differential Imaging (qPDI)
- Signal to Noise (SN)
- Singular Value Decomposition (SVD)
- Spectral Differential Imaging (SDI)
- Spectral Energy Distribution (SED)
- standard Polarized Differential Imaging (sPDI)
- Very Low Mass (VLM)
- Young Stellar Object (YSO)

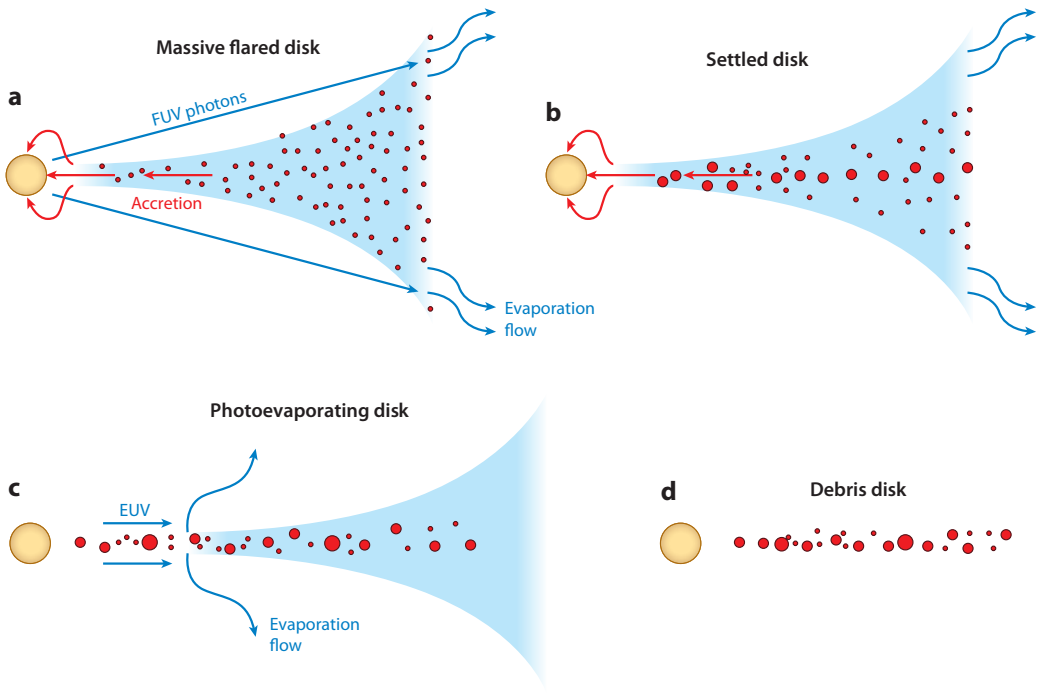


Fig. 1.1.— This diagram outlines the evolution of protoplanetary disks. Sub-figure a) (upper left) shows the disk after the collapse of the giant molecular cloud. The envelope around the system has dissipated, material is still accreting onto the star, and FUV photons from the star are causing an evaporative flow. Sub-figure b) (upper right) is a more evolved system than a) where the dust has begun coagulate together and the sub-sequent large dust grains settle to the mid-plane of the disk. Next in sub-figure c) (lower left) accretion has turned off and the inner disk is beginning to clear. Photons from the star are driving photoevaporation which will eventually destroy the disk. Finally, sub-figure d) (lower right) is a debris disk where the gas and small grain dust have been driven away from the system leaving only the larger processed grains and fully formed planets. This figure is reproduced from the following publication: Williams, J. P., & Cieza, L. A. 2011, ARA&A, 49, 67, "Protoplanetary Disks and Their Evolution".

# Chapter 2

# Near-IR Polarized Scattered Light Imagery of the DoAr 28 Transitional Disk

## 2.1 Introduction

Detailed observations of the spectral energy distributions (SEDs) of young stellar objects (YSOs) have revealed numerous systems with deficits of near-infrared flux compared to primordial YSOs. These pre-transitional and transitional disk systems are interpreted as having inner gaps and holes in their disks (Strom et al., 1989b; Espaillat et al., 2007a,b). Both infrared scattered light imagery (Fukagawa et al., 2006; Thalmann et al., 2010; Hashimoto et al., 2011; Canovas et al., 2013; Avenhaus et al., 2014) and sub-millimeter observations (Andrews et al., 2011; Bruderer et al., 2014; van der Marel et al., 2014) have confirmed this basic architecture for pre-transitional and transitional disk systems, and revealed additional sub-structure that could provide information about the mechanism responsible for clearing regions in these disks (van der Marel et al., 2014).

Numerous mechanisms have been suggested to explain the clearing and partial clearing associated with pre-transitional and transitional disk systems, including grain-growth (Dullemond & Dominik, 2005), photo-evaporation (Clarke et al., 2001), disk instability (Papaloizou, 2007), and perturbation from planetary companions (Zhu et al., 2011). These mechanisms can also influence other regions of these disks such as the inner walls and surface structures. For example, grain growth can create a rounded gap edge (Birnstiel et al., 2012) whereas planets can inflate gap edges, creating a wall that can shadow parts of the outer disk or induce significant back scattering (Jang-Condell & Turner, 2012, 2013). Grain growth

should also induce very bright sub-millimeter features in systems exhibiting gaps in the near-infrared, although this is not seen in Oph IRS 48 or SAO 206462 (Bruderer et al., 2014; Pérez et al., 2014). Additional morphological features such as spiral arms have been detected in these disks, and could be attributable to stellar and sub-stellar companions or gravitational instabilities (Bate et al., 2003). Planet-induced perturbations should co-rotate with the planet; hence, detecting the rotation of these structure could help to distinguish the origin of some disk structures (Hashimoto et al., 2011; Lomax et al., 2015). Additional morphological features observed in transitional disks, such as dust traps (Bruderer et al., 2014), can also be used to constrain the mechanism responsible for sculpting the spatial distribution of gas and dust in transitional disks. Clearly, a first step that is needed to assess the clearing mechanism is to fully constrain the spatial distribution of small and large dust grains, as well as the gas, in individual disk systems.

The spatial distribution of small dust grains in numerous transitional disks (Hashimoto et al., 2012; Muto et al., 2012; Grady et al., 2013; Follette et al., 2013; Kusakabe et al., 2012; Hashimoto et al., 2011; Thalmann et al., 2010; Tsukagoshi et al., 2014; Takami et al., 2013; Canovas et al., 2013; Avenhaus et al., 2014; Hashimoto et al., 2015) have been recently parametrized utilizing several facilities, including large programs like the Strategic Exploration of Exoplanets and Disks with Subaru (SEEDS) high-contrast imaging survey (Tamura , 2009). These observations have provided scattered light confirmation of the gapped nature of transitional disks (Thalmann et al., 2010), revealed the presence of spiral structures (Muto et al., 2012; Grady et al., 2013; Currie et al., 2014b), detected likely non-axisymmetric inner disks (Kusakabe et al., 2012; Takami et al., 2013), found differences in some cases about the distribution of large versus small dust grain populations (Hashimoto et al., 2012; Dong et al., 2012), and the presence of

a planet within a gap (Currie et al., 2014b).

DoAr 28 is a K5-type object in the $\rho$ Ophiuchi association located at a distance of $\sim$139 pc (Mamajedk, 2008), that has been identified as a transitional disk based on its SED (McClure et al., 2010; Kim et al., 2013). The system is observed to be actively accreting at a rate of $4 * 10^{-9}$ $\frac{M_{\odot}}{year}$ (Keane et al., 2014), and has a disk with an inferred outer gap radius of 15 AU (Kim et al., 2013) from analysis of its SED.

In this paper, we present the first scattered light detection of the DoAr 28 transitional disk, in the H-band. In Section 2, we will discuss the scattered light observations and data reduction. In Section 3, we present our analysis of the resolved disk, constrain the presence of co-moving point sources, and model these data using Monte Carlo models. Finally, we discuss the implications of our results in the broader context of other resolved transitional disk systems in Section 4.

## 2.2 Observations and Reductions

DoAr 28 was observed in two epochs on 2012 July 9 (2012 epoch) and 2014 June 9 (2014 epoch) as part of the SEEDS survey using HiCIAO (Hodapp et al., 2008) in the H-band. The data were obtained in quad Polarized Differential Imaging (qPDI) mode at four wave-plate positions (0°, 22.5°, 45°, 67.5°) in Angular Differential Imaging (ADI) mode. Each observational frame contains four sub-images with each sub-image having a field of view of 5.″0 by 5.″0, with a pixel scale of 9.5 mas pixel$^{-1}$ and a FWHM of 0.″136 for the 2012 epoch and 0.″101 for the 2014 epoch. The total ADI field rotation achieved was 19.5° for the 2012 epoch data and was 21.3° for the 2014 epoch data.

### 2.2.1 HiCIAO Data Reduction

The data reduction process we employed for extracting polarized intensity (PI) disk images utilized the double differencing reduction technique described in Hashimoto et al. (2011). To briefly review, the four sub-images of each frame contain two ordinary and two extra-ordinary images, which can be summed and subtracted from their 90° counterparts to create -Q, +Q, -U, and +U images. The Q and U frames were then rotated into a common orientation, corrected for instrumental polarization, and summed to create final Q and U images. Note that as our 2012 epoch imagery were obtained under non-optimal conditions, we only utilized the best 64 of the 76 observed frames for our summed imagery. The final PI images are computed using $PI = \sqrt{Q^2 + U^2}$. As previously noted by Hashimoto et al. (2012), the PSF convolved by seeing is not perfectly corrected by the AO-188 system, which produces a residual polarized halo. We computed an artificial halo following the procedure outlined in Hashimoto et al. (2012), scaled this to the observed aperture polarization of the system ($P = 0.869\% \pm 0.012\%$), and subtracted it from the PI image to create final PI imagery.

We searched for point-source companions to DoAr 28 using the ACORNS-ADI software package (Brandt et al., 2013). We treated each of the four sub-images noted above as its own angular differential imaging sequence (ADI, Marois et al. 2006) and reduced them using the LOCI algorithm (Lafreniere et al. 2007) with the standard reduction parameters from Brandt et al. (2013). This yielded four residual images, each corrected for partial flux subtraction. We then averaged these PSF-subtracted images to produce a single high-contrast image. We computed the standard deviation in annuli on this combined image to produce a contrast map and searched for $5\sigma$ companions. We found one companion candidate as described in Section 3.2; follow-up data showed it to be an unrelated

background star.

### 2.2.2 SMA Observations and Reduction

We observed DoAr 28 with the Submillimeter Array (SMA) on 2011 March 16, using the Compact Configuration with six of the 6 m diameter antennas at 230 GHz (1.3 mm) with a full correlator bandwidth of 2 GHz, for a total integration time of 63 minutes. Calibration of the visibility phases and amplitudes was achieved with observations of the quasar 3C 279, at intervals of about 20 minutes. Observations of Titan provided the absolute scale for the flux density calibration. The data were calibrated using the MIR software package.[a] We detected DoAr 28 with a flux density of 68.6±1.9 mJy. The double sideband system temperatures were 110 to 170 K.

### 2.2.3 APO Observations and Reduction

DoAr 28 was observed using the ARC Echelle Spectrograph (ARCES; Wang et al. 2003) at the Apache Point Observatory (APO) 3.5m telescope on 2014 June 19, yielding a R∼31,500 spectrum covering the spectral range of ∼3,600-10,000Å . The data were reduced using standard IRAF techniques. We extracted the order containing H$\alpha$ and continuum normalized these data, enabling us to characterize the line strength discussed in Section 2.3.3.

[a]http://www.cfa.harvard.edu/∼cqi/mircook.html

## 2.3 Analysis

### 2.3.1 Scattered Light Imagery

Our two epochs of scattered light PI imagery of DoAr 28 are shown in Figure 2.1. Significant scattered light around the central star is clearly seen in both epochs. The direction and relative intensity of the polarization vectors derived from these data exhibit a clear centrosymmetric behavior around the central star (Figure 2.2), confirming that this signal arises from scattering off of circumstellar material. These data exhibit less evidence of centro-symmetry about the minor axis, which is much less resolved than the major axis, suggesting that the level of our residual polarized halo correction might be incomplete. Our primary analysis of these data will focus on the measured polarized intensity along the major axis of the system.

Since these data were not observed with a coronagraph, we defined the effective inner working angle as the location where the radial profile measured along the disk major axis (Figure 2.3) exhibited a clear deviation from the disk dominated scattered light power law behavior seen in the outer disk. Using this criterion, we determined the inner working angle to be $0\farcs17$ (22 AU) for the 2012 epoch data and $0\farcs10$ (13 AU) for the 2014 epoch (Figure 2.4). The power law that characterizes the radial profile distribution of the scattered light flux along the disk major axis extends out to $\sim 0\farcs50$ (65 AU), defining the outer edge of the scattered light disk, before becoming clearly dominated by noise. The detected disk appears to be continuous, with no significant gaps or holes clearly visible. The two epochs of imagery appear similar to each other, modulo potential differences arising from the factor of 1.4 better FWHM achieved in the 2014 epoch imagery. For the imagery with a slightly larger FWHM, it is conceivable that a small amount of

disk flux could be spread out into the PSF halo, and be subtracted out in the process described in Section 2.2.1. Nevertheless, the overall surface brightness of the disk is the same at both epochs and the radial surface brightness power law measured along the major axis for both epochs is similar (-2.47 for 2012; -1.84 for 2014). We do note the potential presence of a slight curl in the SW region of the 2014 epoch scattered light disk, and further discuss this feature in Section 3.6

We determine the inclination of the disk to be $\sim 50^{\circ}$ (Table 4.2). This was found by subtracting a suite of disk models for a range of inclination angles, described in Section 2.3.3, and identifying the inclination which yielded the smallest residuals (Figure 2.5). Note that this residual image (Figure 2.5) exhibits clear deviations from axisymmetry, with a deficit of scattered light present along the northern side of the major axis. We will further discuss this non-axisymmetric structure in Section 3.6.

### 2.3.2 Point Source Detections

We identified a candidate point source companion $1\farcs08$ northwest of DoAr 28, with an $H$-band contrast of 9.5 magnitudes, in our July 2012 data. Our second epoch images from June 2014 indicate that this object is almost certainly a background star. DoAr 28 was too faint for a proper motion from the *Tycho* satellite, but is part of to the same star forming region as $\rho$ Oph. We assume that it shares $\rho$ Oph's proper motion of $(-5.5 \pm 0.9,\ -21.7 \pm 0.9)$ mas/yr in RA and Dec (van Leeuwen, 2007). At a distance of $\sim$140 pc, 1 mas/yr corresponds to $\sim$0.7 $\mathrm{km\,s^{-1}}$, similar to the velocity dispersions of the Hyades, Pleiades, and TW Hya (Perryman et al., 1998; Jones, 1970; Makarov & Fabricius, 2001), and somewhat less than the $\sim$2–3 $\mathrm{km\,s^{-1}}$ of Orion (Jones & Walker, 1988; Fűrész et al., 2008). Figure 6 shows that the companion candidate follows the expected background track assuming

common proper motion with $\rho$ Oph. If the point source were co-located with DoAr 28, their relative velocity would be at least 17 $\mathrm{km\,s^{-1}}$, much too high for the system to be bound at its observed location.

Figure 2.7 shows our sensitivity limits, assuming a distance of ∼140 pc and converting contrast to absolute magnitude, and neglecting extinction (estimated to be ∼0.4 magnitudes at H-band, using A(v) = 2.3 (McClure et al., 2010), $R_v$ = 3.1, and the Cardelli, Clayton, & Mathis (1989) extinction relations), making these sensitivity estimates slightly optimistic. It is more difficult to interpret these results as mass limits, given DoAr 28's extreme youth and uncertainties about the luminosities of very young planets (Spiegel & Burrows, 2012; Allard et al., 2011; Marley et al., 2007; Fortney et al., 2008). Our SEEDS observations reach a limiting $H$-band absolute magnitude of ∼13.5 at a projected separation of 100 AU. At an age of 5 Myr, this corresponds to ∼4 $M_{\mathrm{Jup}}$ in the BT-Settl models, but anywhere from ∼4 $M_{\mathrm{Jup}}$ up to the deuterium-burning limit of ∼13 $M_{\mathrm{Jup}}$ in the Spiegel & Burrows (2012) models (SB12), depending on the initial entropy. We note that the high-mass end of this range requires a very cold start. Assuming an initial entropy midway between the minimum and maximum values of the SB12 models, the SB12 mass limits are only slightly higher than the BT-Settl limits.

There are theoretical reasons arguing against the formation of substellar companions below ∼5 $M_{\mathrm{Jup}}$ by direct gravitational collapse (Low & Lynden-Bell, 1976; Bate et al., 2003; Bate, 2009). Our SEEDS imagery rule out such a companion, which would necessarily form hot and beyond ∼80 AU. While a less massive core-accretion planet is unlikely to form at such a wide separation (DoAr 28's disk only extends to 70 AU), our data cannot rule out a Jovian planet scattered into a wide or unbound orbit.

### 2.3.3 Radiative Transfer Modeling

We modeled the DoAr28 system with the HOCHUNK3D Monte Carlo Radiative Transfer (MCRT) code as described in Whitney et al. (2013). HOCHUNK3D is similar to other codes (Min et al., 2009; Wolf & Hillenbrand, 2003; Dullemond & Dominik, 2004; Pinte et al., 2006; Robitaille, 2011; D'Alessio et al., 2006) and has a long history of being used to constrain the dust distribution in protoplanetary systems. The latest version of HOCHUNK3D decouples the small and large dust grain distributions, allowing settling of dust to be incorporated. This implementation can be thought of as utilizing overlapping disks with different dust grain size distributions. Dust density distributions in HOCHUNK3D are adopted from Shakura & Sunyaev (1973) and are characterized by a radial power law ($\alpha$), and a vertical gaussian distribution ($\beta$), as given by Equation **2.1**, where $r$ is the radial component in cylindrical coordinates and $z$ is the height of the disk from the mid-plane. $h$ is the scale height defined in Equation **2.2**, which is normalized at a defined radius of 100 AU. Deviations in the dust density distribution, such as gaps, spiral arms, and warped disks, can also be fully parameterized with HOCHUNK3D.

$$\rho \propto r^{-\alpha} \exp\left\{\left[\frac{z}{h}\right]^2\right\} \tag{2.1}$$

$$h \propto r^{-\beta} \tag{2.2}$$

Whitney et al. (2013) and references therein describe the full radiative transfer of the HOCHUNK3D code. To briefly summarize, the code uses a Henyey-Greenstein scattering phase function and includes parameters for forward-scattering and albedo calculated from the adopted dust grain model. The dust models we

used are described below. Temperature corrections utilized the Lucy method with a maximum number of six iterations (Lucy, 1999). We utilized $5*10^6$ photons for our broad exploration of MCRT parameter space, and $5*10^7$ photons for each of our runs where we compared both the observed SED and PI imagery against the models.

As is true with many MCRT codes, the large number of free parameters exceed the number of data points leading to model degeneracies. Since we lacked spatially resolved sub-millimeter observations that trace the radial distributions of large grains we assumed that the small and large grain disks had the same $\alpha$ and $\beta$ . We included a wall along the disk edge, as walls are thought to be common in transitional disks (Calvet et al., 2005; Espaillat et al., 2007a). We also assumed that there was a negligible envelope, no warping of the disk, and that the disk was azimuthally symmetric. We adopted dust parameters from Wood et al. (2002) dust model 1 for our large dust grains, which are composed of amorphous carbon and silicon ranging in sizes up to 1 millimeter. The small dust grain model we adopted was the average galactic ISM model from Kim et al. (1994). We generated a grid of 270 models and identified a broad range of parameters consistent with the observed SED in Table 4.2.

Our model SED is consistent with the observed photometry of DoAr 28, as shown in Figure 2.8, with the new SMA data point helping to constrain the large dust grain disk. We explored a range of gap sizes and how these influenced the resultant SED and images, and demonstrate below that a gap size of $\sim$8 AU best represents our data. We also found that the accretion rate and the gap density parameter had similar effects on the SED 4.2. We adopted the accretion rate quoted by Keane et al. (2014), $4.0 * 10^{-9}$ $\frac{M_\odot}{year}$, which led us to assume a gap density parameter of $5*10^{-5}$ (Table 4.2). Note however that our analysis of our new spectroscopic observations of DoAr 28 revealed a H-alpha equivalent width

($30 \pm 0.1\mathring{A}$) that was different than the 36 Å reported in Keane et al. (2014). This suggests that the system likely exhibits a variable accretion rate. Thus, the upper and lower bound values of the gap density shown in Table 4.2 are more representative of the system.

After using the observational SED of DoAr 28 to constrain our MCRT model parameters, we next used the observed surface brightness of our PI imagery to further constrain these parameters. Specifically, we measured the surface brightness of our PI imagery using a 4-pixel wide aperture along the major axis of the disk, and compared this to the H-band PI surface brightness predicted by our models (Figure 2.4). This iterative process enabled us to arrive at our final adopted model parameters listed in Table 4.2, including the adoption of the gap size at ∼8 AU. We used the model image subtracted from the PI images to find the inclination of 50°. To search for potential deviations from axi-symmetry in our data, we subtracted our (axi-symmetric) model, scaled to the peak intensity of the observed PI disk, from our observations. This process revealed evidence that the northern side of the disk exhibits a deficit of polarized flux near the inner working angle of our data as compared to the southern side of the disk (Figure 2.5). We discuss the potential origin of this asymmetry in the discussion section.

## 2.4 Discussion

Our HiCIAO H-band multi-epoch observations of the DoAr 28 transitional disk clearly reveals evidence of a scattered light disk observed in polarized intensity, extending from our effective inner working angle of 13 AU (0.″10; 2014 epoch) to 65 AU (0.″50). We observe no gap in the disk in our PI imagery at the location suggested by previous SED modeling of the system (15 AU; Kim et al. 2013). This suggests that either the small grain population is decoupled from the large

grain population, and/or that the disk gap resides inside of our effective inner working angle. Our MCRT modeling of the disk, using constraints both from DoAr 28's SED and our H-band imagery, suggests the disk has a gap extending from the dust sublimation radius out to ∼8 AU, that is only partially cleared of material. This gap size is smaller than that estimated from previous SED-only modeling efforts (15 AU; Kim et al. 2013). Other transitional disks observed in the H-band with HiCIAO as part of the SEEDS project, such as SAO 206462, MWC 758, and SR 21 (Muto et al., 2012; Grady et al., 2013; Follette et al., 2013), also exhibit evidence of small dust grains in their gaps, similar to that inferred for DoAr 28. Future multi-wavelength observations of the system that achieve a factor of ∼2 improvement in the effective inner working angle are needed to both test if the disk gap is truly as small as ∼8 AU, and to determine whether the radial distribution of small and large dust grains are decoupled, as is the case for systems like SR 21 (Follette et al., 2013).

The seemingly small gap size of DoAr 28 contrasts the disk gaps at larger orbital separations observed in other transitional disks, such as PDS 70 (70 AU; Hashimoto et al. 2011), SR 21 (36 AU; Follette et al. 2013), SAO 206462 (46 AU Muto et al. 2012), LkCa 15 (56 AU; Thalmann et al. 2014b), and Oph IRS 48 (60 AU Follette et al. 2015). If this gap is caused by dynamical interactions between planetary bodies in the system and the disk, this could suggest that DoAr 28 has few such fully formed companions, perhaps owing to the system being in a more youthful state than other imaged systems.

DoAr 28 exhibits several indications of morphological features that deviate from simple axisymmetry at modest signal-to-noise levels (Figure 2.5). For example, our 2014 epoch imagery exhibits tentative evidence of asymmetry in the northern-side of the disk (Figure 2.5). This type of asymmetry is commonly ob-

served, and could be caused by a range of phenomena ranging from companion interactions, a clumpy inner disk, and magneto-rotational instability. A companion such as a planet could induce warping of the disk which would shadow the outer portions of the disk. If the observed asymmetric feature is caused by a companion, the feature should move in the disk at the same rotational speed of the companion, and not at the Keplarian speed (Hashimoto et al., 2011). The asymmetry could also indicate the presence of a small azimuthal asymmetry in the inner disk. Numerical simulations of magneto-rotations instabilities (MRI) also suggest that MRI-driven disk winds can perturb the disk (Suzuki et al., 2010), which could also produce departures from axisymmetry. Additional epochs of spatially resolved imagery could help constrain whether the observed non-axisymmetric structure evolves with time, hence constrain the potential origin of this feature.

An additional, albeit more speculative indication of a non-axisymmetric feature is present along the southwest edge of the disk in our 2014 epoch data, namely the suggestive presence of a small hook-like feature (Figure 2.1). While the feature looks similar to spiral arms seen on in disks such as SAO 206462 and MWC 758 (Muto et al., 2012; Grady et al., 2013), there are no known T-Tauri transitional disks that exhibit spiral structures. It has been suggested that the lower temperatures of T-Tauri disks (compared to their Herbig analogs) results in lower sound speeds, creating tighter spiral arms (Muto et al., 2012) that would not be resolved in our data. Some studies have found that the dynamical temperature of CO gas is greater in T Tauri stars than in Herbig AeBe stars (2013), but this CO gas may not be well coupled with the small dust grain population. We conclude that this hook, if it is real, is most likely to be a perturbation of the disk much like the asymmetric feature described above and not a spiral arm.

## 2.5 Conclusion

We have reported the first spatially resolved scattered light image of the DoAr 28 transitional disk in H-band. We detect the scattered light disk from 0.″10 (13 AU) out to 0.″50 (65 AU), which is slightly interior to the location of the system's gap inferred by another group's SED modeling (15 AU). Although we detected a point source companion 1.″1 northwest of the system, our second epoch of imagery of the system indicates this object is most likely a background star. Using the HOCHUNK3D Monte Carlo Radiative Transfer code, we have modeled both the observed SED and H-band PI imagery of the system. Our best fit models utilize a modestly inclined (50°), 0.01 M$\odot$ disk that has a partially depleted inner gap from the dust sublimation radius out to $\sim$8 AU. Subtracting this best fit, axi-symmetric model from our polarized intensity data reveals evidence for a small asymmetry in the northern-side of the disk, which could be attributable to variety of mechanisms. We encourage future high spatial resolution sub-millimeter imagery of the system to better ascertain the location of the disk gap in the system, and to search for azimuthal and radial differences in distribution of small versus large dust grains that could be caused by recent planet formation in the system.

## 2.6 Acknowledgements

This chapter is reproduced by permission of the American Astronomical Society from the following publication: Rich, E. A., Wisniewski, J. P., Mayama, S., et al. 2015, AJ, 150, 86, "Near-IR Polarized Scattered Light Imagery of the DoAr 28 Transitional Disk". Here is the original publications author list: Evan A. Rich, John P. Wisniewski, Satoshi Mayama, Timothy D. Brandt3,31, Jun Hashimoto, Tomoyuki Kudo, Nobuhiko Kusakabe, Catherine Espaillat, Lyu Abe,

Eiji Akiyama, Wolfgang Brandner, Joseph C. Carson,Thayne Currie, Sebastian Egner, Markus Feldt, Kate Follette, Miwa Goto, Carol A. Grady, Olivier Guyon, Yutaka Hayano, Masahiko Hayashi, Saeko S. Hayashi, Thomas Henning, Klaus W. Hodapp,Miki Ishii, Masanori Iye, Markus Janson, Ryo Kandori, Gillian R. Knapp, Masayuki Kuzuhara, Jungmi Kwon, Taro Matsuo, Michael W. McElwain, Shoken Miyama, Jun-Ichi Morino, Amaya Moro-Martin, Tetsuo Nishimura, Tae-Soo Pyo, Chunhua Qi, Eugene Serabyn, Takuya Suenaga, Hiroshi Suto, Ryuji Suzuki,Yasuhiro H. Takahashi, Michihiro Takami, Naruhisa Takato, Hiroshi Terada, Christian Thalmann,Daigo Tomono, Edwin L. Turner, Makoto Watanabe, Toru Yamada, Hideki Takami,Tomonori Usuda, and Motohide Tamura

We thank the referee for providing suggestions that improved the content and layout of this paper. We acknowledge support from NSF-AST 1009203 (J.C.), 1008440 (C.G.), and 1009314 (E.R, J.W, J.H) and the NASA Origins of Solar System program under NNX13AK17G (J.W.), RTOP 12-OSS12-0045 (M.M.), and NNG13PB64P (C.G.). This work is partly supported by a Grant-in-Aid for Science Research in a Priority Area from MEXT Japan and by the Mitsubishi Foundation. This work was performed [in part] under contract with the Jet Propulsion Laboratory (JPL) funded by NASA through the Sagan Fellowship Program executed by the NASA Exoplanet Science Institute. The authors recognize and acknowledge the significant cultural role and reverence that the summit of Mauna Kea has always had within the indigenous Hawaiian community. We are most fortunate to have the opportunity to conduct observations from this mountain.

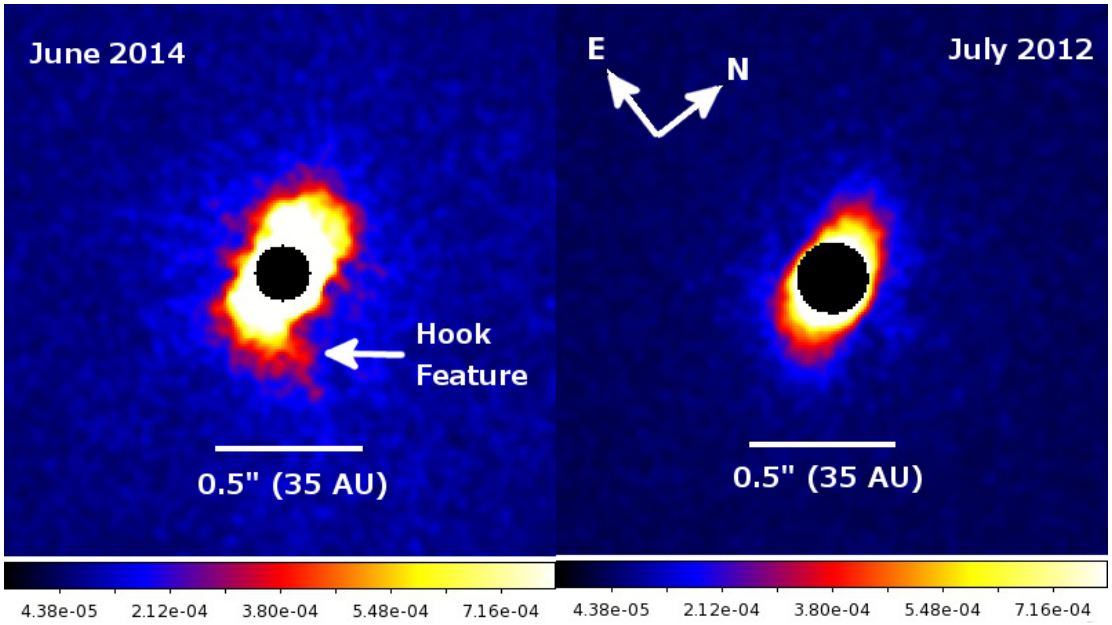


Fig. 2.1.— The H-band polarized intensity (PI) image of DoAr 28 in 2014 June (left) and 2012 July (right) is shown over a field of view of 1.″95 x 1.″95 with the excess halo subtracted as described in section 2.2.1. We have applied a software mask over the location of the central star, with a size of 0.″17 (24 AU) for the 2012 epoch data and 0.″10 (13 AU) for the 2014 epoch data, for asthetic purposes. The imagery is plotted linearly in units of mJy, and was further smoothened with a 3-pixel Gaussian kernel.

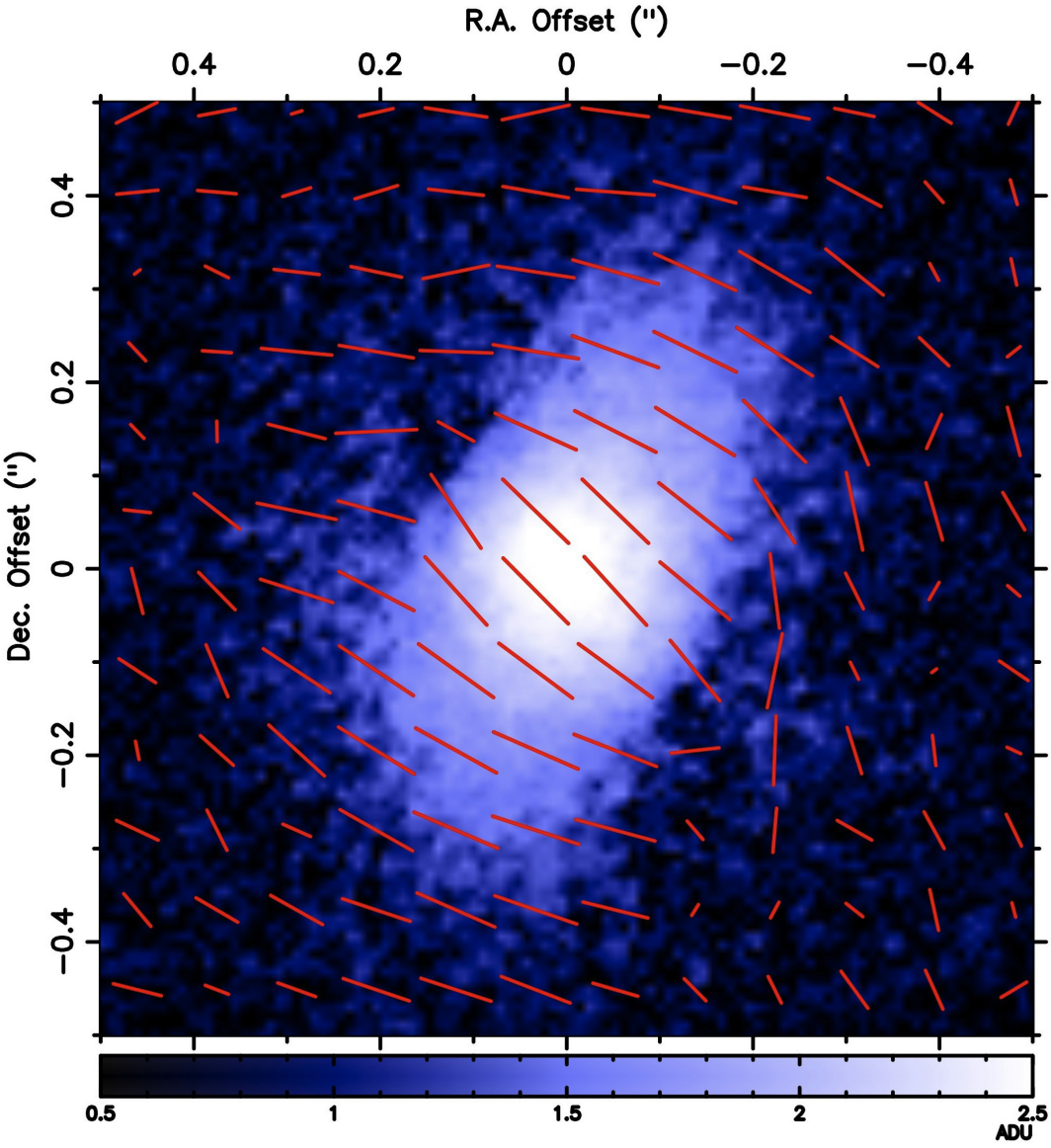


Fig. 2.2.— A polarization vector map is overlaid on the PI image of DoAr 28 of epoch 2014 including halo subtraction. While the direction of the vectors represent the orientation of the observed polarization, the length of the vectors is a relative quantity and does not indicate the percent polarization present. The clear centrosymmetric behavior of the vectors confirms that we are detecting scattered light originating from the system's disk.

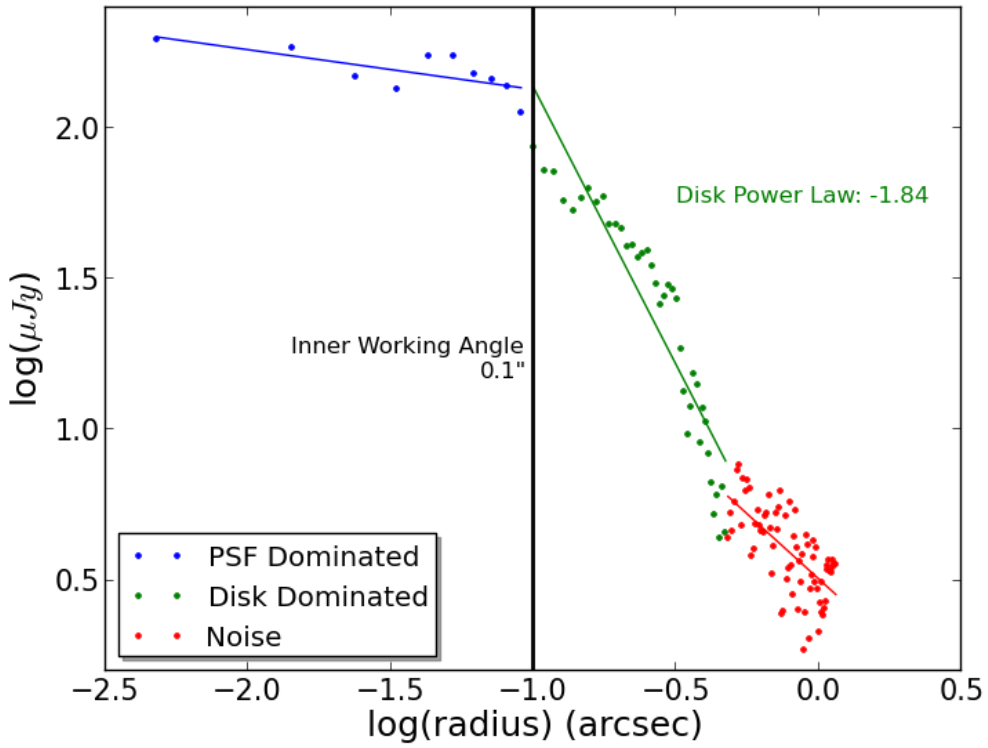


Fig. 2.3.— The radial profile of 2014 epoch data along the north-side of the major axis illustrates clear evidence of two departures from a singular power law behavior. One clear break in the power law happens at $\sim$0.″1 (the FHWM of the 2014 data), where the system transitions from being dominated by unsubtracted PSF residuals (blue) to disk dominated scattered light (green). The second break occurs when the disk dominated scattered light (green) is overwhelmed by background noise (red). The solid colored lines are best fit lines from linear regression fits to the disk power law shown on the figure. The black vertical line represents where the inner working angle is defined.

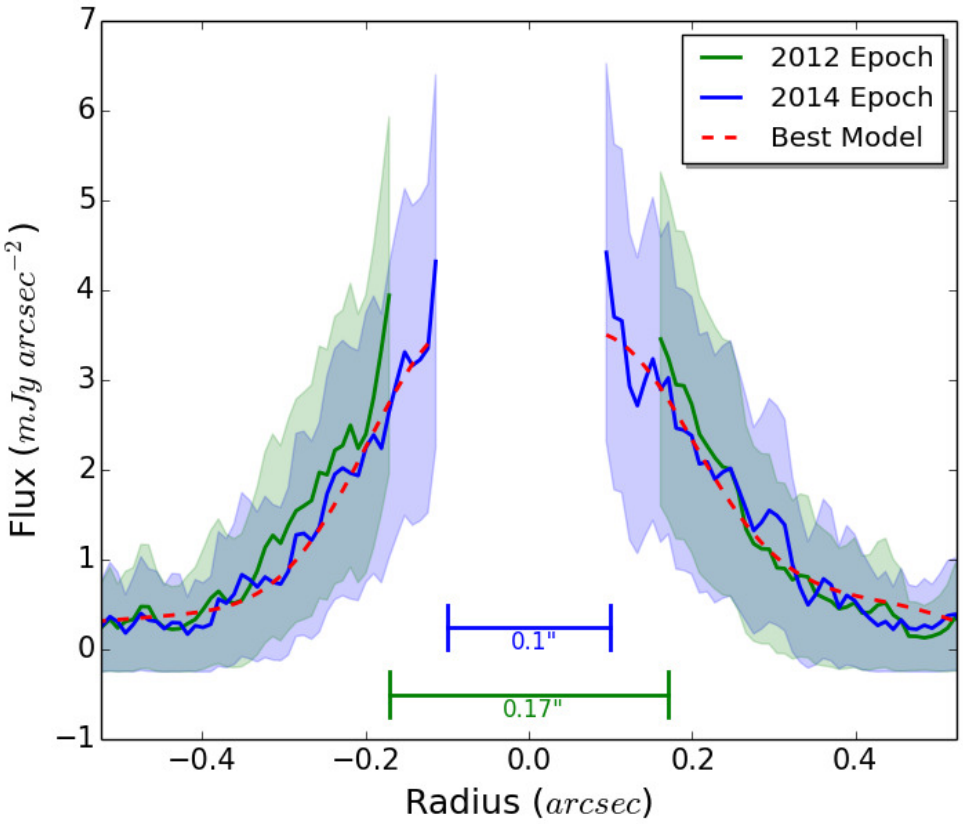


Fig. 2.4.— The observed surface brightness along the major axis of the disk in our PI imagery at our 2012 (green) and 2014 epochs (blue), computed with a 4 pixel-wide average, is shown along with analogous surface brightness measurements from our MCRT model (red). The shaded colors represent a 1-sigma error bar with light green for 2012 epoch and light blue for 2014 epoch. The left side corresponds to the South end of the disk and the right side corresponds to the North side of the disk shown in Figure 2.1. The central portions of these profiles have been removed, signifying the effective inner working angle of our data.

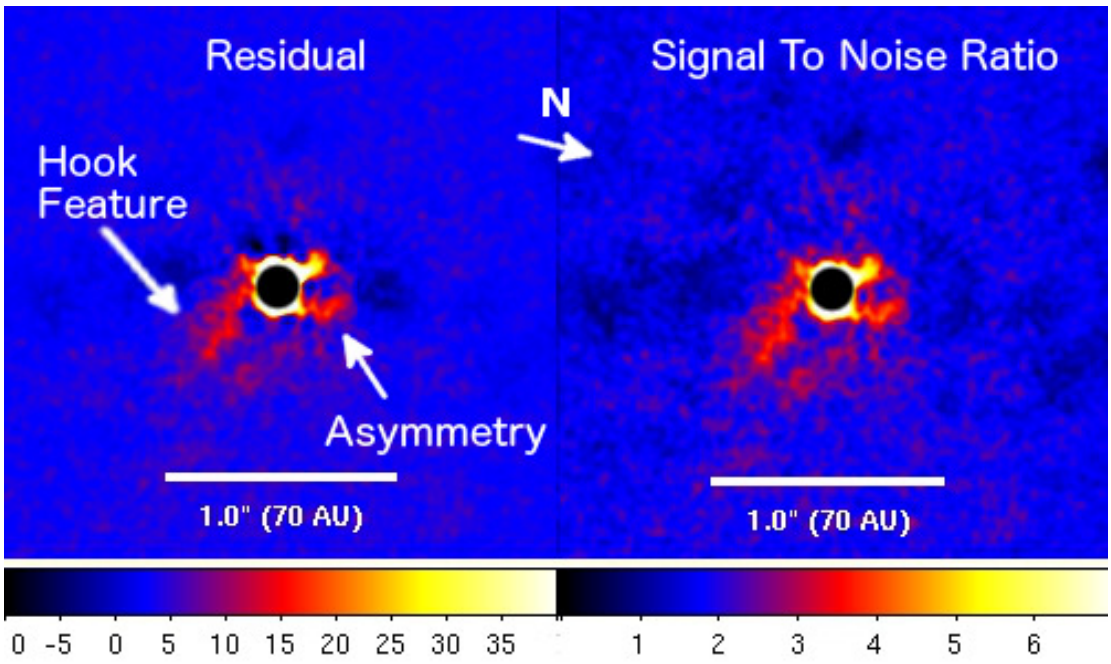


Fig. 2.5.— We subtracted our best fit model from our 2014 epoch PI imagery, yielding the residual imagery shown on the left. The right panel represents the signal to noise of the residual imagery. The image has been rotated such that the major axis is horizontal in the figure, with the northeast region of the disk on the right-hand side of the image. Two potential asymmetries are observed, including a "hook" feature noted in Figure 2.1 and a further asymmetry discussed in Section 3.6. The imagery is plotted linearly in units of ADU, and was further smoothened with a 3-pixel Gaussian kernel.

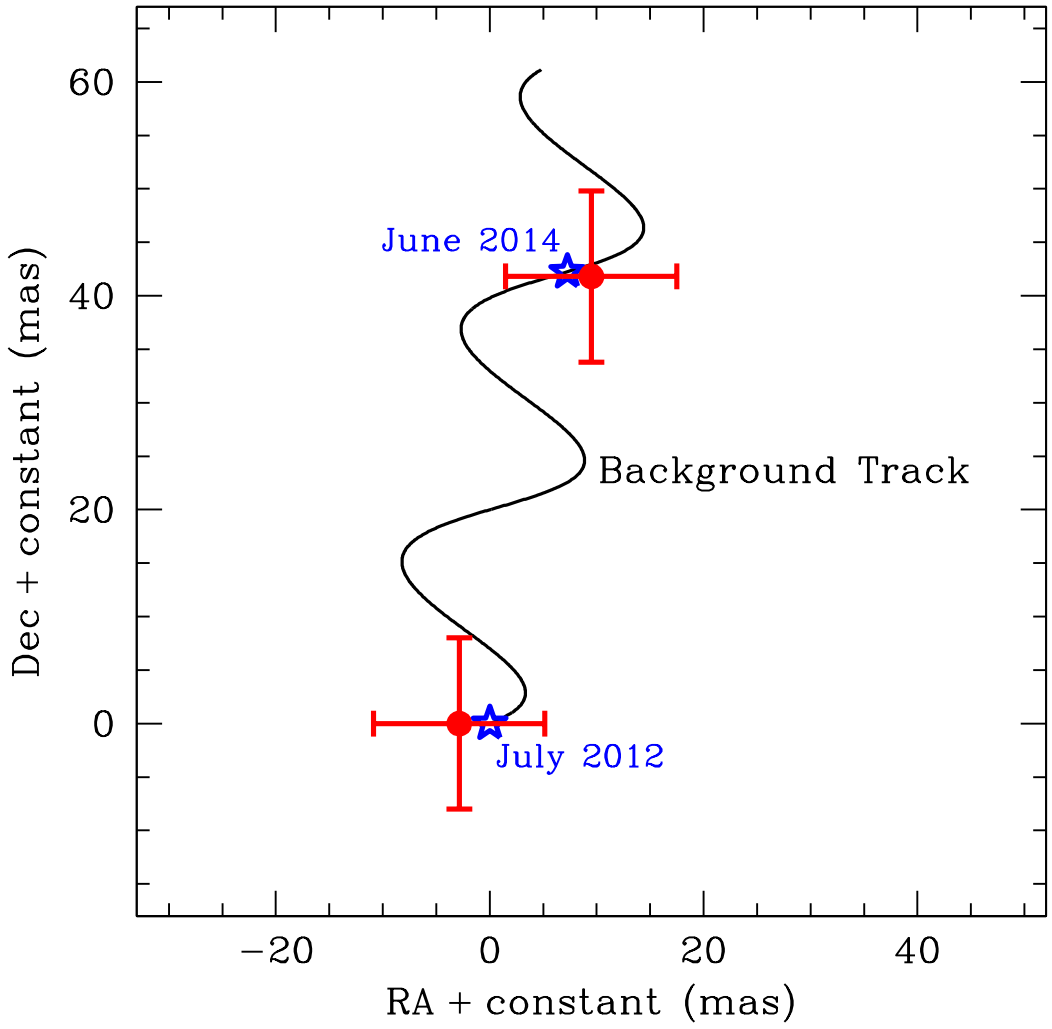


Fig. 2.6.— The proper motion of DoAr 28 (blue star) and its candidate companion (red circle) in our two epochs of observations. DoAr 28 shares proper motion with $\rho$ Oph shown as the black sinusoidal line. The observed proper motion suggests that the companion is not co-located with DoAr 28, as discussed in Section 2.3.2.

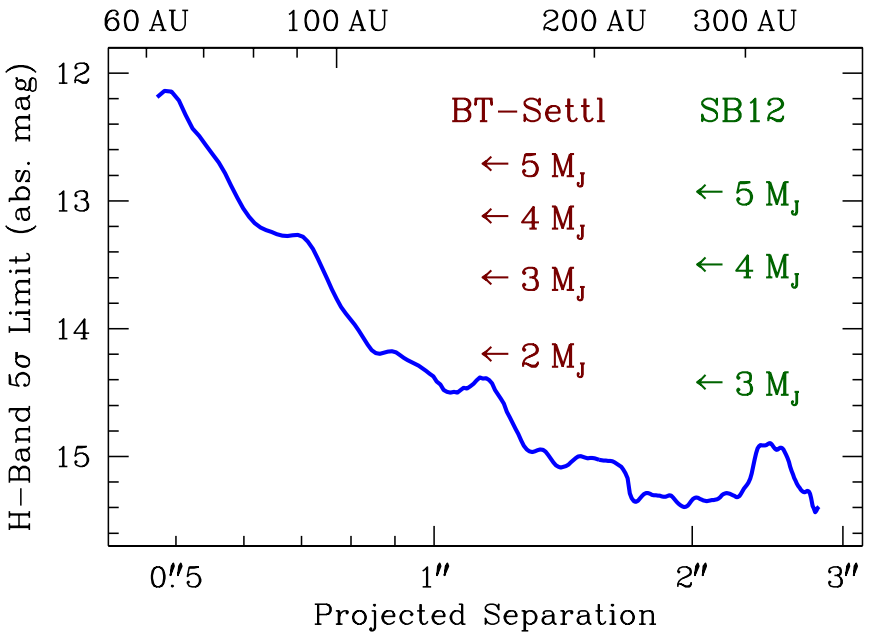


Fig. 2.7.— The computed sensitivity limits of point source detections in our DoAr 28 imagery with a signal to noise of 5 sigma are given, along with associated planetary mass limits assuming both BT-Settl (burgundy) and SB12 (green) planet formation models. We assume an age of 5 Myr and SB12 "warm start" models midway between the minimum and maximum available initial entropies. We do not detect evidence of any co-moving companions above these limits.

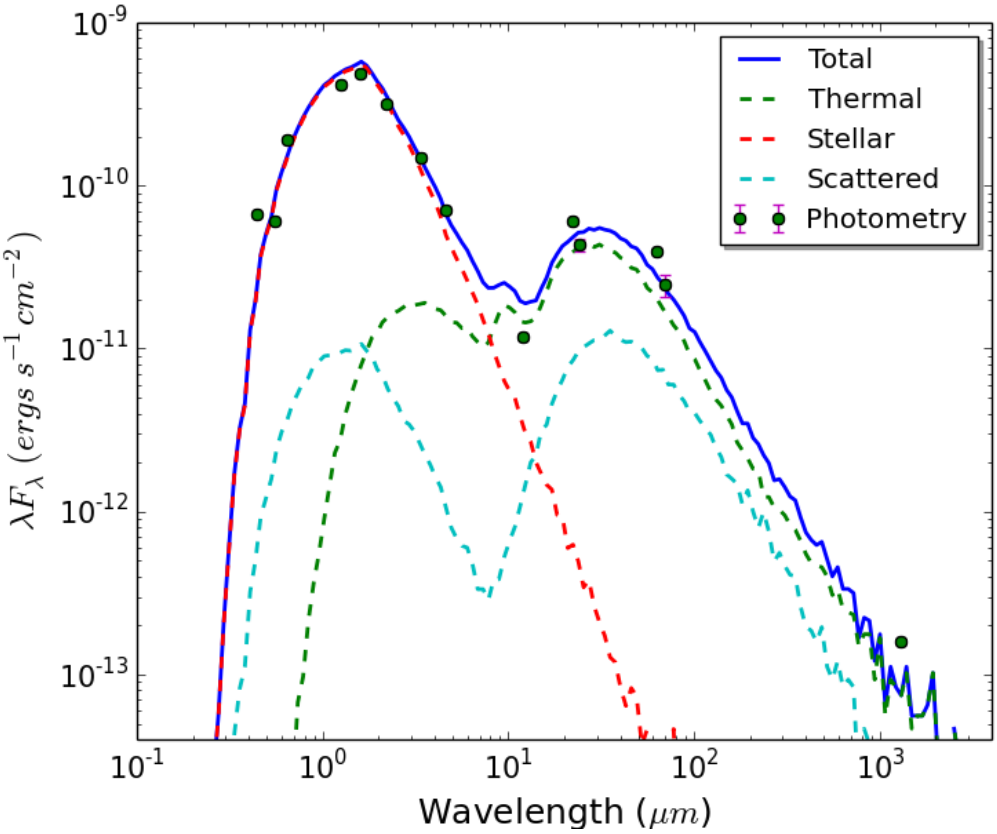


Fig. 2.8.— The observed SED of DoAr 28, as compiled in Table 2.2, is shown along with our best fit model, using the parameters compiled in Table 4.2. The solid line represents the total SED, whereas the dashed lines represent the different contributions to the SED, including thermal emission from the dust disk (thermal), the stellar photosphere (stellar), and scattered light from the disk (scattered).

| Variable | Model | Low Bound | Upper Bound |
|---|---|---|---|
| $T_{eff}$ (K) | 4375 | ··· | ··· |
| $R_{\odot}$ | 1.6 | 1.5 | 1.6 |
| Disk Mass ($M_{\odot}$) | 0.01 | 0.005 | 0.05 |
| Max Disk Radius (AU) | 250 | 200 | 500 |
| Fraction of Mass | 0.8 | 0.7 | 0.99 |
| Inner Gap Radius (AU) | 0 | ··· | ··· |
| Outer Gap Radius (AU) | 8 | 7 | 9 |
| Wall height (AU) | 0.5 | 0.5 | 0.5 |
| Wall length (AU) | 0.5 | 0.5 | 1.1 |
| Zscale Disk 1 | 1.7 | ··· | ··· |
| Zscale Disk 2 | 1.7 | 1.7 | 1.9 |
| $\alpha$ | 2.0 | 1.9 | 2.1 |
| $\beta$ | 1.0 | 0.99 | 1.01 |
| Accretion ($\dot{M}_{\odot}$) | 4.0E-9 | ··· | ··· |
| Gap Density | 5E-6 | 5E-5 | 5E-7 |
| Inclination (i) | 50° | 40° | 65° |

Table 2.1:: A summary of the lower and upper acceptable bounds of key HOCHUNK3D parameters that yield a fit consistent with our observations, along with the "best" values that were adopted for our final model. The "fraction of mass" parameter represents the fraction of the mass located in the large dust grain disk; the rest of the disk mass is located in the small dust grain disk. The parameter "zscale" represents the scale height parameter. The "gap density" is the ratio of the dust density inside the gap relative to the density of dust at the inner edge of the disk. The "Zscale Disk" is the scale hight of disks 1 and 2 where disk 1 is large grain dust and disk 2 is small grain dust. Parameters $\alpha$ and $\beta$ describe the density profile of the disk defined in equation **2.1**.

| Wavelength ($\mu$m) | Flux (Jy) | Error (Jy) | Facility | Reference |
|---|---|---|---|---|
| 0.44 | 0.0098 | ··· | Mt. Maidanak Obs. | (Grankin et al., 2007) |
| 0.55 | 0.0112 | ··· | Mt. Maidanak Obs. | (Grankin et al., 2007) |
| 0.64 | 0.0411 | ··· | USNO | (Monet et al., 1998) |
| 1.26 | 0.1759 | 0.0039 | 2MASS | (Cutri et al., 2003) |
| 1.6 | 0.2606 | 0.0055 | 2MASS | (Cutri et al., 2003) |
| 2.22 | 0.2379 | 0.0042 | 2MASS | (Cutri et al., 2003) |
| 3.4 | 0.1670 | 0.0015 | WISE | (Cutri & et al., 2012) |
| 4.6 | 0.1092 | 0.00087 | WISE | (Cutri & et al., 2012) |
| 12.0 | 0.0471 | 0.00045 | WISE | (Cutri & et al., 2012) |
| 22.0 | 0.4450 | 0.0037 | WISE | (Cutri & et al., 2012) |
| 24.0 | 0.348 | 0.0322 | Spitzer/MIPS | (Evans et al., 2003) |
| 62 | 0.829 | 0.013 | Herschel | (Keane et al., 2014) |
| 70.0 | 0.579 | 0.0891 | Spitzer/MIPS | (Evans et al., 2003) |
| 1300 | 0.072 | 0.0019 | SMA | SMA Observation |

Table 2.2:: The tabulated version of DoAr 28's photometry that was used to construct the SED shown in Figure 2.8.

# Chapter 3

# Thermal Infrared Imaging and Atmospheric Modeling of VHS J125601.92-125723.9 b: Evidence for Moderately Thick Clouds and Equilibrium Carbon Chemistry in a Hierarchical Triple System

## 3.1 Introduction

Exoplanet surveys have recently measured the frequency of exoplanets as a function of a host of parameters like stellar mass, metallicity, orbital separation, and planetary mass (Winn & Fabrycky, 2015). These parameters help to inform our understanding of how and where exoplanets form. The observed frequency of gas giants at small (<2 au) separations rises from ∼3% for dM stars to ∼14% for solar metallicity A-type stars; this dearth of massive planets around dM stars is consistent with theoretical predictions (Laughlin, Bodenheimer, & Adams, 2004) of the core accretion model (Pollack et al., 1996). At larger orbital separations (10s-100s of au), the frequency of gas giants around dM stars is <6% (Bowler et al., 2015). Recent results from Kepler have shown both that the frequency of small mass planets at short orbital periods increases around low mass stars (Borucki et al., 2011; Howard et al., 2012) and there is a lack of planets larger than 2.5 $R_{Earth}$ surrounding dM stars at short orbital periods.

High contrast imaging investigations have similarly begun to discover gas giant exoplanets located at large orbital separations from their stars (Fomalhaut b,

Kalas et al. 2008, $\beta$ Pictoris b, Lagrange et al. 2009, 2010; HR 8799 bcde, Marois et al. 2010; $\kappa$ And. b, Carson et al. 2013; 51 Eri b ,Macintosh et al. 2015; HD 100546 bc ,Quanz et al. 2013, Currie et al. 2015a). While most of these directly imaged gas giants surround early-type stars, detections have been reported around Solar-analogs (GJ 504b, Kuzuhara et al. 2013) and dM stars (e.g. ROXs42B, Currie et al. 2014a; GU Psc, Naud et al. 2014). Yet the formation mechanisms responsible for these systems is still under debate. A growing number of objects with wide orbits and modest mass ratios (eg. HD 106906b, Bailey et al. 2014; ROXs42Bb, Currie et al. 2014a; 1RXSJ1609, Lafrenière et al. 2008; 2M J044144, Todorov et al. 2010) have led to suggestions that the planetary companion formed via a binary star-like process rather than the core accretion process (Low & Lynden-Bell 1976, Bate 2009, Brandt et al. 2014).

Although binary stars are common (e.g. Raghavan et al. 2010), our understanding of the frequency of exoplanets around binaries and higher order systems remains limited. Since the discovery of the first exoplanet surrounding a binary host (Kepler-16b, Doyle et al. 2011), less than a dozen similar systems have been discovered by Kepler (Winn & Fabrycky 2015 and references therein). The analysis of publicly available Kepler data led Armstrong et al. (2014) to conclude that the frequency of planets with R $>$ 6 $R_{Earth}$ on periods of less than 300 days was similar to that of single star rates; however, this conclusion is critically dependent on the assumed planetary inclination distribution. While at least one bona fide planetary mass companion orbiting a binary has been imaged (ROXs 42Bb Simon et al., 1995; Ratzka, Kohler, & Leinert , 2005; Currie et al., 2014a) most dedicated direct imaging surveys for gas giant planets around binaries have not yielded any firm detections to-date (Thalmann et al., 2014a).

Recently, Gauza et al. (2015) reported the detection of a planetary mass (11.2 $^{+9.7}_{-1.8}$ $M_J$) companion at a projected separation of 102 $\pm$9 au from its host star

VHS J125601.92-125723.9 (hereafter VHS 1256), described as a M7.5 object with an inferred mass from its bolometric luminosity of $73^{+20}_{-15}$ $M_J$, placing it near the hydrogen burning limit. The primary was estimated to have an age of 150-300 Myr from both kinematic membership in the Local Association and lithium abundance. At a distance of $12.7 \pm 1.0$ *pc* measured from trigonometric parallax (Gauza et al., 2015), this made VHS 1256 the closest directly imaged planetary mass system to the Earth. Stone et al. (2016) reported a greater distance to VHS 1256 of $17.1 \pm 2.5$ *pc* based on spectrophotometry of the system.

From the standpoint of substellar atmospheres and atmospheric evolution, VHS 1256 b is a particularly unique object. Its near-infrared properties resemble those of the HR 8799 planets and a select few other young (t $\lesssim$ 30 Myr) and very low mass (M $\lesssim$ 15 $M_{\rm J}$) substellar objects, occupying roughly the same near-infrared color-magnitude space (Gauza et al., 2015; Faherty et al., 2016): a continuation of the L dwarf sequence to fainter magnitudes and cooler temperatures. Indeed, as shown by atmosphere modeling, the near-infrared properties of objects like HR 8799 bcde and 2M 1207 B reveal evidence for thicker clouds than field brown dwarfs of the same effective temperatures (Currie et al., 2011). VHS 1256 b then offers a probe of clouds at ages intermediate between these benchmark objects and Gyr-old field objects and thus some insights into the atmospheric evolution of low-mass substellar objects.

Furthermore, non-equilbrium carbon chemistry can be probed by new thermal infrared photometry, in particular at $M'$ (e.g. Galicher et al., 2011)[a]. New thermal infrared data for VHS 1256 b allows us to assess the evidence for non-equilibrium chemistry for the objects at/near the deuterium burning limit and at ages older

[a]The existing W2 photometry reported in Gauza et al. (2015) covers a far wider bandpass (4–5 $\mu m$). Much of this wavelength range is far less sensitive to carbon monoxide opacity at relevant temperatures that is a tracer of non-equilbrium carbon chemistry, while $M'$ is far more (uniquely) sensitive (e.g. see Figure 7 in Currie et al. 2014b).

than HR 8799 bcde.

In this work, we present new adaptive optics imagery of VHS 1256, providing the first detections of its wide-separation companion in major thermal IR broadband filters, $L'$ and $M'$. We use these mid-infrared photometric points and optical and near-infrared photometry from Gauza et al. (2015) to perform the first atmospheric (forward) modeling of VHS 1256 b and the first assessment of how its thermal IR properties (e.g. carbon chemistry) compare to younger planet-mass objects with similar near-IR colors. Additionally, we report our independent determination of the primary's binarity, also reported in Stone et al. (2016), following our original work (Anthes Rich et al., 2015) with additional analyses. We will adopt the same nomenclature as Stone et al. 2016, referring to the close partially resolved binary as VHS 1256 A and B, and the wide companion as VHS 1256 b.

After discussing our observations in Section 4.2, we search for new companions around VHS 1256 and investigate the binarity of VHS 1256 in Section 3.3. Next, we discuss improved photometry of VHS 1256 A, B, and b at $L'$and $M'$ in Section 3.4. Using the new L$'$ and M$'$ photometry, we assess the atmospheric properties of VHS 1256 b in Section 3.5. Finally, we discuss the implications of our study in Section 3.6.

## 3.2 Observations and Reductions

We observed VHS 1256 in $L'(\lambda_{center} = 3.77\ \mu\text{m})$ and $M'$ ($\lambda_{center} = 4.68\ \mu\text{m}$) bands on 2015 June 6 using the Infrared Camera and Spectrograph (IRCS; Kobayashi et al. (2000)) on the 8.2m Subaru Telescope, along with the Subaru AO-188 adaptive optics (AO) system (Hayano et al., 2008, 2010) in laser guide star (LGS) mode. All observations were made with IRCS having a plate scale of 20.57 mas pix$^{-1}$.

For the L' band, we utilized a 0.1 second exposure time along with 100 co-adds to achieve 10 second exposures per dither frame. We obtained a total of 13 dither sets, using a 5 point dither per set, yielding a total on-source integration time of 650 seconds. For our $M'$-band imaging, we utilized a 0.06 second exposure time along with 100 co-adds to achieve 6 second exposures per dither frame. We observed VHS 1256 for a total of 3 dither sets, using a 5 point dither per set, yielding a total on-source integration time of 90 seconds. All data were obtained in angular differential imaging (ADI) mode; a total field rotation of $17^{\circ}.4$ and $2^{\circ}.8$ was achieved in $L'$and $M'$ respectively.

We utilized two approaches to detect VHS 1256 b. First, we simply derotated each image to true north after sky subtraction. We inspected the quality of each image set, and determined that the AO performance was subpar during 7 $L'$frames (70 seconds of integration); hence, we removed these data before median combining frames. Using an identical process, we reduced the $M'$ data and removed 6 of the 15 frames (54 seconds of integration) due to subpar AO performance.

Second, we utilized advanced PSF subtraction methods and a different approach with image combination to compensate for the shorter integration time and brighter sky background in $M'$ and obtained slightly deeper limits in $L'$. We use A-LOCI as in Currie et al. (2012, 2015b) with a large optimization area (500 PSF footprints) and rotation gap (1.5 times the diffraction limit at L$'$ and M$'$) combined with a moving pixel mask to flatten the background without removing signal from VHS 1256 b[a]. We then applied a 4 $\lambda$/D spatial filter and combined the derotated data to obtain a mean image using a 3-$\sigma$ outlier rejection. This allowed us to obtain a higher signal-to-noise detection of VHS 1256 b, which was

[a]as shown by Galicher et al. (2011), advanced methods usually used for point-spread function (PSF) subtraction can in some cases better flatten the sky background, especially in M$'$. As VHS 1256 b is located about $8''$ from the primary, even a small $2^{\circ}.8$ parallactic motion is sufficient to apply PSF subtraction methods like LOCI (Lafrenière et al., 2007)

barely detectable in $M'$ at the 3-$\sigma$ level using the first image processing method, obtaining about a 40% deeper background limit at $L'$.

We utilized observations of the $L'$ standard FS 138 (van der Bliek, Manfroid, & Bouchet, 1996) obtained on 2015 June 7 using NGS and observations of the $M'$ standard HR 5384 (van der Bliek, Manfroid, & Bouchet, 1996) obtained on 2015 June 8 without AO to transform our photometry to a standard system. We did not obtain successful images of a dense stellar cluster that would be needed to construct a robust distortion correction for our $L'$and $M'$ imagery; hence, we have included no such correction to our data. Our lack of a distortion correction introduces some uncertainty into VHS 1256 b's separation, but does not affect our other results.

## 3.3 Search for Additional Companions

### 3.3.1 Point Source Detections and Detection Limits in the $L'$and $M'$ Field of View

Our fully reduced $L'$- and $M'$-band imagery (Figure 3.1) clearly reveals the presence of both the composite source of VHS 1256 A and B (A+B) and VHS 1256 b reported by Gauza et al. (2015). We detect the companion at SNR $\sim$ 130 (100) in the $L'$ data and at 4.5 (3) in the $M'$ data using the A-LOCI (classical) reduction, where the latter detection is roughly comparable to the detection significance of HR 8799 bcd in Galicher et al. (2011). We do not identify any additional point sources.

We determined the centroid positions of both objects, and found that VHS 1256 b is located $8\farcs13 \pm 0\farcs04$ from VHS 1256 A+B at a position angle of $217.8° \pm 0.3°$ in $L'$and $8\farcs17 \pm 0\farcs04$ at a position angle of $217.8° \pm 0.3°$ in $M'$ (Table 3.1).

This separation is consistent with the angular separation observed by Gauza et al. (2015) of $8\farcs06 \pm 0\farcs03$ at a position angle of $218.1° \pm 0.2°$. Note that we did not utilize a distortion correction.

To compute the 5-$\sigma$ point source detection limit in $L'$, we followed standard methods used in high-contrast imaging data (e.g. Currie et al., 2015b). We convolved the image with a gaussian profile having a FWHM set by the observed FWHM of VHS 1256 b and determinated the robust standard deviation of convolved pixels at each angular separation. The limiting 5-$\sigma$ point source detection limits of our $L'$ imagery based on this method is roughly 16.4 mag exterior to $2\farcs5$ ($r_{proj} \sim 32$ au for $d = 12.7$ $pc$), degrading to VHS 1256 b's brightness at $0\farcs5$. Due to the thermal background, limited integration time, and the partial FOV coverage, the $M'$ imagery do not provide stringent constraints on the presence of additional point sources compared to the $L'$imagery.

### 3.3.2 Analysis of the Primary: Evidence of Multiplicity

It is apparent from visual inspection of Figure 3.1 that the VHS 1256 A+B is much more elongated in both $L'$and $M'$ -bands than VHS 1256 b. In fact, simple gaussian fits to the data reveal that the FWHM of the central star is significantly broader than the companion in both band-passes. Zooming in on the region around VHS 1256 A+B, Figure 3.2 demonstrates that the central star is comprised of two marginally resolved sources. Using a modified elliptical least squares minimization fitting routine written by Nicky van Foreest [a], we compute the average ellipticity ($e = ((a^2 - b^2)/a^2)^{0.5})$) of our sources. The average ellipticity of the central star, $0.85 \pm 0.02$ and $0.825 \pm 0.005$ in the $L'$and $M'$ bands respectively, is significantly greater than the average ellipticity observed for the

[a] http://nicky.vanforeest.com/misc/fitEllipse/fitEllipse.html

companion ($0.48 \pm 0.03$ in $L'$). These results all indicate that the central star is clearly comprised of the superposition of two separate sources.

To help ascertain the probability that the observed multiplicity of VHS 1256 A and B arises from chance alignment of VHS 1256 with a background source, we utilize archival WISE W1-band imagery, which has a similar band-pass as our $L'$-band imagery. The local density of W1 sources between 10.2 and 10.8 mag is $\sim$ 34 $deg^{-2}$. Hence, the chance alignment of two sources, within $0\farcs106$ is $5 \times 10^{-6}\%$.

## 3.4 Photometry

Aperture photometry was performed on all components of the VHS 1256 system. Both the L′ photometry of VHS 1256 A+B (9.757 ± 0.04 magnitude) and VHS 1256 b (12.93 ± 0.02 magnitude) and the M′ photometry of VHS 1256 A+B (9.65 ±0.04 magnitude) and VHS 1256 b (12.66 ±0.26 magnitude) are broadly consistent with the literature (Gauza et al., 2015) WISE W1 and W2 photometry (Table 3.2). We utilized a 30 pixels radius for aperture photometry. In addition to the standard uncertainty terms (poisson noise and standard deviation of background), we included read noise, shot noise, and the errors from the zero point terms. We do not include error terms due to variations in the atmospheric transmission during our observations, or due to variations that arise between the use of NGS versus LGS observing modes. Note that our $L'$and $M'$ VHS 1256 b photometry improves on the respective WISE W1 and W2 errors previously presented.

The relative astrometry and flux of VHS 1256 A and B were constrained by fitting a linear combination of two PSFs to our $L'$ images; we adopt VHS 1256 b as the PSF. We first align the dithered images of the central binary by maximizing their cross-correlation and then combine them by averaging. Averaging the frames is optimal in the case of Gaussian errors; in our case, it reduces the noise by nearly

a factor of 2 compared with a median combination.

We use bicubic spline interpolation to translate the PSF of VHS 1256 b. We then simultaneously adjust the positions and normalizations of two PSFs to minimize

$$\chi^2 = \sum \frac{(\mathrm{PSF}_1 + \mathrm{PSF}_2 - \mathrm{data})^2}{\sigma_{\mathrm{ph}}^2 + \sigma_{\mathrm{bg}}^2} \tag{3.1}$$

where $\sigma_{\mathrm{ph}}^2$ is the variance from photon noise and $\sigma_{\mathrm{bg}}^2$ is the variance from read noise and the thermal background. We estimate $\sigma_{\mathrm{ph}}^2$ from the instrument gain and measure $\sigma_{\mathrm{bg}}^2$ from empty regions of the image. The variance is the sum of variance in the image and scaled variance from the noisy companion PSF. In practice, most of the noise arises from scaling the companion PSF, as the noise increases linearly with the scaling factors.

A good fit should have $\chi^2 \approx N_{\mathrm{pix}}$, where $N_{\mathrm{pix}}$ is the number of pixels in the region being fit. With a simple estimate of the background and photon noise, we find that our best-fit $\chi^2$ is about four times the number of pixels; we therefore increase our estimated uncertainties to achieve a reduced $\chi^2$ of unity. After rescaling our noise to achieve a minimum $\chi^2 = N_{\mathrm{pix}}$, we compute our confidence regions by integrating the likelihood

$$\mathcal{L} = \exp\left[-\chi^2/2\right] \tag{3.2}$$

and computing the regions containing 68% of the likelihood (for our $1\sigma$ confidence intervals).

Figure 3.3 shows the results of this fit: the observed $L'$ intensity of VHS 1256 A and B (left panel), the best-fit translated and scaled linear combination of companion PSFs (middle panel), and the residuals (right panel), expressed in units of the peak intensity of the original data. The fit is good to a few percent near the PSF cores, comparable to the expected uncertainties from the noise and

from interpolations. Spatial correlations in the noise are visible in the residual image even far from the PSF core; it is these correlations that force us to scale our errors. A full treatment of the problem would modify $\chi^2$ (Equation **3.1**) to account for the data's non-diagonal covariance matrix. Table 3.1 lists our fitted parameters: a separation of $0\farcs106 \pm 0\farcs001$ ($5.18 \pm 0.05$ pixels), a position angle of $-7\fdg6 \pm 0\fdg5$, and a flux ratio of $1.03 \pm 0.01$. We thus obtain 1% measurements of the relative photometry and separation.

## 3.5 Atmospheric Properties of VHS 1256 b

The discovery work by Gauza et al. (2015) suggested that VHS 1256 b, based on its spectral shape and color-magnitude diagram position, is a red L/T transition object similar to HR 8799 bcde (e.g. Currie et al., 2011; Bonnefoy et al., 2016). With SED information spanning the red optical to mid-infrared, we can more thoroughly compare VHS 1256 b's properties to those of other substellar objects and fit atmosphere models with a range of assumptions about clouds to reproduce VHS1256 b's spectrum. Many free floating L/T dwarfs with red optical to near-infrared photometry and spectra have been studied (e.g. Knapp et al., 2004). However, even considering young brown dwarfs as well as the field, VHS 1256 b occupies an extremely sparsely populated near-infrared color-magnitude diagram position shared by planet mass objects like HR 8799 bcde and 2M 1207 B (Faherty et al., 2016). Furthermore, these objects are young, typically less than $\sim 30$ $Myr$ old (Faherty et al., 2016), while VHS 1256 is at least older than 200 $Myr$ (Stone et al., 2016, sect 6.2 of this work).

While the similarity of VHS 1256 b's near-infrared colors to those of HR 8799 bcde suggest that their atmospheric properties likewise share some similarity (e.g. perhaps thick clouds), the addition of thermal infrared data in this work allows us

to further quantify this feature and assess whether or not VHS 1256 b shows clear evidence for non-equilibrium carbon chemistry. Compared to HR 8799 bcde, VHS 1256 b's available suite of photometry extends far bluer, into the optical. Thus, the companion provides a new test of atmospheric models used to reproduce at least some bona fide directly-imaged planets. Furthermore, as shown in Faherty et al. (2016), young L dwarfs tend to follow a reddened version of the field sequence. Comparing VHS 1256 A+B's colors to those of the field sequence and young associations like AB Dor can then provide a very coarse assessment of the system's youth.

### 3.5.1 Mid-Infrared Colors of VHS 1256 A, B, and b

Figure 3.4 compares VHS 1256 A, B, and b's near-infrared and mid-infrared color magnitude diagrams (CMDs) to the field sequence, planetary companions like HR 8799 bcde, and substellar objects in AB Dor ($t \sim 125\ Myr$). The primary components to VHS 1256 appear indistinguishable from the field sequence and bluer than AB Dor members. Even if VHS 1256 b is at 17.1 $pc$ and thus intrinsically brighter, it still appears somewhat "under luminous", along an extension of the L dwarf sequence to fainter magnitudes and presumably lower effective temperatures. Depending on the distance, VHS 1256 b's $L'$/H-$L'$ position is either consistent with HR 8799 b's or appears more comparable to the inner three planets.

In contrast, VHS 1256 b is significantly brighter at $M'$, relative to HR 8799 bcde. VHS 1256 b's H-$M'$ color is 0.6–1.1 magnitudes redder that HR 8799 bcd, suggesting that at $M'$ it is roughly 1.7–2.7 times as bright. The Leggett et al. (2010) and Dupuy & Liu (2012) compilations of M/L/T objects (Figure 3.4) are more sparsely populated in $M'$ for late L and T dwarfs making comparisons with the field sequence difficult. As the faint $M'$ brightnesses for L/T transition

objects and the HR 8799 planets signaled evidence for non-equilibrium carbon chemistry (Galicher et al., 2011), VHS 1256 b's brighter $M'$ flux density may indicate that non-equilibrium carbon chemistry is not significant for every L/T transition object.

### 3.5.2 Atmospheric Modeling: Methodology

We perform atmospheric forward modeling to estimate VHS 1256 b's temperature, surface gravity, and radius, and to see if its photometry can be reproduced by atmospheric models in chemical equilibrium. We follow the studies of Currie et al. (2011) and Madhusudhan et al. (2011) for HR 8799's planets and Burrows et al. (2006) for field brown dwarfs, comparing the data with atmosphere models from A. Burrows covering a range of parameterized cloud prescriptions but all assuming chemical equilibrium.

We consider the "E60" models, which, have a modal particle size of 60 $\mu m$ and clouds sharply truncated at depth, well below the planet photosphere. We then consider "A60" and "AE60" cloud models, which have an identical modal particle size but simulate "very thick" and "thick" cloud model presciptions (see Burrows et al. 2006 and Madhusudhan et al. (2011) for details). From the model fitting, we identify those consistent with the data to within 3-$\sigma$ using a simple $\chi^2$ threshold, setting the minimum photometry uncertainty to be 10% as in Currie et al. (2011). This method then yields a plausible range of temperature, surface gravity, radius, luminosity and mass from the ensemble of acceptably-fitting models.

We perform two sets of model fits, one where we allow the planet radius to freely vary and another when we pin it to values implied in the Burrows et al. (2001) evolutionary models. We assess how the system's uncertain distance affects our best-fit derived by performing fits, for the fixed-radius case, assuming either

distances (12.7 and 17.1 *pc*).

### 3.5.3 Atmospheric Modeling: Results

Figure 3.5 displays best-fit models using each cloud model assumption and Tables 3.3 and 3.4 summarize our model fitting results. VHS 1256 b's SED cannot be reproduced by the thin-cloud, E60 models: like HR 8799's planets, such models badly under-predict the companion's brightness at the shortest wavelengths and over-predict it in the thermal infrared (see Currie et al., 2011). The A60, very-thick cloud models yield a drastically improved fit at temperatures between 900 $K$ and 1200 $K$, where a model with $T_{eff}$ = 1000 K, log(g) = 4.5 is marginally consistent with the optical to mid-infrared SED at the 3-$\sigma$ confidence limit.

Models with slightly thinner clouds, AE60, fare better, yielding a wider range of temperature and surface gravity phase space able to match the data. The best-fit values systematically skew towards lower temperatures and surface gravities, where the best fit model has $T_{eff}$ = 800 $K$ and log(g) = 3.8 when the radius can freely vary and has a slightly higher gravity (log(g) = 4.1) when the radius is fixed.

Assuming a distance of 17.1 *pc*, the implied luminosity of VHS 1256 b ranges between $\log(L/L_{\odot}) = -4.79$ to $-4.95$. Adopting the 12.7 *pc* distance yields a luminosity consistent with that previously estimated by Gauza et al. (2015): $\log(L/L_{\odot}) = -5.06$ to $-5.24$. We will estimate the mass of VHS 1256 b by using these luminosities in section 3.6.2. While successful at reproducing VHS 1256 b's SED, the derived model fit parameters could be revised by future modeling efforts. For instance, the implied radii for best-fit models are generally larger than predicted for substellar object's with ages greater than 150 $Myr$ (see Baraffe et al., 2003), and thus similarly the temperatures could be slightly larger than implied by our

analysis.

## 3.6 Discussion

### 3.6.1 Binarity of the Central Source

Subaru/IRCS AO $L'$and $M'$ imagery has clearly revealed that the central source of the VHS 1256 system is comprised of two objects (Figure 3.1) that have similar relative brightness ($L'$= 10.5 and 10.54 magnitude respectively). Such binarity is observed in $22^{+6}_{-4}$% of very low mass stars (Duchene & Kraus, 2013). Gauza et al. (2015) assigned the central source a spectral classification of M7.5, based on optical (M7.0) and IR (M8.0) spectral classifications. We speculate that the minor differences in the optical versus IR spectral classifications derived by Gauza et al. (2015) could be caused by minor differences in the spectral classifications of the binary components. At the observed distance to VHS 1256 ($12.7 \pm 1.0$ *pc*; Gauza et al. 2015), the $0\farcs103 \pm 0\farcs001$ projected separation between the binary components corresponds to a projected physical separation of $\sim$1.3 au. Our results on the binarity of the central source are consistent with those independently and recently reported by Stone et al. (2016).

### 3.6.2 System Age and Component Masses

Gauza et al. (2015) suggested a system age of 150-300 Myr, based on the lack of observed Li in the system and kinematic age constraints from being a Local Association member. However, with the discovery that the central source is a binary (Stone et al., 2016) and our independent verification of VHS 1256 A and B in the $L'$-band, we can reassess the age limits of the system. Using the nominal distance (12.7 pc) and the absolute magnitude ($M_{L'}$; $10.0 \pm 0.2$), the 300 Myr

upper limit age suggested by Gauza et al. (2015) results in an inferred mass for VHS 1256 A or B of 47 $M_J$. However such a mass would be too small to destroy Li (Allard, 2014) and produce the non-detection of this line (Figure 3.6). Rather, at this adopted distance the lower limit age of VHS 1256 must be $>$ 400 Myr to produce VHS 1256 A and B with our observed $M_{L'}$ and the lack of Li in the system's spectra. If one assumes the new distance of 17.1 pc proposed by Stone et al. (2016) and the corresponding absolute magnitude of the central components ($M_{L'}$; $\sim 9.4 \pm 0.3$), the lower age limit is $>$ 200 Myrs (Figure 5). This is broadly consistent with the lower age limit proposed by Stone et al. (2016) of $280^{+40}_{-50}$. Note we used models from Allard (2014), while Stone et al. used models from Chabrier et al. (2000).

Stone et al. (2016) suggested that VHS 1256 was consistent with being a member of the AB Dor moving group, based on analysis of its UVW kinematics and a 66.85% membership probability predicted by the BANYAN II software tool (Malo et al., 2013; Gagne et al., 2014). Our own investigation suggests that it still has a 28% chance of being in the "young field" (age up to 1 $Gyr$). Additionally, VHS 1256 b is a clear outlier in UWV space ($\sim 8 \pm 1.7$ km $s^{-1}$ from the core of AB Dor. (J. Gagne, pvt. comm.). Furthermore, membership in the $149^{+51}_{-19}$ Myr AB Dor moving group (Bell et al., 2015) is inconsistent with the lower age limit of $280^{+40}_{-50}$ proposed by Stone et al. (2016) and marginally inconsistent with our lower limit of 200–400 $Myr$. Moreover, the near-to-mid infrared colors of VHS 1256 A appear indistinguishable from those in the field and potentially bluer than AB Dor members (Figure 3.4. Thus, it is not clear that VHS 1256 is a member of the AB Dor moving group, as suggested by Stone et al. (2016).

As shown in Figure 3.6, the minimum mass of each central component of VHS 1256 (A and B) is $>$ 58 $M_J$ for both of the distances discussed above. This implies

that the wide companion, VHS 1256 b, has a minimum mass ranging from 10.5 to 26.2 $M_J$, as shown in Table 3.5. The large range is due to the uncertainty in the distance (12.7 or 17.1 pc) and the range in bolometric luminosities from atmospheric fitting (section 3.5). Though the lower estimate does dip below the deuterium burning limit, the companion is most likely in the brown dwarf regime.

### 3.6.3 Additional Companions and Formation

We detected no other point source companions in our field of view (FOV), $\sim$16.″5 x $\sim$16.″5 in $L'$and $\sim$9.″3 x $\sim$9.″3 in $M'$, down to our 5-$\sigma$ sensitivity limits shown in Figure 3.7. of 13.2 ($L'$; 12.5 mag at 17.1 pc). Assuming a distance of 12.7 (17.1) *pc*, minimum system age of $>$ 400 (200) Myr, and no flux reversal at $L'$ (i.e. that more massive objects are fainter), we can therefore exclude the presence of additional companions more massive than VHS 1256 b beyond 6 (8) au. For most of the semi major axis space we probe, comparisons with Baraffe et al. (2003) imply that companions down to 3–5 $M_{\rm J}$ can be excluded if the system is 200–400 *Myr* old.

Because we have failed to identify other substellar companions orbiting the primary, this severely restricts the possibility that VHS 1256 b was scattered to its present orbit by dynamical interactions with another, unseen planet. Thus far, searches for close-in substellar companions to stars with imaged (near) planet-mass companions at 100–500 au have failed to identify potential scatterers, suggesting that this class of objects formed in situ either from protostellar disk or molecular cloud fragmentation (Bryan et al., 2016).

Furthremore, the mass ratio (q) of VHS 1256 b (M$\sim$18.4 $M_J$; median lower limit between 10.2-26.2 $M_J$) to VHS 1256 A+B (M$\geq$116 $M_J$) is $\sim$0.16. This mass ratio is substantially larger than that observed for other imaged planetary systems

such as HR 8799 ($q \sim 5 * 10^{-3}$; Fabrycky & Murray-Clay 2010) and ROXs 42B (q $\sim$ 0.008-0.01; Currie et al. 2014a). Rather, it is more similar to that observed for low mass BDs (q $\sim$ 0.01-0.9; eg. see Figure 4, Currie et al. 2014a and citations there in). We suggest this is indicative that the system formed via some form of fragmentation, i.e. a binary-star-like formation mechanism, rather than core accretion (Pollack et al., 1996). Stone et al. 2016 reached a similar conclusion of the binary-star-like formation.

### 3.6.4 Atmospheric Modeling

Although VHS 1256 b occupies a similar near-IR color-magnitude space to HR 8799 bcde (Gauza et al., 2015), its significantly older age than the HR 8799 system enables one to probe a different time frame in planet/brown dwarf atmospheric evolution. VHS 1256 b and HR 8799 bcd(e?) have different spectral energy distributions at the longest wavelengths probe ($M'/4.7\ \mu m$). In the now-standard picture of understanding the atmospheres of the youngest and lowest-mass L/T objects, thick clouds and non-equilibrium carbon chemistry both are due to the objects' low surface gravity (e.g. Marley et al., 2012). That VHS 1256 b thus far lacks evidence for non-equilibrium carbon chemistry may complicate this picture, suggesting some decoupling of gravity's two effects or that VHS 1256 b's gravity is high enough that non-equilibrium effects are less obvious than they are for, say, HR 8799 b.

Higher signal-to-noise detections in $M'$ and photometry in the 3–4 $\mu m$ range probing methane will allow us to better clarify VHS 1256 b's carbon chemistry. Multiple lines in $J$ band resolvable at medium resolution could better clarify the companion's surface gravity. With other, similar objects detected at a range of ages, we can better map out the atmospheric evolution of objects of a given mass

as well as the diversity of objects occupying the same reddened L/T transition region where VHS 1256 b and bona fide planets like HR 8799 bcde reside.

### 3.6.5 System Architecture

The VHS 1256 hierarchical triple system is poised to become an important contributor to our understanding of VLM systems. It represents the third hierarchical triple system comprised solely of brown dwarf-mass components known (Bouy et al., 2005; Radigan et al., 2013). Given this projected separation (1.3 au) and associated approximate orbital period (∼4.7 years) of the central binary in VHS 1256, future AO spectroscopic monitoring of the system is poised to determine dynamical masses of all components of the triple system, which should help constrain evolutionary models (see e.g. Dupuy et al. 2010). Since at least some brown dwarf binaries are believed to form via the disintegration of triple systems, and the third body in such systems are most likely also brown dwarf mass object (Reipurth & Mikkola, 2015), robustly determining the fundamental properties of the few known triple systems like VHS 1256 could help test the predictions of dynamical simulations of BD formation and evolution.

## 3.7 Acknowledgements

This chapter is reproduced by permission of the American Astronomical Society from the following publication: Rich, E. A., Currie, T., Wisniewski, J. P., et al. 2016, ApJ, 830, 114 , "Thermal Infrared Imaging and Atmospheric Modeling of VHS J125601.92-125723.9 b: Evidence for Moderately Thick Clouds and Equilibrium Carbon Chemistry in a Hierarchical Triple System". Here is the original publications author list: Evan A. Rich, Thayne Currie, John P. Wisniewski,

Jun Hashimoto, Timothy D. Brandt, Joseph C. Carson, Masayuki Kuzuhara, and Taichi Uyama

We thank Sarah Schmidt for thoughtful discussions about L/T dwarfs and multiplicity and Jonathan Gagne for helpful comments on VHS 1256's possible membership in different moving groups. We acknowledge support from NSF-AST 1009314 and NASA's Origins of Solar Systems program under NNX13AK17G. This work was performed in part under contract with the Jet Propulsion Laboratory (JPL) funded by NASA through the Sagan Fellowship Program executed by the NASA Exoplanet Science Institute. This work is also based on data collected at Subaru Telescope, which is operated by the National Astronomical Observatory of Japan. The authors recognize and acknowledge the significant cultural role and reverence that the summit of Mauna Kea has always had within the indigenous Hawaiian community. We are most fortunate to have the opportunity to conduct observations from this mountain.

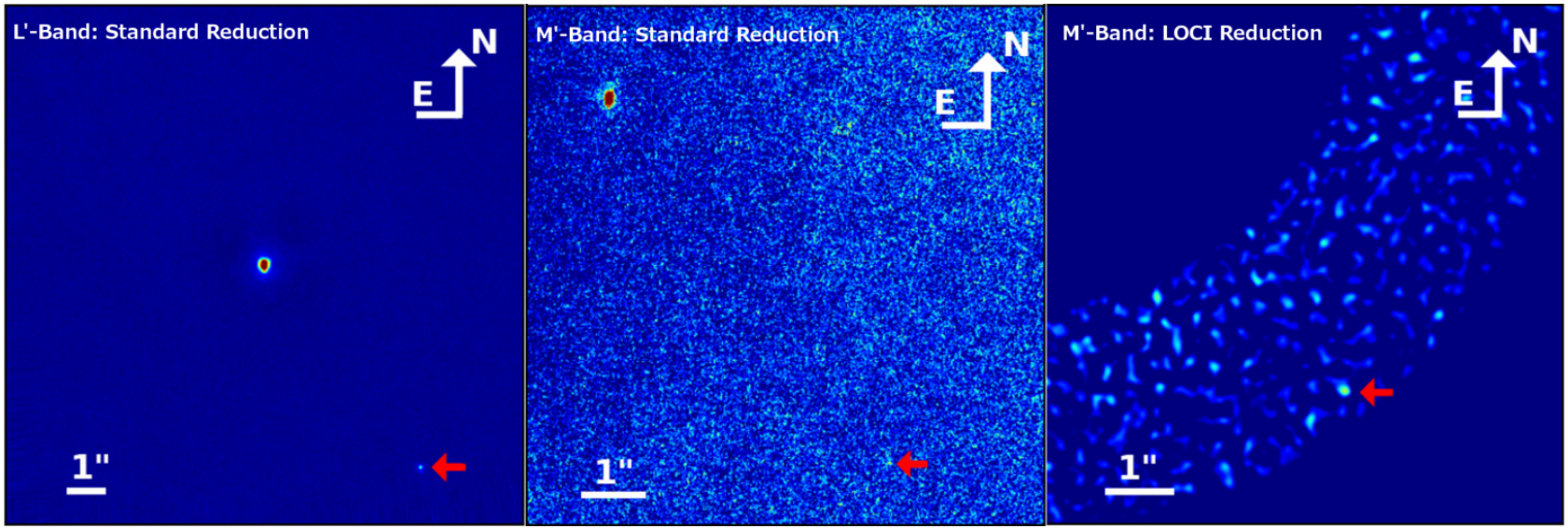


Fig. 3.1.— Subaru/IRCS $L'$-band ($\sim$16.″4 x $\sim$16.″4 FOV; left panel), $M'$-band ($\sim$9.″5 x $\sim$9.″5 FOV; middle panel), and $M'$-band ($\sim$8.″5 x $\sim$8.″4 FOV; LOCI reduction; 3 sigma filter applied; right panel) AO observations of the VHS 1256 system. Left and center panels show the full usable FOV with the partially resolved binary in the left and center panel and VHS 1256 b previously detected by Gauza et al. (2015) in all three panels. The red arrow depicts the location of VHS 1256 b. Note that no other point sources are detected in the FOV. The data are plotted on a linear intensity scale.

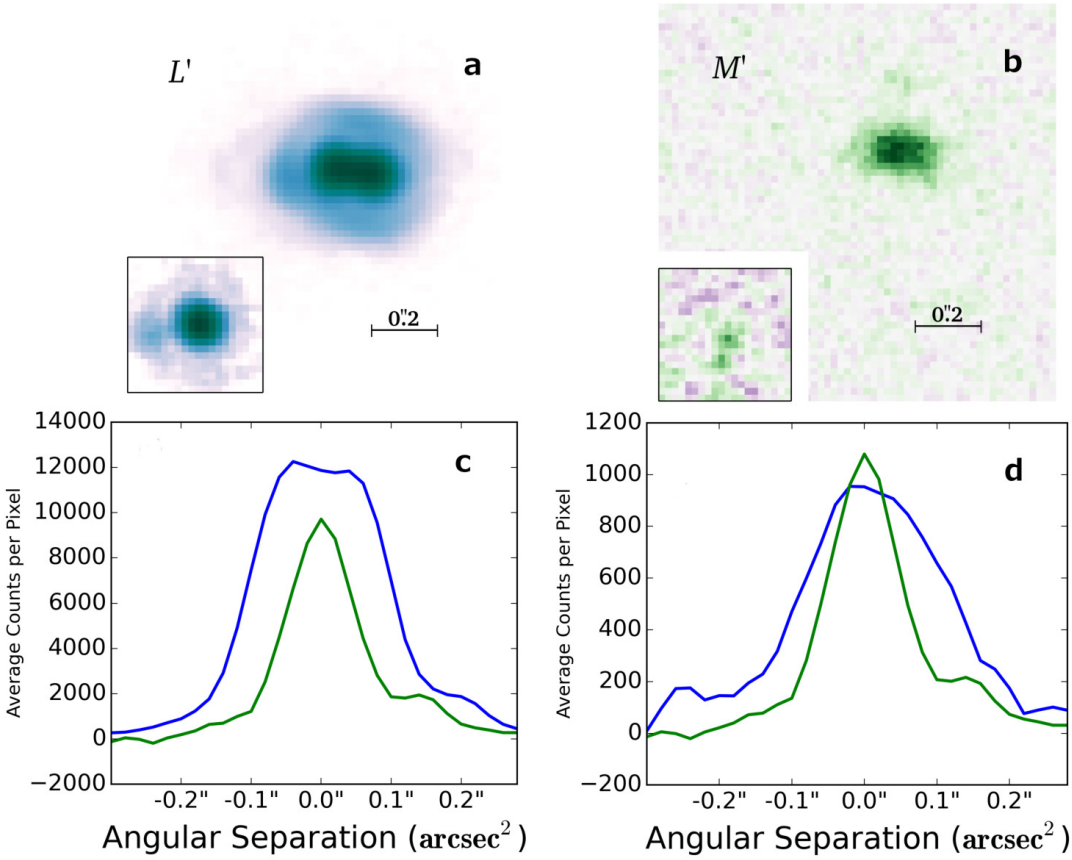


Fig. 3.2.— The ellipticity of VHS 1256 A and B in $L'$(panels a and c) and $M'$ (panels b and d) can be seen above. Panels a and b show a FOV (1.″3 X 1.″3) of VHS 1256 A and B in their respective band-passes with north to the left and east up. The insert in panels a) and b) is of VHS 1256 b used as the PSF. Note that the panel b) insert used the A-LOCI reduction rather than the first reduction method. Panels c and d are crosscuts along the major axis of the central source (blue) and PSF (green), averaged over 5 pixels. The clear double-peak profile in panel c illustrates that we partially resolve the central source in $L'$.

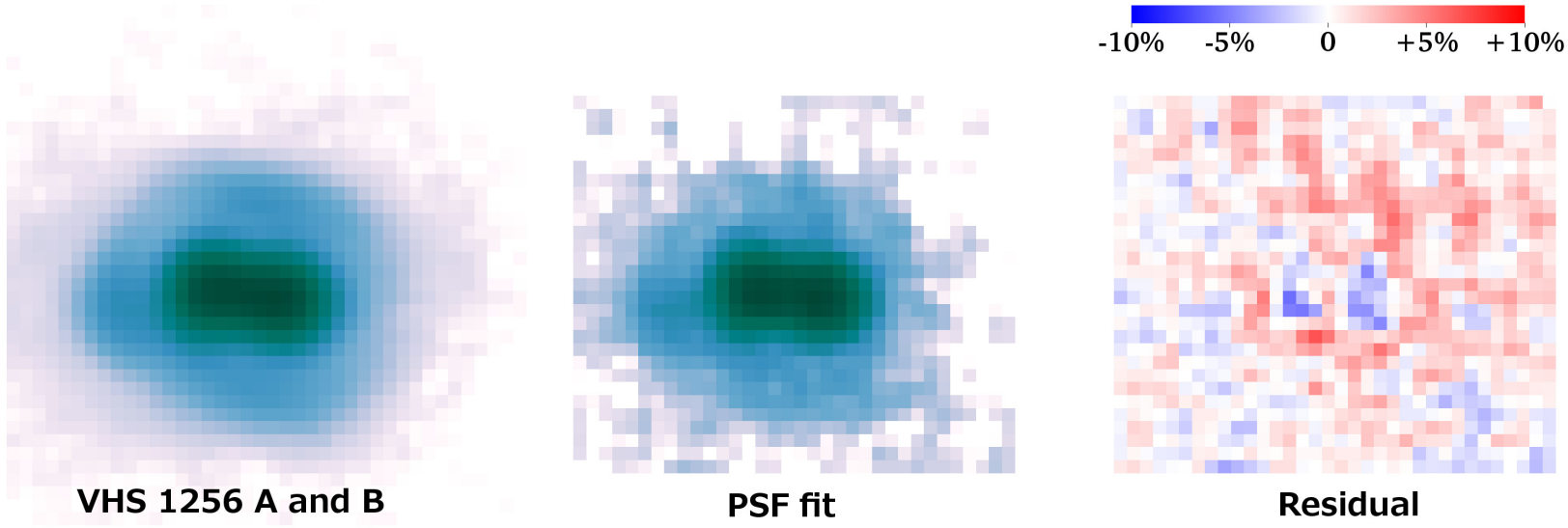




Fig. 3.3.— The above shows PSF fitting of VHS 1256 A and B utilizing our $L'$-band data. The left panel shows a view of VHS 1256 A and B. The middle panel shows the best fit result using VHS 1256 b as an observed PSF. The right panel shows the residual of the PSF fit.

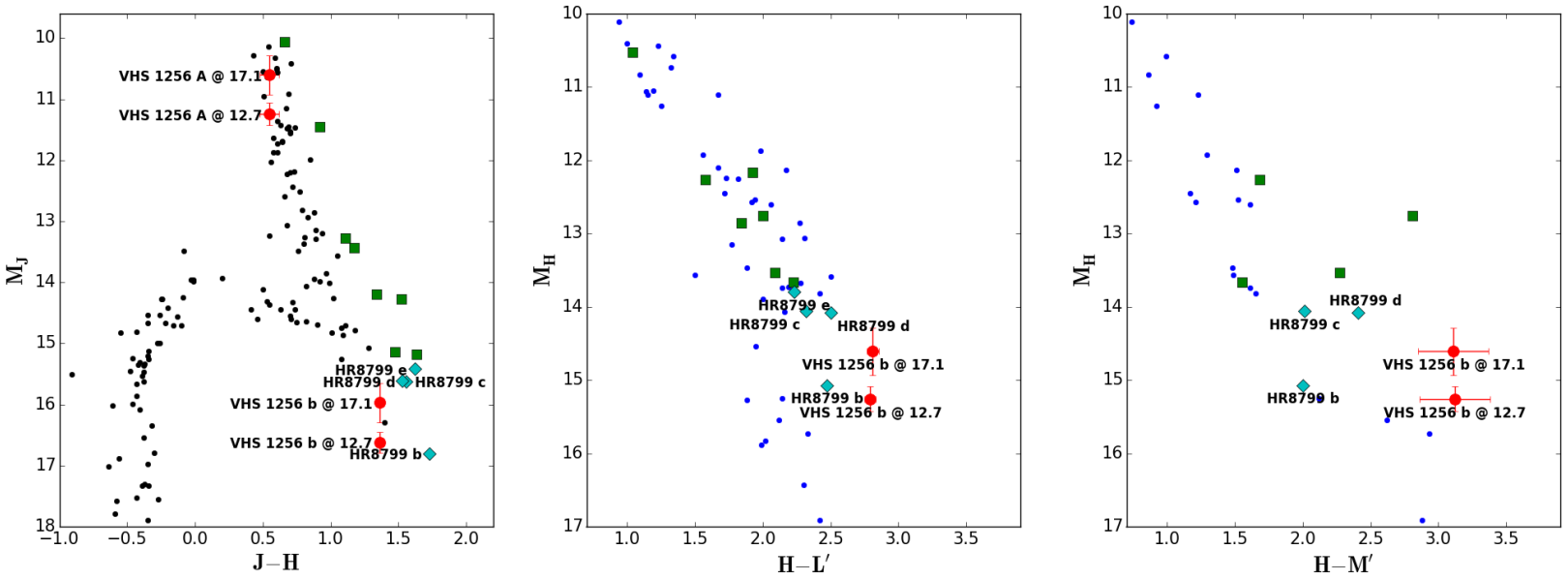


Fig. 3.4.— Near-IR color magnitude diagrams in J-H (right panel) and H-$M'$ (left panel) space are shown. For both panels, the red circles are VHS 1256 A and b for both 12.7 and 17.1 *pc* distances ((Gauza et al., 2015; Stone et al., 2016)), the blue circles are HR 8799 bcde and L/T dwarfs with $M'$ photometry (Leggett et al., 2002; Currie et al., 2014b), the green circles are members of the AB Dor moving group (Faherty et al., 2016), and the black cicles are M/L/T field dwarfs Dupuy & Liu (2012). Note that VHS 1256 b is consistent in color with HR 8799 b in J-H space (right panel) but VHS 1256 b has a much redder color in H-$M'$ space (left panel).

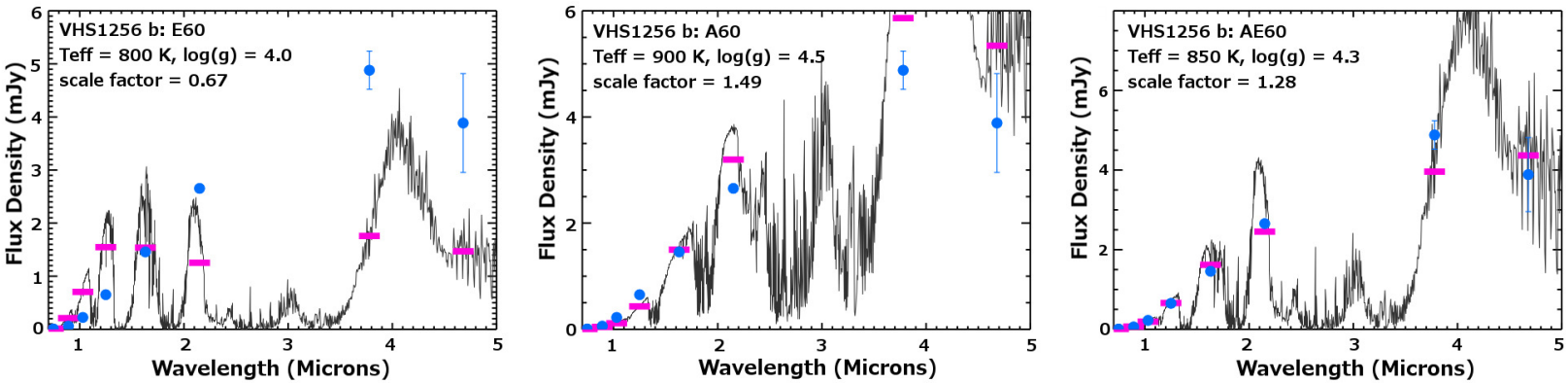


Fig. 3.5.— Best-fit atmosphere models for the thin-cloud E60 model (left panel), the very-thick cloud A60 model (middle panel), and the thick cloud AE60 model (right panel). The (very) thick cloud models accurately reproduce the optical to mid-IR SED of VHS1256 b. Black lines is the model spectra, the magenta points are the model spectra applied to the appropriate filter, and the blue points are photometry that match the magenta filter points.

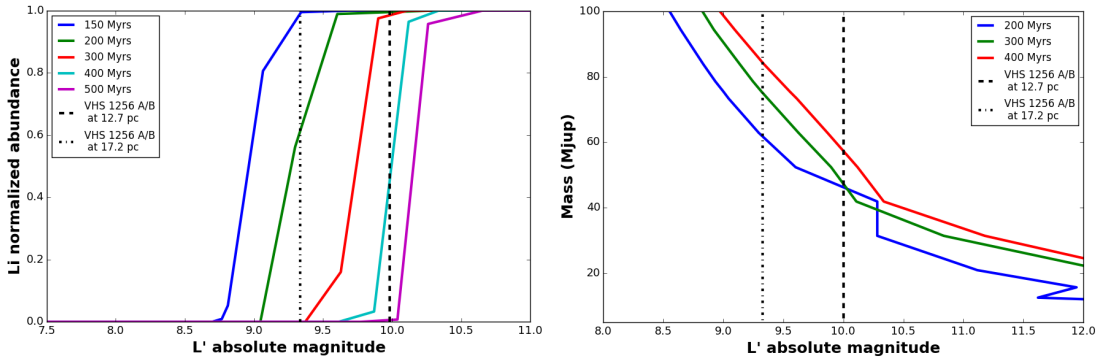


Fig. 3.6.— The above figures demonstrate the age of the VHS 1256 system (left panel), and the estimated lower mass limit of VHS 1256 A and B (right panel). The left panel plots the normalized lithium abundance against the absolute L' magnitude taken from BT-Settl models (Allard, 2014) for a variety of ages. The absolute magnitudes of VHS 1256 A and B (both 12.7 and 17.1 *pc* distances) are taken from the PSF fit shown in table 3.5, plotted as the vertical dashed lines. Unresolved spectroscopy of stars A and B from Gauza et al. (2015) showed no detection of lithium down to 30 $m\mathring{A}$, thus these stars must be old enough to have destroyed the initial lithium. The best lower limit ages based no the non-detection of lithium are $>$ 200 Myrs (17.1 *pc*) or $>$ 400 Myrs (12.7 *pc*). The right panel plots the sub-stellar mass ($M_J$) against the absolute L' magnitude taken from BT-Settl models. The solid lines are three different BT-Settl models: 200 Myrs for the 17.1 *pc* distance, 400 Myrs for the 12.7 *pc* distance, and 300 Myrs for the Gauza et al. (2015) upper age limit. The estimated lower mass limit for VHD 1256 A and B for both 12.7 and 17.1 *pc* distances is $>$ 58 $M_J$.

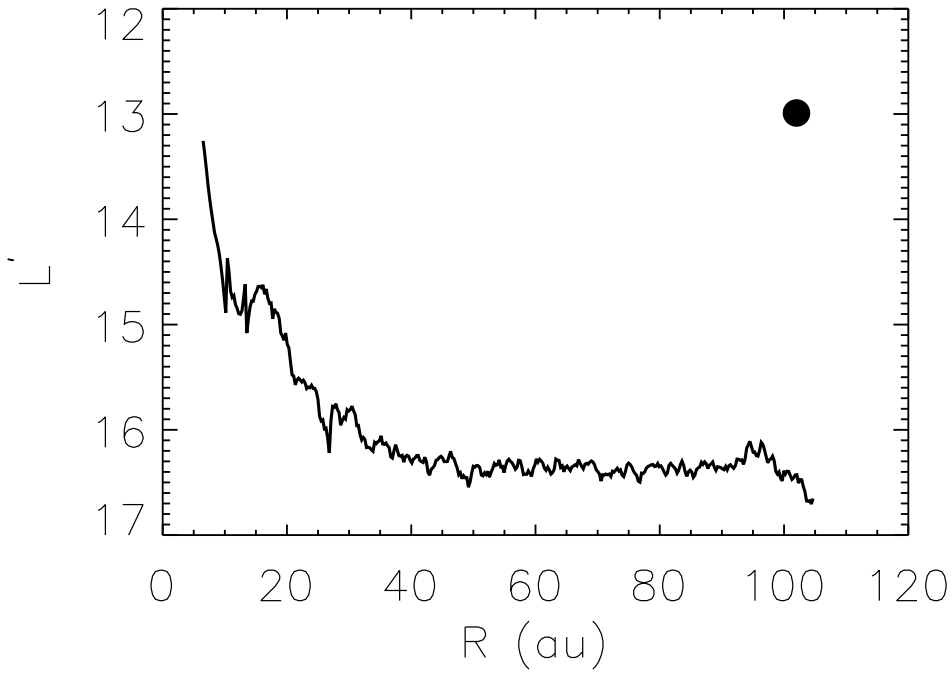


Fig. 3.7.— Limiting background limit as a function of projected radius from VHS 1256 (A+B) for $L'$ imagery with the A-loci reduction. The projected radius assumes a VHS 1256 distance of 12.7 *pc* The black line is the 5-sigma background limit and the black dot is VHS 1256 b.

| VHS 1256 Objects and Band | System Properties |
|---|---|
| A and B separation ($L'$) | $0\farcs1056 \pm 0\farcs001$ |
| A and B PA ($L'$) | $-6° \pm 2°$ |
| A and B Est. Period ($L'$) | 4.7 yrs |
| A apparent magnitude ($L'$) | 10.50 ±0.01 mag |
| B apparent magnitude ($L'$) | 10.54 ±0.01 mag |
| A+B and b separation ($L'$) | 8."13 ± 0."04 |
| A+B and b PA ($L'$) | 217.8 ± 0.3 ° |
| A+B and b separation ($M'$) | 8."17 ± 0."04 |
| A+B and b PA ($M'$) | 217.8 ± 0.3 ° |

Table 3.1:: VHS 1256 Astrometry and Magnitudes. The measured and derived for VHS 1256 A, B, and b in $L'$and $M'$ using centroid positions and PSF fitting.

| Photometry Band | VHS 1256 A and B (mag) | VHS 1256 b (mag) |
|---|---|---|
| L' | 9.76 ± 0.03 | 12.99 ± 0.04 |
| M' | 9.65 ± 0.05 | 12.66 ± 0.26 |
| W1 | 9.880 ± 0.023 | 13.6 ± 0.5 |
| W2 | 9.658 ± 0.021 | 12.8 ± 0.5 |

Table 3.2:: VHS1256 Aperture Photometry. L' and M' aperture photometry taken from traditional reductions described in section 4.2 with the exception of M' photometry of VHS 1256 b which used the LOCI reduction described in section 4.2. The WISE data was taken from Gauza et al. (2015).

| Model | Best-Fit Model $T_{eff}$ (K), log(g), Radius ($R_J$) | Models Matching Within 3-$\sigma$ $T_{eff}$ (K), log(g), Radius ($R_J$) |
|---|---|---|
| Burrows/A60 | 1000, 4.5, 1.34 | 1000, 4.5, 1.34 |
| Burrows/AE60 | 800, 3.8, 1.8 | 700, 3.5–4, 2.57-2.64 |
| | | 750, 3.5–4.3, 2.03-2.25 |
| | | 800, 3.5–4.5, 1.74-1.95 |
| | | 850, 3.5–4.3, 1.60-1.64 |
| | | 900, 3.5-3.9, 1.35, 1.42 |
| Burrows/E60 | 1000, 4.0, 0.98 | – |

Table 3.3:: Atmosphere modeling results shown in increments of 50 $K$. The radii quoted assume the revised parallax from Stone et al. (2016). Owing to uncertainty in VHS 1256-12's parallax from that paper, the best-fit radii have an additional systematic uncertainty of $\approx 10\%$. Radii assuming a nominal distance of 12.7 $pc$ are systematically $\approx 35\%$ smaller.

| Model | Best-Fit Model $T_{eff}$ (K), log(g), Radius ($R_J$) | Models Matching to Within 3-$\sigma$ $T_{eff}$ (K), log(g), Radius ($R_J$) |
|---|---|---|
| *d = 17.1 pc* | | |
| Burrows/A60 | 1000, 4.25, 1.45 | – |
| Burrows/AE60 | 850, 3.8, 1.55 | 850, 3.5–3.9, 1.48–1.75 |
| Burrows/E60 | 700, 4.0, 1.45 | – |
| | | |
| *d = 12.7 pc* | | |
| Burrows/A60 | 900, 4.25, 1.29 | – |
| Burrows/AE60 | 800, 4.1, 1.36 | 750, 3.5–3.8, 1.53–1.73 |
| | | 775, 3.8–4.1, 1.35–1.53 |
| | | 800, 4.0–4.3, 1.25–1.41 |
| | | 850, 4.3, 1.26 |
| Burrows/E60 | 700, 4.0, 1.45 | – |

Table 3.4:: Atmosphere Model Fitting Results (Fixed Radius). Atmosphere modeling results, shown in increments of 25 $K$. As before, for a given parallax assumption the best-fit radii have an additional systematic uncertainty of $\approx 10\%$.

| Object | Measurement at 12.7 ± 1.0 pc | Measurement at 17.1 ± 2.5 pc |
|---|---|---|
| A Absolute magnitude ($L'$) | 10.0 ± 0.2 mag | 9.3 ± 0.3 mag |
| B Absolute magnitude ($L'$) | 10.0 ± 0.2 mag | 9.4 ± 0.3 mag |
| Age lower limit | > 400 Myrs | > 200 Myrs |
| A and B Mass BT-Settll[a] (L') | 58 $M_J$ | 58 $M_J$ |
| b Absolute Magnitude (L') | 12.5 ± 0.2 mag | 11.8 ± 0.3 mag |
| b Mass BT-Settl[a] (L') | 26.2 to 74 $M_J$ | 15.7 to 75 $M_J$ |
| b Bolometric Luminosity log($L/L_{sun}$) | -5.06 to -5.24 | -4.79 to -4.95 |
| b Mass BT-Settl[a] Bolometric | 12.6 - 20.6 $M_J$ | 10.5 - 15.7 $M_J$ |
| Limiting Absolute Magnitude at 2.″8 (L') | 15.6 | 14.9 |
| Limiting Magnitude Mass SB12[b] models (L') | $\sim$ 10 $M_J$ | $\sim$ 10 $M_J$ |
| Limiting Magnitude Mass BT-Settl[a] models (L') | 5 $M_J$ | 7.8 $M_J$ |



Table 3.5:: VHS1256 Absolute Magnitudes and Masses. The measured and derived parameters for VHS 1256 A, B, and b in $L'$and $M'$. a) BT-Settle model from Allard (2014). b) SB12 models from Spiegel & Burrows (2012).

# Chapter 4

# Multi-Epoch Direct Imaging and Time-Variable Scattered Light Morphology of the HD 163296 Protoplanetary Disk

## 4.1 Introduction

Protoplanetary disks are dust and gas disks around young stars that guide the accretion of material onto forming stars and serve as the birthplace of planets. Direct imaging of protoplanetary disks reveals likely sites of active planet formation, may identify planets in the final stages of assembly (protoplanets), and probes the interaction between protoplanets and the disk material from which they form. Herbig Ae/Be stars (Herbig , 1960), the intermediate mass analogs to T Tauri stars, are known to both host protoplanetary disks and often exhibit evidence of ejecting material via collimated, bi-polar jets (Herbig , 1950; Grady et al., 2000; Ellerbroek et al., 2014; Bally, 2016). The protoplanetary disks around Herbig Ae/Be stars exhibit a variety of structures – with some hosting spiral arms (Hashimoto et al., 2011) and others that are flat and settled causing self-shadowing of the disk (Meeus et al., 2001) – and may host some of the first directly-imaged jovian protoplanets (Quanz et al., 2013; Currie et al., 2015).

HD 163296 is a young ($5.1^{+0.3}_{-0.8}$ Myr old Montesinos et al. 2009 to $7.6^{+1.1}_{-1.2}$ Myr old Vioque et al. 2018) Herbig Ae protoplanetary disk system located at a distance of $101.5 \pm 1.2$ *pc* (Gaia Collaboration et al., 2016, 2018). The disk has been spatially resolved by ground- and space-based observing platforms at a multitude of wavelengths, including: optical (HST/STIS: Grady et al. 2000, HST/ACS Wis-

niewski et al. 2008), near-infrared (IR) (VLT/NACO: Garufi et al. 2014, 2017, Gemini/GPI: Monnier et al. 2017, VLT/SPHERE: Muro-Arena et al. 2018, Subaru/CIAO: Fukagawa et al. 2010, Keck/NIRC2: Guidi et al. (2018)), and radio wavelengths (VLA: Guidi et al. 2016, ALMA: Guidi et al. 2016; Isella et al. 2016).

Spatially-resolved imaging observations have revealed a complex circumstellar environment and evidence for active planet formation at wide separations around HD 163296. Its disk extends to at least to $4\farcs4$ (447 AU) in optical scattered light (Wisniewski et al., 2008). While near-IR observations reveal a 64 AU-scale inner dust ring (Garufi et al., 2014, 2017; Monnier et al., 2017; Muro-Arena et al., 2018), 1.3 mm continuum ALMA imaging (Isella et al., 2016) revealed three azimuthal gaps in the disk located at $0\farcs49$, $0\farcs82$, and $1\farcs31$ (50, 83, and 133 au respectively given GAIA-DR2 distance of 101.5 pc). The surface distribution of small dust grains in the outer disk appears low, owing to settling or partial-to-complete depletion (Muro-Arena et al., 2018). Keck/NIRC2 thermal infrared imaging led to the discovery of a candidate 7 $M_{\rm J}$ protoplanet just exterior to the inner ring (Guidi et al., 2018), while modeling of ALMA gas emission data suggest Jovian planets at 83 and 137 au (Teague et al., 2018) and/or a single Jovian on an even wider orbit (260 au Pinte et al., 2018).

Multi-epoch observations have revealed a wealth of variability in the HD 163296 system likely traceable to dynamical processes in the inner disk region. Both IR spectra and visibilities from optical inteferometry show variability possibly connected to changes in the inner disk or the system's wind component (Sitko et al., 2008; Tannirkulam et al., 2008). Long-term optical photometric and IR spectroscopic monitoring revealed suggestive evidence of a 16 year periodicity, with optical fluxes dimming when the IR fluxes reach a maximum level (Ellerbroek et al., 2014; Sitko et al., 2008), on similar timescales as the ejection of Herbig-Haro

objects (Ellerbroek et al., 2014). The star's accretion rate increased over 1 dex over $\sim$ 15 years (Mendigutía et al., 2013). However, no clear correlation between these variations and the 16 year optical infrared periodicity has yet been found. CO ro-vibrational emission lines exhibit variability possibly connected to changes in the disk wind or episodic accretion (Hein Bertelsen et al., 2016).

Spatially-resolved imaging may also reveal evidence for variability – time-dependent changes in the disk's surface brightness and morphology potentially linked to variable illumination (Wisniewski et al., 2008). However, despite this plethora of variability observed, the lack of contemporaneous observations of both the inner and outer regions of the HD 163296 disk limits efforts to connect these phenomenon to one another.

In this paper, we present multi-epoch near-infrared scattered light imaging of HD 163296, obtained at $H$-band in polarized light as part of the Strategic Exploration of Exoplanets and Disks with Subaru (SEEDS) survey (Tamura , 2009) and in total intensity in $JHK$ using *Subaru Coronagraphic Extreme Adaptive Optics* (SCExAO) (Jovanovic et al., 2015a) coupled with the CHARIS integral field spectrograph (Section 4.2). To help parse and complement these data probing the outer disk, we acquired near-contemporaneous IR spectra to characterize the inner disk region of the system. We modeled the H-band scattered light images and near-IR spectra using a well-established 3D Monte Carlo Radiative Transfer code to create a more coherent, full picture of the system at this epoch (Section 5.3). Finally we discuss the implications of our results in Section 5.5 including deeper constrains on protoplanets around HD 163296 with the new SCExAO/CHARIS data.

## 4.2 Observations and Data Reduction

### 4.2.1 HiCIAO Imagery

We obtained high contrast H-band imaging of HD 163296 using the HiCIAO instrument (Hodapp et al., 2008) along with the AO-188 system (Hayano et al., 2008, 2010) at the Subaru Observatory on 2011 August 3. We used a circular occulting mask having a diameter of 0.″3, and observed the system in standard Polarized Differential Imaging (sPDI) mode at four wave-plate positions (0°, 22°.5, 45°, 67°.5). We obtained 72 frames using 30 second exposures, yielding a total of 18 complete wave-plate sets. We determined that 8 wave-plate sets had lower AO performance, and discarded them during the reduction of the data. We also obtained a short, direct H-band photometric observation of HD 163296, and determined that the source's brightness at this epoch was 5.62 ± 0.05 mag.

We reduced our observations using standard double differencing techniques, as described in Hashimoto et al. (2011). To briefly summarize, the two sub-images of each frame contain an ordinary and an extra-ordinary image, which can be summed and subtracted from their 90° counterparts to create stokes parameter −Q, +Q, −U, and +U images. The Q and U frames were then rotated into a common orientation, corrected for instrumental polarization, and summed to create final Q and U images. We corrected these data for the presence of a residual polarized halo having the properties of p = 1.00 ± 0.05% and $\theta$ = 42.5 ± 1.5°. Final polarized intensity (PI) imagery was created from the total Q and U data, using $PI = \sqrt{Q^2 + U^2}$, as shown in Figure 4.1.

To further simplify the analysis of our imagery, we adopt the now common practice of assuming single scattering, and rotated all of the light that is polarized perpendicular to the star by the angle $\phi$ into a $Q_\phi$ image and all of the light that

is polarized parallel to the star into a $U_\phi$ image as defined below (Schmid et al., 2006).

$$Q_\phi = Q \times \cos 2\phi + U \times \sin 2\phi \quad (\mathbf{4.1})$$

$$U_\phi = Q \times \sin 2\phi + U \times \cos 2\phi \quad (\mathbf{4.2})$$

The final $Q_\phi$ and $U_\phi$ imagery for HD 163296 are shown in Figure 4.1. Little coherent signal appears present in the $U_\phi$ image, which helps confirm that little residual instrumental contaminants remain in these data. Next, we computed a signal to noise (SN) image, following the procedure outlined by Ohta et al. (2016). In summary, we computed the noise by measuring the standard deviation of every pixel in each of the Q and U frames used to construct the final imagery, then divided by the square root of the number of frames. The resultant SN image is shown in Figure 4.1.

### 4.2.2 Near-Infrared Spectra from SpeX, BASS, and TripleSpec

We also observed HD 163296 multiple times with several near-IR instruments on NASA's Infrared Telescope Facility (IRTF) and at Apache Point Observatory (APO). We observed HD 163296 using the SpeX spectrograph (Rayner et al., 2003) at IRTF in its short-wavelength mode (0.8 - 2.4 $\mu m$) and long-wavelength mode (2.3-5.5 $\mu m$) on 2011 July 31, 2016 May 4, and 2018 June 24. These observations are contemporaneous with the HiCAIO 2011 observation (Section 4.2.1), the Gemini/GPI observation (Section 4.5.1), and the second SCExAO/CHARIS observations (Section 4.2.3) respectively. We observed HD 163296 using the Triple-

Spec spectrograph (Wilson et al., 2004) at the APO 3.5m telescope, covering a spectral range of (0.95 - 2.46 $\mu m$), on 2018 May 16. This observation is contemporaneous with the first SCExAO/CHARIS observation (Section 4.2.3). We observed the nearby A0V star HD 163336 to perform telluric corrections for both the SpeX and TripleSpec observations. These data were reduced and calibrated using the standard reduction packages *Spextool* and *Triplespectool* (Vacca et al., 2003; Cushing et al., 2004). We also observed HD 163296 with The Aerospace Corporation's Broad-band Array Spectrograph System (BASS), which covers two wavelength bands from 2.9-6 $\mu m$ and 6-13.5 $\mu m$ respectively, on 2011 August 1. HD 163336 was observed with BASS to flux calibrate these data. The instrument and data reduction method are fully described in Wagner et al. (2015). These SpeX, TripleSpec, and BASS spectra are plotted in Figure 4.2.

### 4.2.3 SCExAO/CHARIS High-Contrast Near-Infrared Spectroscopy

We observed HD 163296 on 2018 May 22 and 2018 July 1 at the Subaru Observatory with SCExAO coupled with the CHARIS integral field spectrograph operating in low-resolution ($R \sim 20$), broadband (1.13–2.39 $\mu$m) mode, covering the $JHK$ filters simultaneously (Groff et al., 2015). For the May observations, the conditions were stable with $0\farcs4$ seeing and 6–7 m s$^{-1}$ winds. Our observations consisted of co-added 60.4-second frames totaling ∼30 minutes of integration time and covering a modest parallactic angle rotation ($\Delta$PA = $14.8^o$). Due to highly variable conditions for the July observations, we obtained shorter exposures (30.9 $s$) and removed roughly 50% of the frames with poor AO correction, yielding ∼ 40 minutes of data covering $30.9^o$ of parallactic angle motion[a].

[a]While a real-time estimate of the Strehl ratio (S.R.) was not recorded for these data sets, the raw contrast for the May data was just slightly poorer than that obtained for $\kappa$ And obser-

We followed the standard setup used for SCExAO/CHARIS broadband observations (Currie et al., 2018b; Goebel et al., 2018), using the Lyot coronagraph with the 217 mas occulting spot and bracketing our coronagraphic sequence with blank sky frames to remove sky emission and instrumental artifacts. We used satellite spots produced from a 25 nm modulation on SCExAO's deformable mirror for spectrophotometric calibration and image registration (Jovanovic et al., 2015b). For data cube extraction, we utilized the least-squares algorithm from the CHARIS Data Reduction Pipeline (Brandt et al., 2017). Basic data processing, including sky subtraction, image registration, etc., follows methods used for recent SCExAO/CHARIS broadband studies (Currie et al., 2018a,b; Goebel et al., 2018).

Spectrophotometrically calibrating CHARIS data for pre-transitional disk sources like HD 163296 require either observations of a separate spectral standard or contemporaneous near-IR spectra. We opt for the latter, using the IRTF/SpeX and APO/Triplespec data previously discussed in Section 4.2.2. The spectra show only minor differences between epochs.

We explored a range of point-spread function (PSF) subtraction approaches leveraging on *angular differential imaging* (ADI Marois et al., 2006), *spectral differential imaging* (SDI Sparks and Ford, 2002), and combinations of the two (ASDI, e.g. Marois et al., 2014). We further considered a variety of PSF subtraction algorithms, including A-LOCI (Currie et al., 2012, 2018b), KLIP (Soummer et al., 2012), and classical PSF subtraction (Marois et al., 2006). The approach implemented for $\kappa$ And in Currie et al. (2018b), using A-LOCI to subtract the PSF in ADI and then again to remove residuals in SDI mode, yielded the best speckle suppression while preserving the signal from the disk. Due to the limited

vations achieving S.R. $\sim$ 0.90–0.92 in $H$ band (Currie et al., 2018b). Raw contrasts for the July data considered in our study are roughly a factor of 2.5–3 worse at $0\farcs4$, more characteristic of performance at S.R. $\sim$ 0.65–0.70.

parallactic angle motion of both data sets (especially in May) and the presence of the disk, we utilized large optimization zones for the ADI step, employed local masking in the SDI step, and imposed a rotation/magnification criterion of $\delta =$ 0.5–1.0 PSF footprints in both steps to construct a reference PSF (see Lafrenière et al., 2007). For both steps, we used a *singular value decomposition* (SVD) cutoff of $10^{-6}$ to solve the set of linear equations that result in the weighted reference PSF for each region of each data cube slice (see Currie et al., 2015).

Figure 4.3 shows broadband (wavelength-collapsed) CHARIS images of HD 163296 from SCExAO/CHARIS for the May (left) and July (right) epochs after removing the stellar PSF through both ADI and SDI. Despite poor field rotation (May data) or variable conditions (July data), we clearly detect the outer ring of emission seen in polarimetry, which appears as a sharply-defined crescent defining the forward-scattering edge of the structure. Self-subtraction footprints due to both ADI and SDI flank the ring. In individual passbands, the disk is just marginally visible in $J$ band but is well separated from residual speckle noise in $H$ and $K$.

We defined a conservative lower limit to the signal-to-noise (SNR) ratio of the trace of the disk in broadband, adopting the standard practice of replacing each pixel by the sum within its aperture, defining a radial-dependent noise profile, and applying a finite-element correction for the noise (Currie et al., 2011; Mawet et al. , 2014). To be conservative, we include signal from the disk in our estimate of the noise profile. Except at the semi-minor axis, where the disk signal is attenuated by self-subtraction, the disk trace is decisively detected, with a SNR per resolution element ranging from 3 to 8.5.

Our data do not reveal the candidate protoplanet identified in Keck/NIRC2 $L_{\rm p}$ data from Guidi et al. (2018) nor the companions predicted from ALMA data

(Teague et al., 2018). The inner disk seen by GPI polarimetry (Monnier et al., 2017) is also not visible, likely due to heavy self-subtraction due to poor field rotation. The position of the Guidi et al. candidate lies well separated from the ring and residual speckle noise; the SNR maps show no convolved pixel within one PSF footprint ($\sim 0\farcs08$) of this position with a significance greater than $1.3\sigma$. More conservative reductions (e.g. larger rotation gap; higher SVD cutoff) may show slightly elevated residual emission consistent with additional extended structure at this separation (e.g . additional ring material). However, this signal is not statistically significant and is simpler to explain as residual speckle noise instead.

## 4.3 Analysis of the H-band Polarimetry Data

In this section, we characterize the distribution of scattered light in our H-band imagery, and construct a Monte Carlo Radiative Transfer (MCRT) model to help interpret the contemporaneous H-band scattered light imagery and near-IR spectra.

### 4.3.1 Geometry of the Disk

Figure 4.1 reveals the clear detection of scattered light surrounding the HD 163296 disk in our H-band imagery outside of the inner working angle of these data, $0\farcs3$ (30.5 au). The scattered light imagery reveals a broken ring structure that peaks at a distance along the major axis of $0\farcs65$ (66 au) and extends out to $0\farcs98$ (100 AU) along the major axis (see Figure 4.4). Both the $Q_\phi$ and SN imagery exhibit little coherent signal between our inner working angle and the inner edge of the ring structure. We do not detect the inner disk component as previously detected by Monnier et al. (2017) due to our larger inner working angle. We therefore conclude that the small amount of scattered light interior to the ring in the PI image (panel

A; Figure 4.1) could arise from a mixture of residual, uncorrected flux from the PSF and scattered flux from an inner disk component that is within our masked region (see e.g. Takami et al. 2018). The NE-side of the disk is known to be the near side (Rosenfeld et al., 2013) and the IR scattered light disk exhibits evidence of strong forward scattering (Guidi et al., 2018). The broken ring structure we observe is missing polarized intensity originating from the far-side of the disk (SW region, along the minor axis; see Figure 4.1).

We fit an ellipse to the scattered light ring using a least squares fitting code written by Ben Hammel and Nick Sullivan-Molina [a], assuming the ring is a perfect circle projected at inclination. Since a known bias of the code is to prefer a smaller ellipse by preferably fitting the inner points (Halif et al. , 1998), we choose to fit the peaks of the ring to mitigate this effect. Due to the low signal along the SW minor axis and sporadic structure along the NE minor axis, we did not keep any vertical cuts between $70° < \text{PA} < 180°$ and between $270° < \text{PA} < 370°$. We fit a gaussian to each vertical crosscut, producing the peak x,y position of the ring, and input these positions into the ellipse code described above.

In order to estimate the error of our ellipse fit, we performed a Monte Carlo routine by randomly sampling the gaussian xy-coordinate errors and adding them to the xy-coordinates found above. We additionally applied a random rotation of the image between 0° and 1° to constrain the error associated with the interpolation of the image due to rotation. We performed 500 iterations and used the average values of the 500 iterations as the best fit ellipse. The errors were estimated by taking the standard deviation of the parameters found with the 500 iterations. The best fit results are shown in Table 4.1. The best fit ellipse is compared to the PI image in Figure 4.5 shown as the white oval along with the center of the disk (small white circle) and the center of the star.

[a] https://github.com/bdhammel/least-squares-ellipse-fitting

Our measured inclination of the disk (41.4 ± 0.3°) and PA (132.2° ± 0.3°) is in agreement with the values derived from ALMA data of 42 ° and 132° respectively (Isella et al., 2016). Additionally, the offset of the minor axis from the central star that we find (-0.″0432 ± 0.″0016) is consistent with previous measurements, given their quoted errors when available (0.″06, Garufi et al. 2014; 0.″105 ± 0.″045, Muro-Arena et al. 2018; 0.″1, Monnier et al. 2017).

We applied an $r^2$ illumination correction to our data to better investigate the physical distribution of dust in the ring seen in Figure 4.1. We then azimuthally binned the average flux per area of the ring between two concentric ellipses. We adopted an inclination of 42°, and constructed each bin to be 8° wide and spanned a projected radial distance of 0.″55 - 0.″71 (55 - 72.5 au), to encompass the majority of the disk flux. The binned disk flux is azimuthally symmetric along the major axis, with the NW- and SE-side of the disks exhibiting the same amount of polarized intensity (Figure 4.6). There is also a clear azimuthal asymmetry in the binned flux along the minor axis, with the near-side of the disk (NE-side) exhibiting substantially more flux than the far-side (SW-side). We observe a deficit in scattered light flux along the near-side of the disk at a PA of 30° in both the binned imagery (Figure 4.6) and unbinned PI, $Q_{rot}$ images, SN map images (Figure 4.1). This feature coincides with the position angle of the disk brightness enhancement and the position angle of the candidate point source noted by Guidi et al. (2018) and will be further discussed in Section 4.5.4.

### 4.3.2 Modeling of the HD 163296 Disk

To help interpret our imagery and contemporaneous IR spectroscopy of HD 163296, we utilized the 3D Monte Carlo Radiative Transfer code (MCRT), HOCHUNK3D (Whitney et al., 2013). HOCHUNK3D allows the user to characterize the radial

dust distribution, dust composition, and disk illumination parameters, and outputs a SED of the disk and imagery in a variety of user-defined bandpasses. The current version of HOCHUNK3D allows the user to decouple the disk into two dust distributions, allowing one to parameterize both a settled dust population towards the midplane and a different dust population in the upper surface layers of the disk. These two dust populations can either be co-spatial, or have different radial sizes. The dust distribution of each disk is characterized by several power-law parameters: the radial power law ($\alpha$), the vertical gaussian distribution ($\beta$), and the height of the disk from the mid-plane ($h$). Deviations from these power-laws such as a gap, spiral arms, warped disks, and walls can all be included. The code also allows for the presence of a dusty envelope, which is parameterized by its minimum and maximum radius ($R_{minenv}$, $R_{maxenv}$), and a dust density power-law (ENVEXP). The dusty envelope can also include gaps and a bipolar cavity. Following the techniques established by Sitko et al. (2008); Wagner et al. (2015); Fernandes et al. (2018), we use the dusty envelope as a proxy to model material ejected from the disk, aka a disk wind.

We constrained our model starting parameters by observations when possible, and adopted the parameters from Pikhartova et al. (in prep), who are using HOCHUNK3D to model the variations seen in two epochs of HD163296's SED, as a starting point for our parameter-space exploration. ALMA observations of HD 163296 revealed the presence of 3 gaps located at $0\farcs49$, $0\farcs82$, and $1\farcs31$ (50, 83, and 133 au respectively given GAIA-DR2 distance of 101.5 pc) (Isella et al., 2016). Since our HiCIAO imagery is only sensitive to the first dust ring and the near-IR SED is most sensitive to dust features closer to the star, we only include the inner gap in our model. We allowed the two components of the dust distribution to be vertically stratified, and chose the radial extent of these distributions to match those observed for grains populating the midplane (250 au from VLA and ALMA

observations; Guidi et al. 2016) and surface layers (540 au, Isella et al. 2007; Wisniewski et al. 2008). We note that while ALMA observations of the system were best described by a radial power-law multiplied by an exponential function (Isella et al., 2016), HOCHUNK3D only uses a power-law function. Nevertheless, we did adjust the large grain dust distribution to match, as closely as possible, the dust distribution as measured by ALMA in the inner portion of the disk (Isella et al., 2016). The dust parameters for the large grain disk that we used are adopted from Wood et al. (2002), and are composed of amorphous carbon and silicon dust particles ranging in size up to 1 millimeter. The small grain disk and envelope dust parameters are from Kim et al. (1994), which is the average galactic ISM dust grain model.

We adopted an interstellar extinction of $A_V = 0$ mag from Ellerbroek et al. (2014), who measured the level of extinction from the ejected HH-knots. Note that Ellerbroek et al. (2014) concluded that the optical variability of the SED likely comes from on source reddening. In our model, we utilize the dusty envelope, a proxy to model disk wind, to replicate the on source reddening which is further discussed in section 4.5.2. We explored accretion rates ranging from $1.73 \times 10^{-7}$ to $4.35 \times 10^{-6}$ $M_\odot$, calculated from contemporaneous Br$\gamma$ emission line in the SpeX 2011 data, first presented in Ellerbroek et al. (2014), but adjusted for the new distance of 101.5 pc.

We constrained these models using a SED (Figure 4.9) constructed from contemporaneous near-IR observations (Figure 4.2), along with non-contemporaneous photometry from the All WISE catalog (Wright et al., 2010), 2MASS All Sky Survey (Cutri et al., 2003), IRAS point source catalog (Helou & Walker, 1988), and the historical variability of the V-band photometry as compiled in Ellerbroek et al. (2014). We also constrained these models using the surface brightness profiles

along the major axis of our HiCIAO H-band scattered imagery (Figure 4.4).

We explored the parameter space of our models using a $\chi^2$ minimization scheme. Namely, we calculated the $\chi^2$ for the SED fit, the surface brightness along the major axis, and the minor axis offset, and added these values in quadrature to find the total $\chi^2$ value. Since some of the SED data were not contemporaneous, we also calculated a separate $\chi^2$ value that only incorporated comparisons of contemporaneously obtained data to the model. We began the iterative process with model runs of 5 million photons in order to find the best fit SED to the SpeX and Bass spectra. Next, we increased the number of photons in each run to 50 million photons to obtain higher quality model H-band images, and convolved the model image with the PSF of the H-band image. We explored parameter space to produce the best fit $\chi^2$ value between model surface brightness along the major axis and the minor axis offset to the observed imagery. After finding the best chi-squared fit model image, we iteratively switched between the SED and the model until we found a model that optimized the combined chi-squared value, resulting in our best fit model. We then re-ran this best fit model using $10^9$ photons to produce the model SED and imagery used all of our figures. We remind readers that MCRT models, like HOCHUNK3D that employ a large family of parameters, suffer from parameter degeneracy, thus our best fit model is not unique (Dong et al., 2012).

Table 4.2 lists the main parameters utilized in our best fit model, and Figure 4.7 details the temperature and density profile of the disk in this model. Figures 4.9 and 4.8 show the SED and radial surface brightness profile along the disk major axis of our best fit model as compared to our observations. We remark that our best fit model parameters are generally similar to those previously reported in the literature. For example, our disk mass of 0.05 $M_\odot$ (Table 4.2) is similar to that

measured by Qi et al. (2011) (0.089 $M_\odot$) and Isella et al. (2007) (0.12 $M_\odot$).

Our best fit model SED generally matches well with the contemporaneous spectroscopy and historical observations from optical to radio wavelengths (Figure 4.9). Since the optical flux has been shown to be highly variable and we do not have contemporaneous optical photometry or spectroscopy, we do not know whether the modest model overestimation of the optical flux simply reflects that the star was at a high flux state in 2011. Additionally, our model reproduces the on source extinction value of $A_V = 0.5$ mag from Ellerbroek et al. (2014) with a value of $A_V = 0.46$ mag. We note that the observed versus model imagery comparison matches well along the NW side of the disk (right hand side of Figure 4.8), while the model imagery is marginally too narrow along the SE side of the disk (left hand side of Figure 4.8). This could be due to slight geometrical variations in the wall of the disk, causing the illumination of the SE-side of the disk to be broader. We provide a full comparison of the observed H-band PI imagery and model imagery in Figure 4.10. Our model imagery reveals little scattered light beyond the bright ring and little to no scattered light within the gap of the disk, which matches the observed PI and $Q_\phi$ images.

## 4.4 Analysis of SCExAO/CHARIS High-Contrast Near-Infrared Spectroscopy

### 4.4.1 Methodology: Disk and Planet Forward-Modeling

Although none of the protoplanets/candidates reported from Keck/NIRC2 or ALMA are visible in our data, great care is needed to properly interpret these non-detections and their implications. For example, like HD 163296, HD 100546 has multiple imaged protoplanet candidates embedded in a bright, structured pro-

toplanetary disk (Quanz et al., 2013; Currie et al., 2015). Follow-up claims of a spurious detection/non-detection of candidates around HD 100546 were faulty as shown in Currie et al. (2017b), in large part due to 1) incorrect spectrophotometric calibration and 2) a lack of forward-modeling of planet and disk signals.

Contemporaneous near-IR spectra of HD 163296 allowed us to spectrophotometrically calibrate CHARIS data cubes (see Sect 2.1). To properly understand our non-detections and derive upper limits at the candidates' locations, we then performed forward-modeling of our images, investigating the reduction of the total source signal and the biasing of its spatial intensity distribution due to processing. This annealing results from self-subtraction of the source by itself and over-subtraction of the disk in ADI and SDI. Our method follows that outlined in Currie et al. (2018b), where we save the A-LOCI coefficients $\alpha$ and model the disk and planet signals as introducing a linear perturbation of value $\beta$, which provides an additional source of annealing (see also Brandt et al., 2013; Pueyo, 2016). We focus on the May 2018 data due to its higher quality.

First, we explored the effect of disk on the non-detections of planetary companions, using forward-modeling to determine its annealing due to processing and its effect on any point sources located exterior, like the proposed companions from Guidi et al. (2018) and Teague et al. (2018). We started with the best-fit scattered light disk model described in Section 4.3.2, which is drawn from our H-band scattered light imagery with Subaru/HiCIAO. We produced a total intensity (not scattered light) images in $J$, $H$, and $K$ passbands and interpolated the model images onto the CHARIS wavelength array and pixel scale. The model disk is slightly bluer than the combined light of the star+disk, with intrinsic colors of $J$-$H$, $H$-$K$ of $\sim 0.35$ and $\sim 0.35$. Note that the model was constructed based on a single passband (H-band), thus the model may not constrain the true color

of the disk. The disk contrast with respect to the star on the forward-scattering side is typically $\Delta$M = $M_{disk/arcsec^2}$ - $M_\star \approx$ 3.5–4. The visible trace of a disk may differ in total intensity vs. scattered light. Therefore, we slightly adjusted the model parameters to provide a better match to the forward-modeled disk image, specifically increasing the semimajor axis by 5%.

Second, we verified that an object consistent with the 6–7 $M_{\rm J}$ candidate from Guidi et al. would be detected in our data. We used standard hot-start evolutionary models from Baraffe et al. (2003), adopting a planet age equal to the system age (5 Myr). This approach is intermediate between possible extremes that would yield higher and lower luminosities for a given planet mass. While we assume a planet age of 5 $Myr$ when estimating mass limits, the age of a superjovian planet is likely much younger than that of the host star (Currie et al., 2013). This is especially true for *protoplanets*, which are nearing the end of their formation and thus much closer to $t \lesssim 1$ $Myr$ for any evolutionary model, where the planet luminosity is maximum. The inferred limits adopting would be then substantially lower than those we report. Conversely, we could adopt planet mass limits using the "cold start" evolutionary models (e.g. Marley et al., 2007). However, recent literature casts serious doubt on the validity of the cold start model formalism, which relies on specific assumptions about the entropy of accreted material. As shown by Berardo et al. (2017), classic cold start conditions are extremely difficult to reach as the protoplanet will be substantially heated by the accretion shock, which will increase its entropy, resulting in hot start-like initial condition. Furthermore, imaged planets for which we have derived dynamical masses – $\beta$ Pic b, HR 8799 bcde (Lagrange et al., 2010; Marois et al., 2010; Currie et al., 2011; Snellen and Brown, 2018; Wang et al., 2018; Dupuy et al., 2019) – are inconsistent with a cold-start evolutionary model. At the candidate's location in each data cube, we injected a planet whose temperature matches that expected for a 4 $M_{\rm J}$,

5 $Myr$ planet according to these models. Although such a planet is predicted to be near the L/T dwarf transition ($T_{\rm eff} \sim 1300\ K$), we assume a (cloudier) L dwarf spectrum drawn from the Bonnefoy et al. (2014) library, since annealing due to SDI will be stronger for such a spectrum. Integrated over the CHARIS wavelength array, the broadband contrast of this planet with respect to HD 163296 is $\sim 8{\times}10^{-6}$, about 2.5–3.5 times as high as the predicted contrast for the Guidi et al. companion using a cloudy planet atmosphere from Currie et al. (2011).

Finally, our forward-modeling calculation allowed us to compute radially-averaged, throughput-corrected broadband contrast curves. As with our fake planet injection test, we used the Baraffe et al. (2003) models to map between planet mass and temperature. To map between temperature and spectrum, we further used atmosphere models drawn from A. Burrows, adopting cloud prescriptions that provide reasonable fits to near-IR photometry for HR 8799 bcde and ROXs 42Bb, whose temperature, gravity, and masses cover most of our range (Currie et al., 2011; Madhusudhan et al., 2011; Currie et al., 2014a, Currie et al. 2018 in prep.).

### 4.4.2 Results: Limits on Planets

Figure 4.11 shows the wavelength-collapsed image of the input disk (left panel) and output image after forward-modeling the disk through ADI and SDI (right panel). While the disk in total intensity is more forward-scattering than the model based on polarimetry would predict and its brightness is $\sim 30\%$ higher, the model otherwise reproduces the CHARIS data and is sufficient for investigating the impact of self-subtraction on the forward-scattering side. The proposed candidate from Guidi et al. (2018) lies exterior to the main trace of the disk (cyan cross). After processing, the candidate's location is free of negative self-subtraction foot-

prints. Inspection of the individual data cubes containing the disk model processed through ADI & SDI likewise show a flat background. At wider separations overlapping with the proposed candidate from Teague et al. (2018), the disk likewise leaves negligible residual effects.

As shown in Figure 4.12 (left panel), a 6–7 $M_{\rm J}$ candidate similar to the one proposed in Guidi et al. should have been detected in our data. The fainter, even lower-mass (4 $M_{\rm J}$) candidate injected into our data is clearly visible. While its SNR is formally $\sim$ 4.8, our inclusion of disk signal contributions leads our estimate of the noise to be conservative. A planet corresponding to the Guidi et al. candidate ($\Delta$F $\sim$ 2.5 $\times 10^{-5}$ would be even more decisively detected (SNR $\sim$ 15).

Broadband contrast limits in the righthand panel of Figure 4.12 provide stringent limits on protoplanets covering the range probed with Keck/NIRC2 and ALMA. At $\rho \sim 0\farcs49$, the azimuthally-averaged 5-$\sigma$ contrast limit is $\sim 8.5\times10^{-6}$, in agreement with our expectations from the fake planet injection. If the Guidi et al. companion is real, it would then have to be redder than $H$ - $L_{\rm p} \sim 3.5$ to escape detection: redder than all directly-imaged planets except for the extreme L/T transition object HD 95086 b (DeRosa et al., 2016). Over the separations just interior or close to the visible trace of the disk and comparable to the separation of the Guidi et al. companion – $\rho \sim 0\farcs4$ ($0\farcs7$) along the minor (major) axis – we can exclude planets with masses of 2–5 $M_{\rm J}$, assuming standard hot-start evolutionary models. The CHARIS field encloses the possible location of the innermost companion proposed by Teague et al. (2018), which would lie at a projected separation of $r_{\rm proj} \sim 83$ au ($\rho \sim 0\farcs82$) along the major axis or $r_{\rm proj} \sim 40$ au ($\rho \sim 0\farcs4$) along the minor axis. At these locations, our data rule out planets more massive than 5 $M_{\rm J}$ and $\sim$ 1.5 $M_{\rm J}$, respectively. If located along the minor axis, the outermost proposed companion from Teague et al. (2018) would be at $\rho$

$\sim 0\farcs65$ with a mass less than $\sim 2\ M_{\rm J}$ according to our data.

## 4.5 Discussion

### 4.5.1 Previous optical-IR disk imaging

HD 163296 has been observed numerous times across optical-IR bandpasses. Here we briefly summarize some of the major results of those investigations, to compare and contrast with our new imagery.

Space-based optical imagery has been obtained in both white light (HST/STIS; Grady et al. 2000) and broad-band filters (HST/ACS; Wisniewski et al. 2008), tracing the disk out to $4\farcs4$ (447 AU) and detecting HH knots. Comparison of these data revealed evidence for significant variation ($\sim$1 magnitude) in the disk surface brightness, changes in the number of disk ansae visible over time, and changes in the relative brightness of features located in the NW and SE disk regions (Wisniewski et al., 2008). Unfortunately, none of these optical observations fully overlapped in wavelength coverage.

Ground-based AO imagery of the system can be generally summarized into 3 categories. First, a subset of observations clearly reveal the detection of the disk in scattered light, but the presence of residual AO speckle noise in the disk vicinity prevents a robust characterization of the surface brightness or detailed morphological structure of the disks (e.g. 2012 H-band imagery Garufi et al. 2014; 2014 Ks-band imagery Garufi et al. 2017). Second, a subset of observations (e.g. 2012 Ks-band imagery; Garufi et al. 2014) reveal the detection of an inclined ring structure extending out to $1\farcs03$ (103 AU), where the intensity of scattered light is strongest along the major axis of the disk and is symmetrical about both sides of the disk major axis (NW-side and SE-side). Third, a subset of observations

(e.g. 2014 J-band Monnier et al. 2017; 2016 H-band imagery Muro-Arena et al. 2018) reveal clear evidence of this same inclined ring structure whose flux is both azimuthally asymmetric and not the strongest along the major axis. In particular, the NW side of the major axis is brighter than the SE side of the disk in J-band GPI observations (see Figure 2, Monnier et al. 2017), and the maximum flux from the disk is north of the major axis peaking on the NW side of the disk in these data. The 2016 H-band VLT/SPHERE observations (Muro-Arena et al., 2018) also exhibit strong azimuthal asymmetry, with the NW-side of the disk along the major axis exhibiting 2.7x more scattered light than the SE-side of the disk along the major axis. Muro-Arena et al. (2018) used 3D radiative transfer modeling to suggest that this strong azimuthal asymmetry could be reproduced by including an inner disk component that was misaligned by 1° compared to the outer disk.

### 4.5.2 Evidence for time dependent azimuthal asymmetry

Our 2011-epoch H-band imagery is consistent with the second category of disk appearance we discussed in Section 4.5.1. Namely, we observe a broken ring structure in H-band scattered light whose flux peaks along the major axis and exhibits clear symmetry between the NW- and SE-side of the disk. Our 2011 epoch H-band data are thus clearly different than the 2016 epoch VLT/SPHERE H-band data, that show a 2.7x asymmetry between the NW- and SE-side of the disk (Muro-Arena et al., 2018).

To illustrate these differences, we scaled the peak flux along the major axis of the 2016 VLT/SPHERE data and present these data as dashed horizontal lines in our Figure 4.4. The 2.7x asymmetry about the major axis observed in the 2016 VLT/SPHERE data is clearly outside of the $3\sigma$ errors of our 2011 data. This obvious difference is also seen by comparing Figure 1 of Muro-Arena et

al. (2018) with Figure 4.1 in this paper. We note that neither dataset exhibits evidence of large-scale gradients in their $U_\phi$ component, indicating that systematic artifacts are not the cause of this phenomenon. We suggest that this is clear evidence that the system exhibits large changes in the appearance of its scattered light disk as seen in multi-epoch observations obtained with the same filter, and supports previous suggestions of this phenomenon as deduced from multi-epoch observations from similar, albeit not the same, filters (Wisniewski et al., 2008).

There are several mechanisms that could cause an azimuthal asymmetry of scattered light including an asymmetrical distribution of dust (Muro-Arena et al., 2018), an inclined inner disk shadowing the outer disk (Muro-Arena et al., 2018), a warped inner disk structure shadowing the outer disk (Sitko et al., 2008), or dust ejected above the mid-plane of the disk that shadows the outer disk (Ellerbroek et al., 2014).

Muro-Arena et al. (2018) suggested that an asymmetric distribution of dust in the system was unlikely, as no asymmetry was observed with ALMA (Isella et al., 2016). Muro-Arena et al. (2018) was able to replicate the azimuthal asymmetry they observed in their scattered light imagery by inclining the inner disk by 1° compared to the outer disk , which is consistent with previous near-IR interferometric observations (Tannirkulam et al., 2008; Lazareff et al., 2017; Setterholm et al., 2018). However, our 2011 epoch data reveal the presence of no azimuthal asymmetry along the major axis in the same filter bandpass as the 2016 SPHERE observations. An inclined inner disk is unlikely to precess significantly over a 5 year time-frame; hence, an inclined inner disk alone is unlikely to produce the observed significant azimuthal variations in the scattered light disk. Moreover, we have shown that we can reproduce the basic properties of both our contemporaneously obtained near-IR SED and H-band imagery with a model that does

not include an inner inclined disk. Thus, while the system could plausibly host an inclined disk, we suggest that this feature is unlikely to be responsible for producing the time-dependent azimuthal variations in the outer scattered light disk of the system.

We consider several other mechanisms that could explain the change in disk surface brightness seen in the system. First, a warped inner disk structure, such as a puffed up inner disk wall (Turner et al., 2014), could be shadowing the outer disk Sitko et al. (2008). If this disk warp were to dissipate or rotate azimuthally within a 2-3 year timescale, this could cause a change in illumination of the outer disk similar to that observed between the 2011 and 2016 epoch H-band datasets. Dynamical simulations are needed to determine whether a substantial change in the appearance of a warped disk could occur on this short of a time-scale and lead to the amplitude of variable disk illumination observed.

Second, this phenomenon could be caused by dust ejected above the mid-plane of the disk, which partially shadows the outer disk, as proposed by Ellerbroek et al. (2014). These dust "clouds" could differentially obstruct the illumination of the outer disk while they are between the star and the outer disk, as shown in Figure 4.13. We do have IR spectra that were obtained at a similar epoch to both our 2011 HICIAO data and the 2016 SPHERE data. The contemporaneous IR spectra cannot constrain the possible asymmetric nature of the dust clouds, but can constrain the total amount of dust in the disk wind when compared to our MCRT models. As shown in Figure 4.2, while both have the same flux around 0.9 $\mu$m, the 2011 epoch IR spectrum is brighter ($\sim$0.5 mag at K') around 2 $\mu$m than the 2016 epoch IR spectrum. We remark that we can best reproduce the 2016 SED in our model by adopting a $\sim$2x lower envelope density, e.g. $9.0 \times 10^{-18} \frac{g}{cm^3}$, which corresponds to a lower circumstellar extinction in 2016 of $A_V = 0.1$ mag. We predict that the 2016 epoch should be 0.4 mag brighter in the V-band compared

to the 2011 epoch data, similar to the optical variability found by Ellerbroek et al. (2014). Since the interstellar extinction is consistent with AV = 0 mag, the observed reddening most likely originates from the system. Thus an asymmetric disk wind launching dust clouds can explain both the variable illumination of the outer disk (Figure 4.13) and the reddening optical variability observed by our disk wind models and Ellerbroek et al. (2014).

If the system does have an inclined inner disk as suggested by Muro-Arena et al. (2018) that during some epochs produces non-axisymmetric illumination of the outer disk (e.g. NW-side brighter than SE-side; 1998 HST/STIS Grady et al. 2000, 2014 J-band Monnier et al. 2017; 2016 H-bandMuro-Arena et al. 2018), the spatial distribution of any dust clouds elevated by a disk wind must also be non-axisymmetric to produce the observed epochs of axi-symmetric illumination of the outer disk (e.g. as seen in 2012 Ks-band imagery, Garufi et al. 2014; 2011 H-band, this study) and the sole-epoch of observed non-axisymmetric illumination with the SE-side of the disk brighter than the NW-side (2004 HST/ACS Wisniewski et al. 2008). Future observations that simultaneously observe quiescent and wind events with contemporaneous optical and IR photometry and coronagraphic imagery could help to test whether shadowing by dust clouds could explain the observed behavior of the inner and outer disk of the system, and better parameterize the azimuthal distribution of such dust clouds.

### 4.5.3 Model

We were able to reproduce the basic properties of our contemporaneous near-IR spectra and scattered light H-band imaging with a 3D MCRT disk model, which approximated the features of a disk wind via an envelope. As seen in Figure 4.9, our model SED is consistent with the highest observed V-band flux that was

reported by Ellerbroek et al. (2014), but we caution that the robustness of this agreement is uncertain as we do not have contemporaneous optical photometry.

Muro-Arena et al. (2018) also performed MCRT modeling of HD 163296, and compared their models to the ALMA dust continuum image from Isella et al. (2016), their own VLT/SPHERE image, and historical photometry and spectroscopy. They modeled all three gaps that were observed in the ALMA continuum image and introduced an inclined disk to explain the asymmetric scattered light flux observed with the VLT/SPHERE image as noted above 4.5.2. Their model images and SED are well matched to their observed images and historical photometry and spectroscopy. While they do not employ a disk wind model as we did (Section 4.3.2, see Figure 4.13), their model does not have a clear mechanism to explain the time dependent azimuthal asymmetries seen in near-IR scattered light images (Section 4.5.2) or the optical-IR photometric and spectroscopic variability that has been observed (Sitko et al., 2008; Ellerbroek et al., 2014). We caution that the inability of an inclined disk by itself to explain the observed time dependent azimuthal asymmetries observed in scattered light does not exclude the possibility that the system does in fact have an inclined disk. Due to limitations with Hochunk3D, we leave applying our disk wind model to the archival images and SEDs to future work.

### 4.5.4 Scattered light features along the minor axis

We note that a deficit of scattered light is seen in the near-side of our disk imagery at a PA of 30°, in both our binned imagery (Figure 4.6) and our unbinned PI and $Q_{rot}$ images. We caution that while this feature could be real, it is not uncommon to observe depolarization along the minor axis due to the residual presence of an un-corrected polarized halo. Interestingly, this feature coincides with the disk

brightness increase observed with the Keck/NIRC2 L'-band vortex coronagraph by Guidi et al. (2018) and is located at a similar position angle, albeit closer to the host star, as the purported candidate planetary mass object reported by Guidi et al. (2018). As noted by Guidi et al. (2018), this disk feature is located where forward scattering should be significant. If the feature we observe at the similar disk position is astrophysical, the decreased amplitude of the feature in polarized intensity suggests that it could be polarized less than its neighboring disk material.

### 4.5.5 Limits on Protoplanets Orbiting HD 163296

Our data improve the detection limits for protoplanets in thermal emission around HD 163296 compared to Keck/NIRC2 data from Guidi et al. (2018): from 5–7 $M_{\rm J}$ to now 2–5 $M_{\rm J}$, assuming standard hot-start evolutionary models, near the projected trace of the disk. At wider separations covering the possible locations of the inner proposed candidate from Teague et al. (2018) ($r_{\rm proj} \sim 83$ au/$\rho \sim 0\farcs82$), the limits have now improved from 4.5 $M_{\rm J}$ to 1.5 $M_{\rm J}$, the latter which is just slightly higher than the predicted mass of the companion (1 $M_{\rm J}$). Limits for the outer Teague et al. candidate along the minor axis are likewise just slightly higher than the predicted mass (a limit of 2 $M_{\rm J}$ vs. a predicted 1.3 $M_{\rm J}$). Thus, at least for now, the ALMA-predicted protoplanet candidates are consistent with direct imaging constraints.

Our data appear to rule out the proposed, marginally-significant candidate identified from thermal IR data in Guidi et al. (2018). Using standard assumptions for planet atmospheres, our forward-modeling demonstrates we could have detected an even fainter planet at the location of the proposed candidate. For an assumed age of 5 $Myr$ and hot-start evolutionary models, the candidate is pre-

dicted to be 6–7 $M_J$, while our radially-averaged contrast limits are significantly lower ($\sim$ 4–5 $M_J$)[a].

The simplest explanation for our conflicting results is that the NIRC2 candidate is instead residual, partially-subtracted speckle noise or partially-subtracted disk emission left over from processing. Figure 1 of Guidi et al. (2018) shows multiple emission peaks with a similar or slightly smaller spatial scale as the candidate (e.g. at the 2, 6, 7, and 8 o'clock positions just exterior to the masked region). An even brighter, seemingly point source-like peak at nearly the same position angle in these data appears to be an artificially-enhanced region of the disk, which could have been mistaken for a point in shallower and/or higher background data. Convolving the image with a gaussian kernel may further accentuate the point source-like appearance of these features[b]. The position of the candidate also coincides with the minor axis of a second ring of emission detected with ALMA. Forward-modeling as performed in Currie et al. (2015) could better clarify whether the candidate's morphology is consistent with an annealed point source or residual disk emission.

Alternatively, the candidate could be extremely red/underluminous in the near-IR and thus difficult to detect. If embedded in the disk, it would be preferentially extincted in the near-IR compared to the thermal infrared, as has been

[a]Note that any new age estimates for HD 163296 drawn from its GAIA-revised distance do not change our results. Comparisons to some isochrones may imply an older age (e.g. $7.6 \pm 1.1$ $Myr$; Vioque et al. 2018). However, others (e.g. the MIST and PARSEC) isochrones imply ages comparable to or just slightly greater than 5 Myr (T. Currie, unpublished). These differences do not change the fact that the proposed HD 163296 companion should have been detected in our data under standard assumptions for planet atmospheres.

[b]The large spatial scale of the residuals may also be traced to the PSF subtraction method used, which leverages on the Karhunen-Loéve Image Projection (KLIP) algorithm with few KL modes retained (Soummer et al., 2012). Compared to standard implementations of A-LOCI, KLIP with few KL modes retained may yield larger spatial scale residuals (T. Currie, unpublished). This is especially true for KLIP implementations performing PSF subtraction in full annuli as in Guidi et al. instead of smaller wedge-shaped annular regions, since the subtraction is less local, in addition to constructing a low-rank approximation of the data set's covariance matrix.

proposed for HD 100546 b (Currie et al., 2015; Quanz et al., 2015). It could also retain an extremely dusty/cloudy atmosphere characteristic of some young exoplanets near the L/T transition (Currie et al., 2011; DeRosa et al., 2016), making it appear "underluminous" in the near-infrared. Follow-up thermal infrared imaging at $L_{\rm p}$ or $M_{\rm p}$ could provide a more decisive probe of these possibilities.

## 4.6 Conclusions

We report H-band polarimetric imagery of the HD 163296 system along with contemporaneous infrared spectra observations and near-IR extreme AO imaging in total intensity. We find:

- Our 2011 H-band polarimetric imagery resolve a broken ring structure surrounding HD 163296 that peaks at a distance along the major axis of 0.″65 (66 au) and extends out to 0.″98 (100 AU) along the major axis. Our non-detection of the inner disk component is driven by our inner working angle (0.″3, 30.5 au), and does not conflict with the detection of this component by Monnier et al. (2017).

- Our 2011-epoch H-band imagery exhibits clear axisymmetry, with the NW- and SE-side of the disk exhibiting similar intensities. Our 2011 epoch H-band data are thus clearly different than the 2016 epoch H-band data from VLT/SPHERE reported by Muro-Arena et al. (2018), that exhibit a strong 2.7x asymmetry between the NW- and SE-side of the disk. These results indicate the presence of time variable, non-azimuthally symmetric illumination of the outer disk.

- We were able to reproduce the basic properties of our contemporaneous near-IR spectra and spatially resolved H-band polarimetric imagery of the

HD 163296 disk with a 3D MCRT disk model that approximated the features of a disk wind via an envelope and did not specifically require an inclined inner disk component. We suggest that, while the system could plausibly host an inclined disk as suggested by Muro-Arena et al. (2018), such a component is unlikely to be responsible for producing the observed time-dependent azimuthal variations in the outer scattered light disk of the system. We speculate that a variable, non-axisymmetric distribution of dust clouds elevated by a disk wind could produce the diversity of morphological appearances of the outer disk now reported in the literature for this system.

- While our 2018 epoch SCExAO/CHARIS observations easily recovers the disk, they fail to recover the candidate 6–7 $M_{\rm J}$ protoplanet identified from Keck/NIRC2 data (Guidi et al., 2018). The Keck/NIRC2 detection is likely a residual speckle or a partially-subtracted piece of the disk; alternatively, this object could be a heavily embedded or particularly red/cloudy object only identifiable in the thermal infrared.

- Assuming hot-start evolutionary models and a system age of 5 Myr, our SCExAO/CHARIS detection limits for protoplanets in thermal emission around HD 163296 near the projected trace of the disk are 2–5 $M_{\rm J}$. At wider separations, covering the possible locations of the inner proposed candidate from Teague et al. (2018) ($r_{\rm proj} \sim 83$ au/$\rho \sim 0\farcs82$), our data lower the mass limit for detections from 4.5 $M_{\rm J}$ to 1.5 $M_{\rm J}$, which is still slightly higher than the predicted mass of the companion (1 $M_{\rm J}$). Limits for the outer Teague et al. candidate along the minor axis are likewise just slightly higher than the predicted mass (a limit of 2 $M_{\rm J}$ vs. a predicted 1.3 $M_{\rm J}$). The ALMA-predicted protoplanet candidates are currently still consistent with direct imaging constraints.

## 4.7 Acknowledgements

This chapter is reproduced by permission of the American Astronomical Society from the following publication: Rich, E. A., Wisniewski, J. P., Currie, T., et al. 2019, ApJ, Accepted, "The Time Variable Scattered Light Morphology of the HD 163296 Protoplanetary Disk". Here is the original publications author list: Evan A. Rich, John P. Wisniewski, Thayne Currie, Misato Fukagawa, Carol A. Grady, Michael L. Sitko, Monika Pikhartova, Jun Hashimoto, Lyu Abe, Wolfgang Brandner, Timothy D. Brandt, Joseph C. Carson, Jeffrey Chilcote, Ruobing Dong, Markus Feldt, Miwa Goto, Tyler Groff, Olivier Guyon, Yutaka Hayano, Masahiko Hayashi, Saeko S. Hayashi, Thomas Henning, Klaus W. Hodapp, Miki Ishii, Masanori Iye, Markus Janson, Nemanja Jovanovic, Ryo Kandori, Jeremy Kasdin, Gillian R. Knapp, Tomoyuki Kudo, Nobuhiko Kusakabe, Masayuki Kuzuhara, Jungmi Kwon, Julien Lozi, Frantz Martinache, Taro Matsuo, Satoshi Mayama, Michael W. McElwain, Shoken Miyama, Jun-Ichi Morino6, Amaya Moro-Martin, Takao Nakagawa, Tetsuo Nishimura, Tae-Soo Pyo, Eugene Serabyn, Hiroshi Suto, Ray W. Russel , Ryuji Suzuki, Michihiro Takami, Naruhisa Takato, Hiroshi Terada, Christian Thalmann, Edwin L. Turner, Taichi Uyama, Kevin R. Wagner, Makoto Watanabe, Toru Yamada, Hideki Takami, Tomonori Usuda, Motohide Tamura

We acknowledge support from the NASA XRP program via NNX-17AF88G. The authors recognize and acknowledge the significant cultural role and reverence that the summit of Mauna Kea has always had within the indigenous Hawaiian community. We are most fortunate to have the opportunity to conduct observations from this mountain.

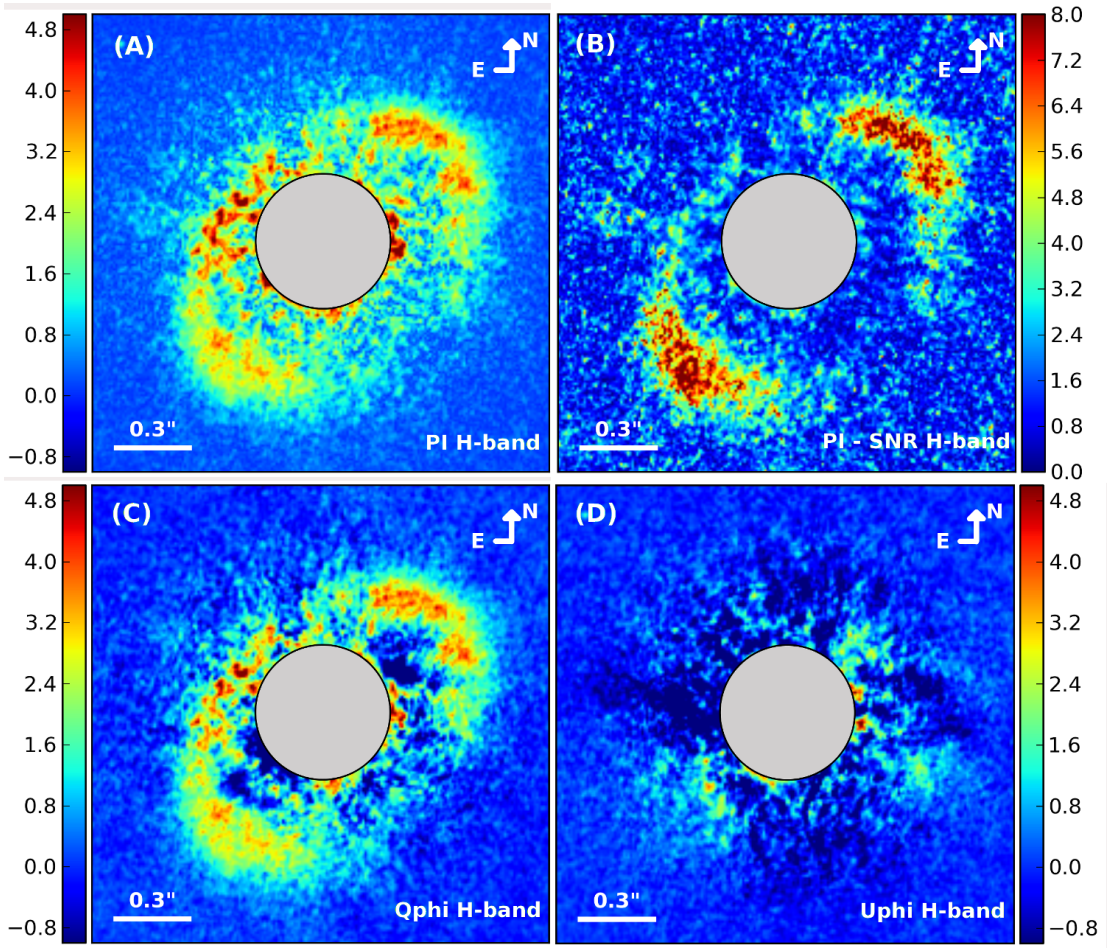


Fig. 4.1.— H-band scattered light from the HD 163296 disk is clearly seen in polarized intensity (PI) (panel A), the SN map (panel B), and in $Q_{phi}$ imagery (panel C). Little coherent signal is seen in the $U_{phi}$ image (panel D), indicating that these data are largely free from PSF residuals. The PI (panel A), $Q_{phi}$ (panel C), and $U_{phi}$ (panel D) images are displayed on a linear scale with units of mJy, and have not been filtered. We have applied a software mask having a radial size of 0.″3 (gray circles) to match the effective inner working angle of these data. For all panels, North is up and East is to the left. The Q and U images shown in panels C and D of this figure is available as the Data behind the Figure.

| Parameter | PI image Value |
|---|---|
| Major Axis of Disk (AU) | 58.01 ± 0.09 |
| Minor Axis of Disk (AU) | 48.4 ± 0.3 |
| Minor Axis offset (") | -0.0432 ± 0.0016 |
| PA (deg) | 132.2 ± 0.3 |
| Inclination (°) | 41.4 ± 0.3 |

Table 4.1: Results of ellipse fitting to PI H-band image

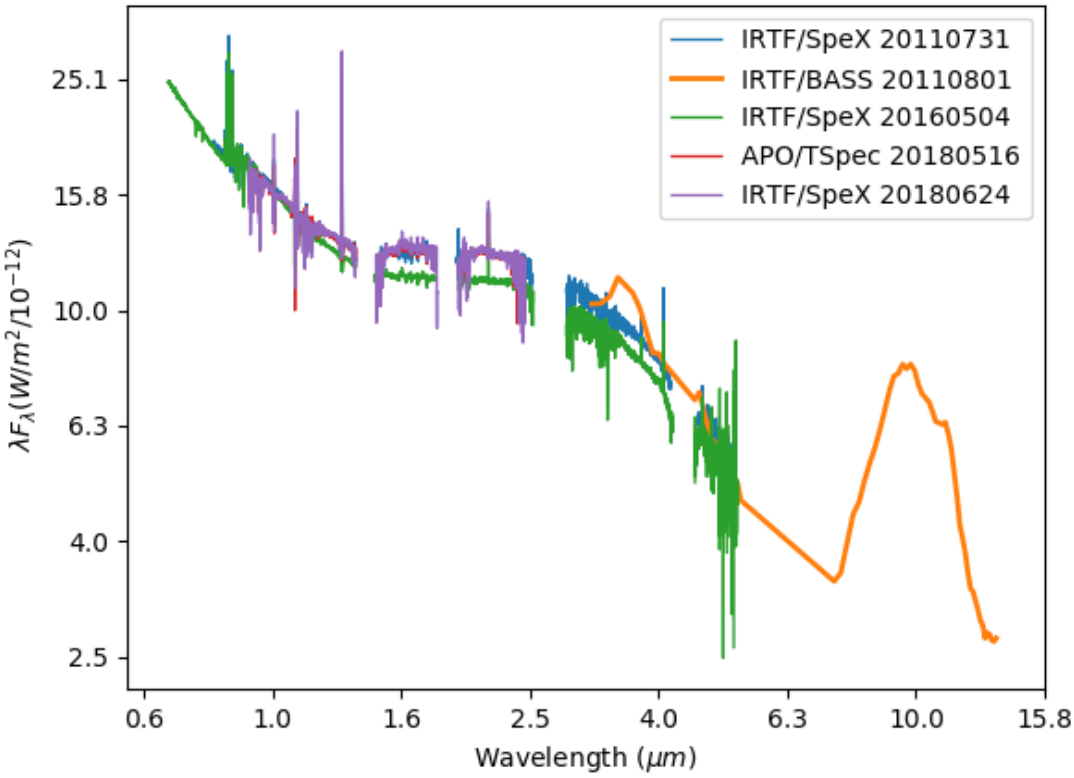


Fig. 4.2.— 5 epochs of flux calibrated IR spectra of HD 163296, taken with IRTF/SpeX, IRTF/BASS, or APO/TripeSpec, are shown. A full description of these observations can be found in Section 4.2.2. The spectra are plotted in log-log space.

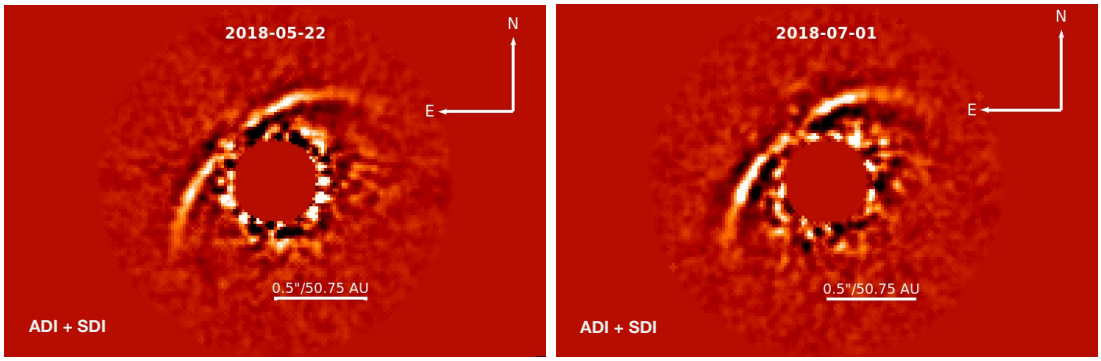


Fig. 4.3.— SCExAO/CHARIS broadband (wavelength-collapsed) images from 2018 May (left) and 2018 July (right) after removing the stellar PSF through both ADI and SDI: the color scaling for both panels goes from -30 to 30 mJy arcsec$^{-2}$. In both data sets, self-subtraction footprints (dark regions) flank the disk signal, which is reduced due to processing. The throughput of the disk is slightly higher in the July data due to better field rotation; regions surrounding the disk show slightly less residual speckle noise in the May data due to better AO performance.

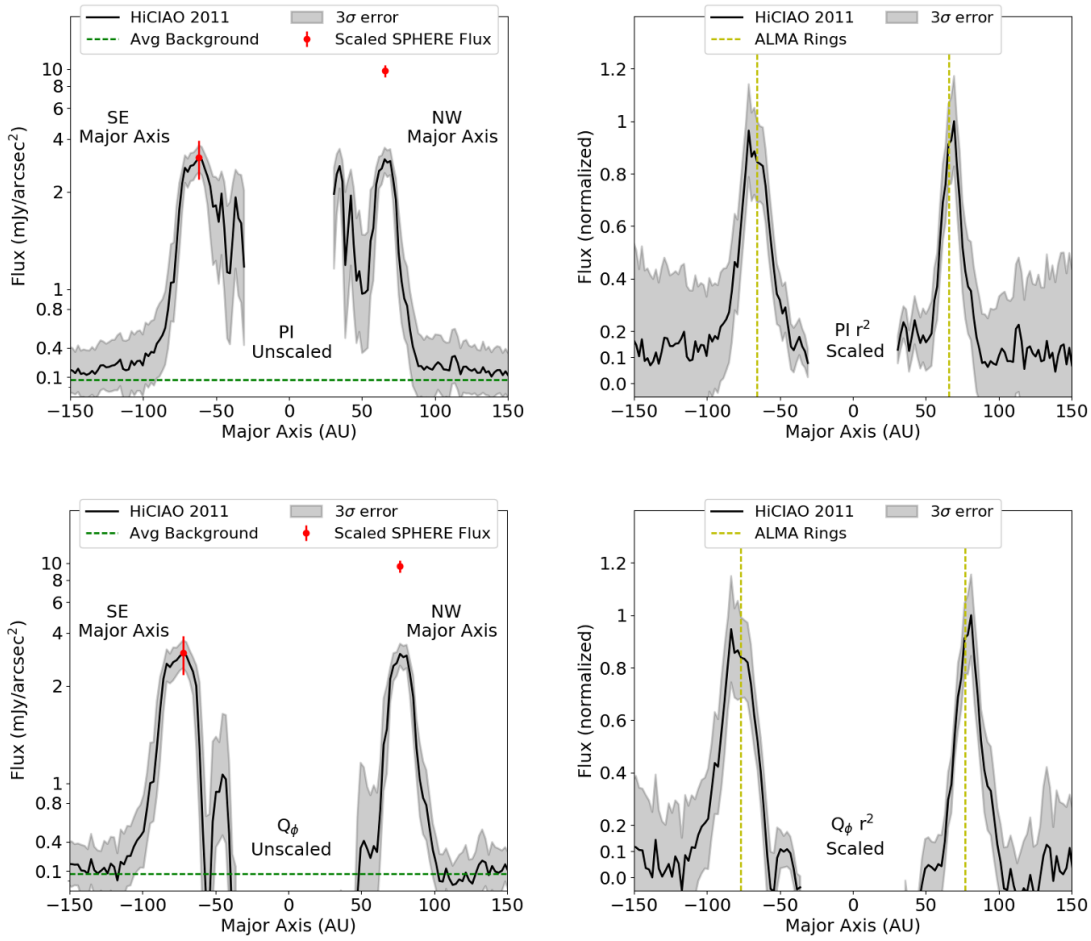


Fig. 4.4.— Crosscuts along the major axis of the 2011 H-band PI image (top row) and $Q_\phi$ image (bottom row). The right column is the PI and $Q_{phi}$ images unscaled, and the left column is the PI and $Q_\phi$ with a $r^2$ scaling applied. The gray shaded area represents 3-$\sigma$ error bars. The red point is the scaled flux from the 2016 VLT/SPHERE observation reported by Muro-Arena et al. (2018).

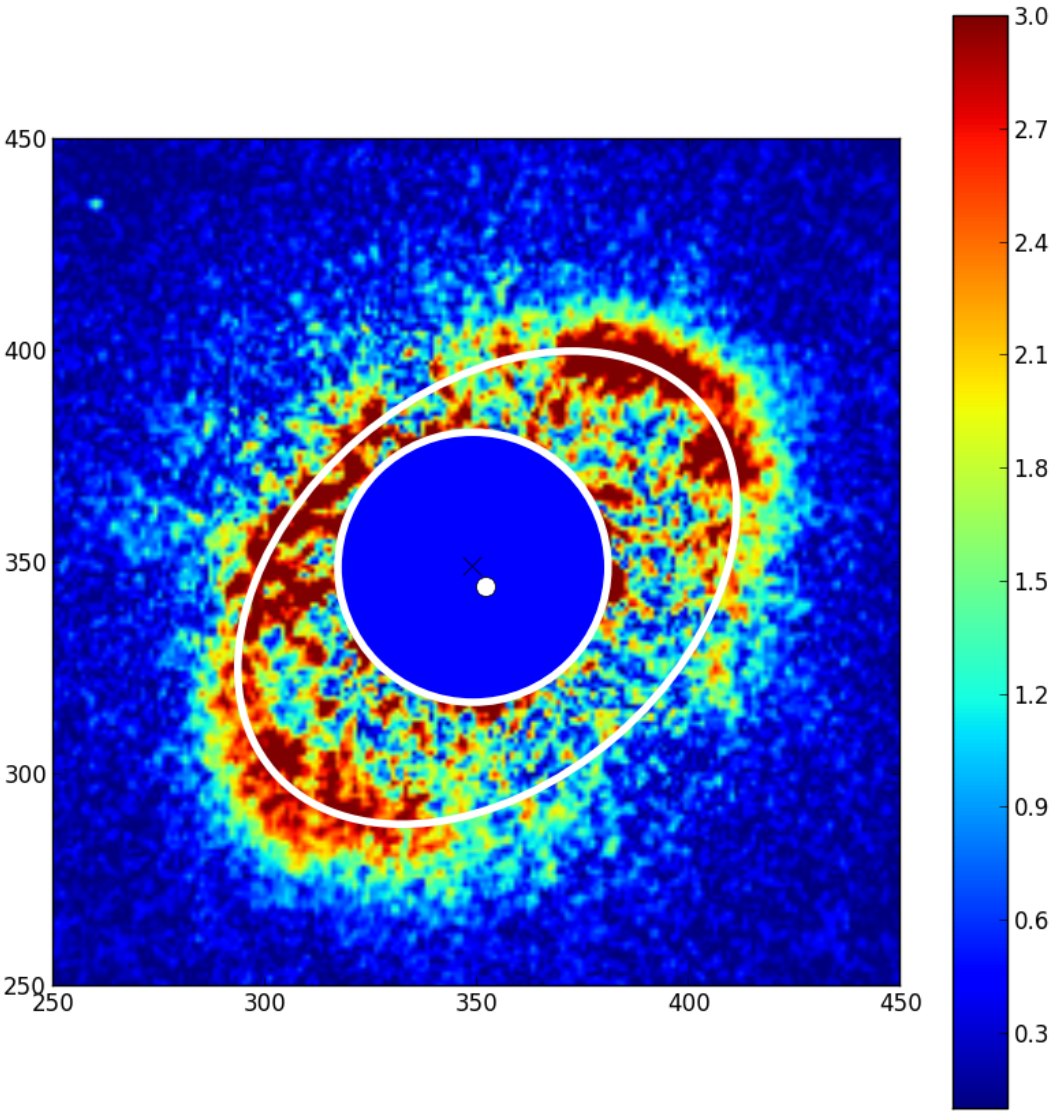


Fig. 4.5.— Result of the best fit ellipse to our H-band PI data, where the central white dot is the center of the ellipse, the white ellipse is the peak of the ellipse, the black x marks the location of the star, and the blue circle marks the inner working angle. The ellipse was fit to the peak points along the main elliptical ring by fitting gaussians to the cross cuts along the ring. The best elliptical fit finds a minor axis offset of -0.″055. This value is consistent with those reported by Garufi et al. (2014); Monnier et al. (2017); Muro-Arena et al. (2018) given their quoted uncertainties.

| Parameter (Units) | Best fit Model | Lower Bound | Upper Bound |
|---|---|---|---|
| Star Temperature (K) | 9250 | ... | ... |
| Star Radius ($R_\odot$) | 1.4 | 1.2 | 1.6 |
| Disk Mass ($M_\odot$)$^{(a)}$ | 0.05 | ... | ... |
| Fraction of Mass in Large Grain Disk | 0.9 | 0.8 | 0.95 |
| Inner Gap Radius (AU) | 29 | 20 | 32 |
| Outer Gap Radius (AU) | 59 | 55 | 62 |
| Large Grain Disk Minimum Radius ($R_{sub}$)$^{(b)}$ | 31.9 | 25 | 35 |
| Large Grain Disk Maximum Radius (AU) | 250.1 | ... | ... |
| Large Grain Disk Scale Height ($R_{sub}$)$^{(b)}$ | 0.11 | 0.08 | 0.13 |
| Large Grain Disk radial density exponent | 0.1 | 0.05 | 0.2 |
| Large Grain Disk scale height exponent | 0.16 | | 0.18 |
| Small Grain Disk Minimum Radius ($R_{sub}$)$^{(b)}$ | 1.22 | 1.0 | 1.5 |
| Small Grain Disk Maximum Radius (AU) | 540.1 | ... | ... |
| Small Grain Disk Scale Height ($R_{sub}$)$^{(b)}$ | 0.11 | 0.08 | 0.13 |
| Small Grain Disk radial density exponent | 0.05 | | |
| Small Grain Disk scale height exponent | 1.25 | | |
| Envelope inner radius ($R_sub$)$^{(b)}$ | 0.41 | ... | ... |
| Envelope outer radius (AU) | 2.38 | ... | ... |
| Envelope Density ($\frac{g}{cm^3}$) | $4.0 \times 10^{-17}$ | $2.0 \times 10^{-17}$ | $6.0 \times 10^{-17}$ |
| Accretion ($M_\odot$) | $6.0 \times 10^{-7}$ | | |

Table 4.2:: List of key best fit model parameters and estimates of the upper and lower bounds the parameter.
(a) Disk mass value includes dust and gas. We assumed the gas to dust ratio is 100.
(b) $R_{sub}$ is the sublimation radius with 1 $R_{sub}$ = 0.36 AU.

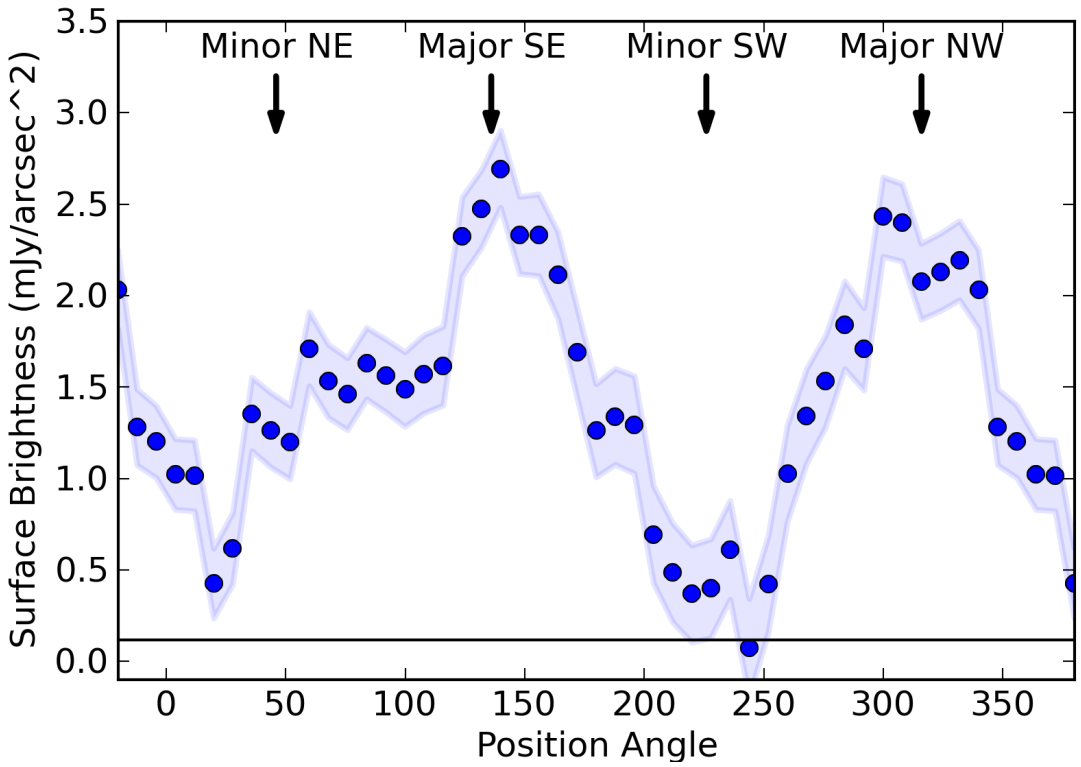


Fig. 4.6.— Binned flux along the azimuthal ring located at 65 AU. Each bin is 8° wide and extends from a projected distance of 55 to 71 AU annulus along the ring seen in this figure.

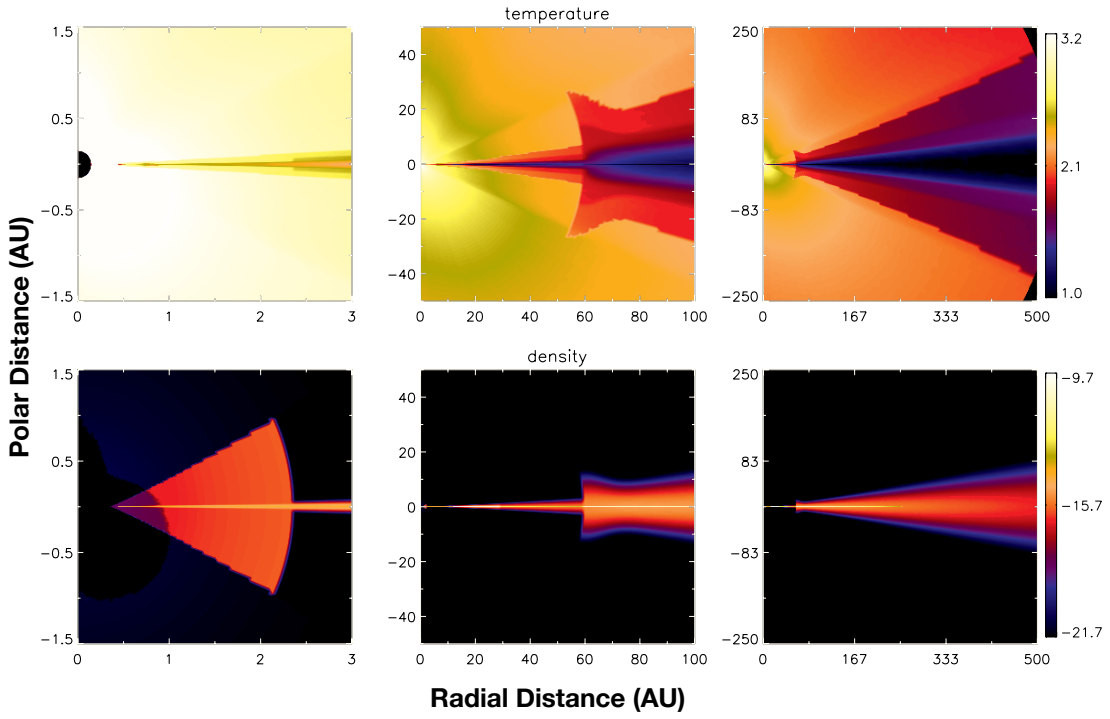


Fig. 4.7.— The top row of panels present temperature profiles for three regions of our MCRT disk model. The bottom row of panels present the density profiles for these same three regions of the disk model.

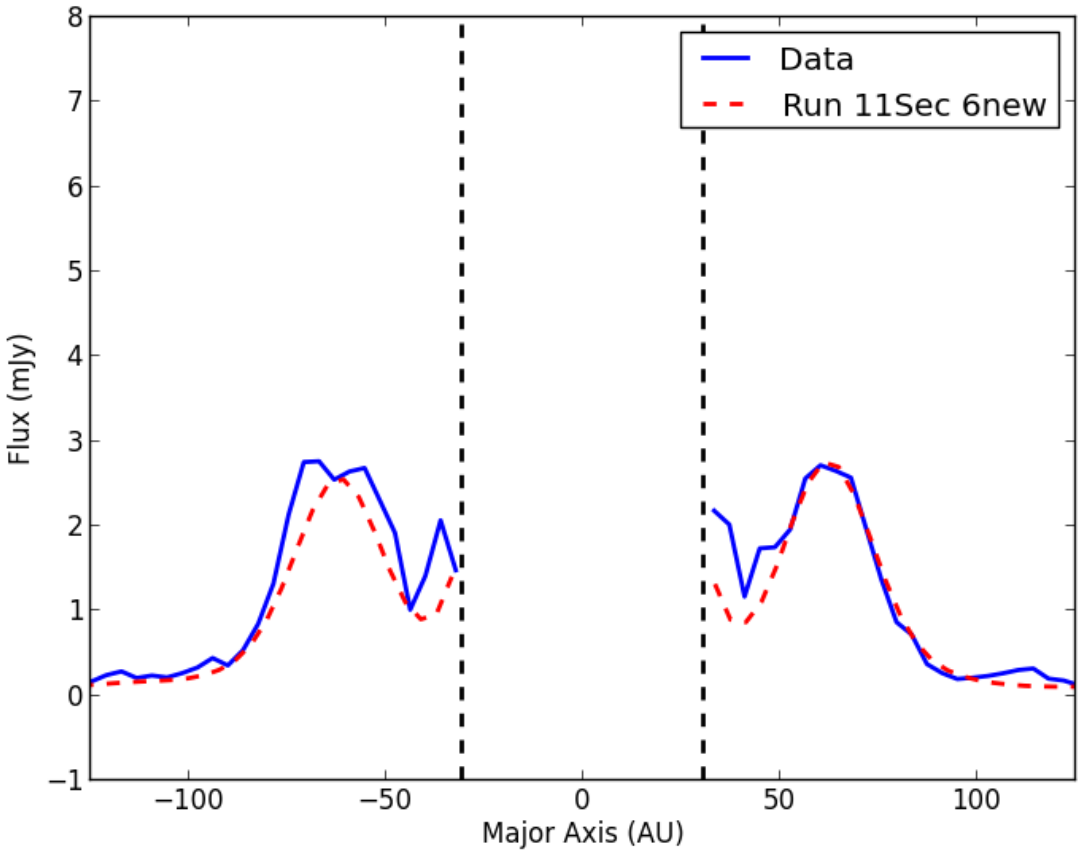


Fig. 4.8.— Major axis crosscut of our 2011 H-band imagery data (PI image) compared to the best fit model (red-dashed line). The vertical dashed lines represent the inner working angle of 0.28”

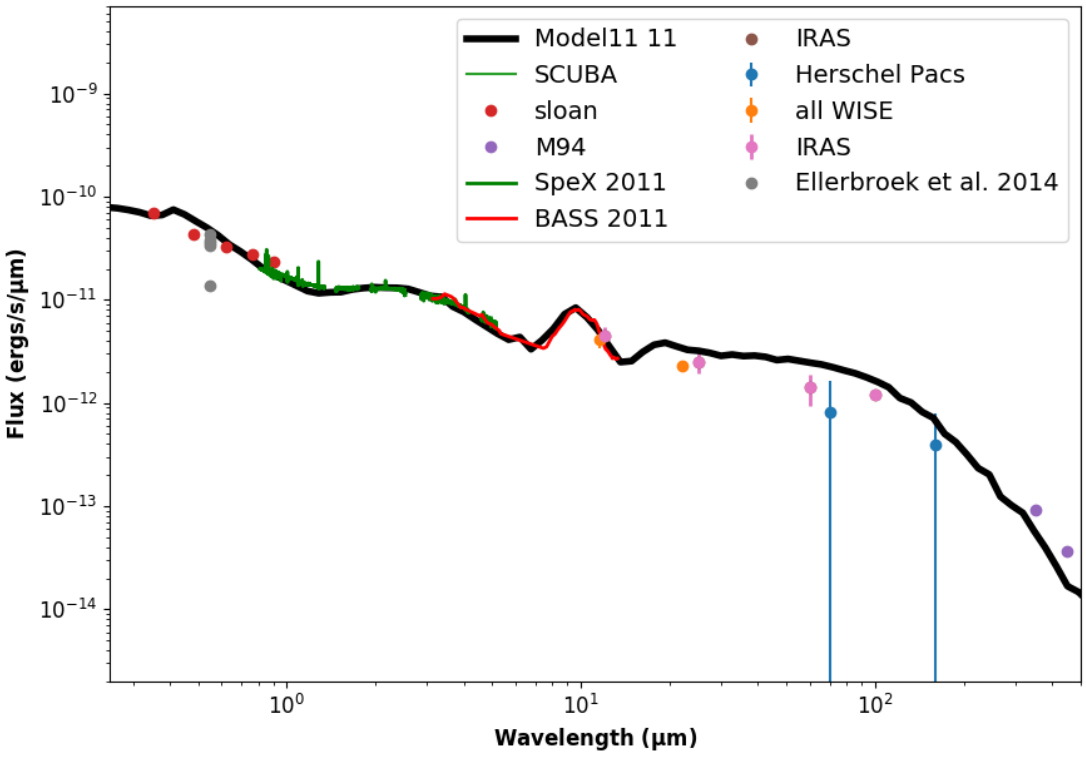


Fig. 4.9.— The observed SED of HD 163296 is shown along with our best fit model SED (black line). The SpeX 2011 (red line) and BASS 2011 (teal line) data are from this work, as described in Section 4.2. The blue circles represent data from the AllWISE catalog (Wright et al., 2010), the green circles are from the 2MASS All Sky Survey (Cutri et al., 2003), and the purple circles are from IRAS point source catalog (Helou & Walker, 1988). The gray circles depict V-band photometry and represent the historical minimum, 1-$\sigma$ below median flux, median flux, and 1-$\sigma$ above the median flux as reported by Ellerbroek et al. (2014).

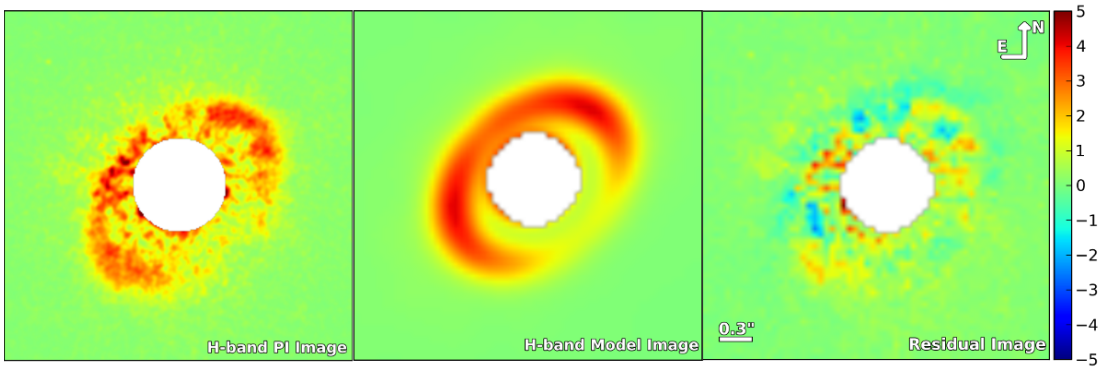


Fig. 4.10.— Our 2011 H-band polarized scattered light image (left panel), the best fit model PI H-band scattered light image (middle panel), and the difference between the observed and model PI image (right panel) are shown. All three panels are displayed on the same linear scale, same spatial scale, and rotated such that North is up and East is left. The inner working angle is masked out with a white circle. Note that the PI image was binned to match the pixel scale of the model for the difference image.

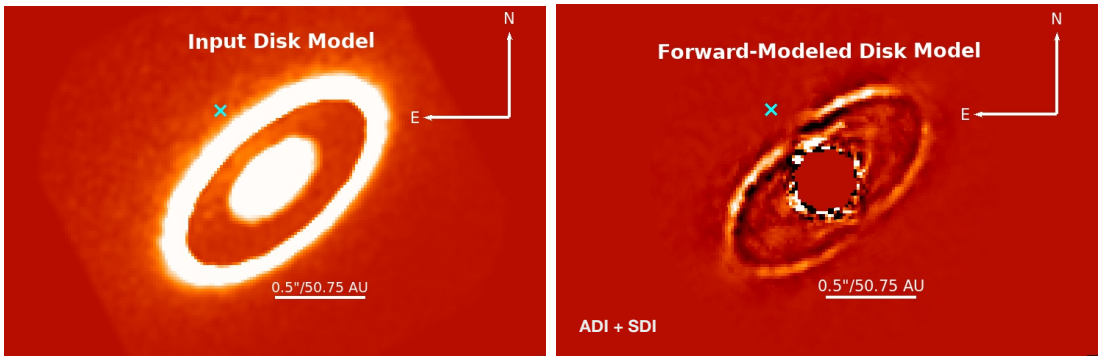


Fig. 4.11.— (left) Broadband image of the best-fit synthetic disk model derived from polarimetry interpolated onto the CHARIS pixel scale and wavelength array and (right) forward-model of the disk after propagating its signal through ADI and SDI. The location of the proposed protoplanet candidate from Guidi et al. (2018) lies well exterior to the azimuthal and radial self-subtraction footprints in the forward-modeled disk. The images have been smoothed with a top-hat filter to more clearly reveal the trace of the disk: localized emission exterior to the disk is an artifact of this smoothing.

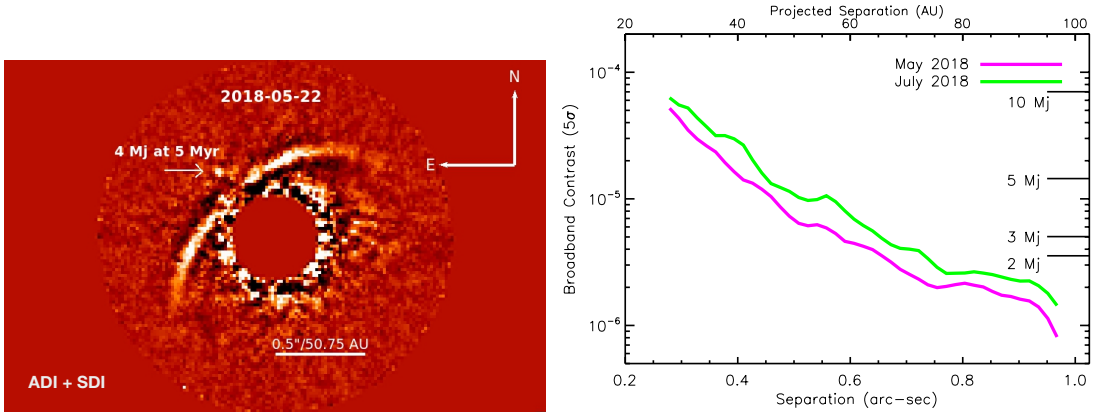


Fig. 4.12.— (left) 2018 May broadband image with a 4 $M_{\rm J}$, 5 Myr-old planet injected into our observing sequence at the location of the candidate from Guidi et al. (2018) ($\Delta$F $\sim 8{\times}10^{-6}$) and propagating its signal through ADI and SDI. Even with signal from the disk contributing to an estimate of the noise, the injected companion is detected at SNR $\sim$ 5. (right) Broadband contrast curve for the 2018 May and 2018 June data compared to broadband contrasts for 2–10 $M_{\rm J}$ planets assuming the Burrows atmosphere models. The 5-$\sigma$ contrast at 0.″49 is in agreement with expectations based on our injected 4 $M_{\rm J}$ planet in the lefthand panel. The contrast for a 1 $M_{\rm J}$ companion lies off the graph at $\Delta$F $\sim 3.7{\times}10^{-7}$.

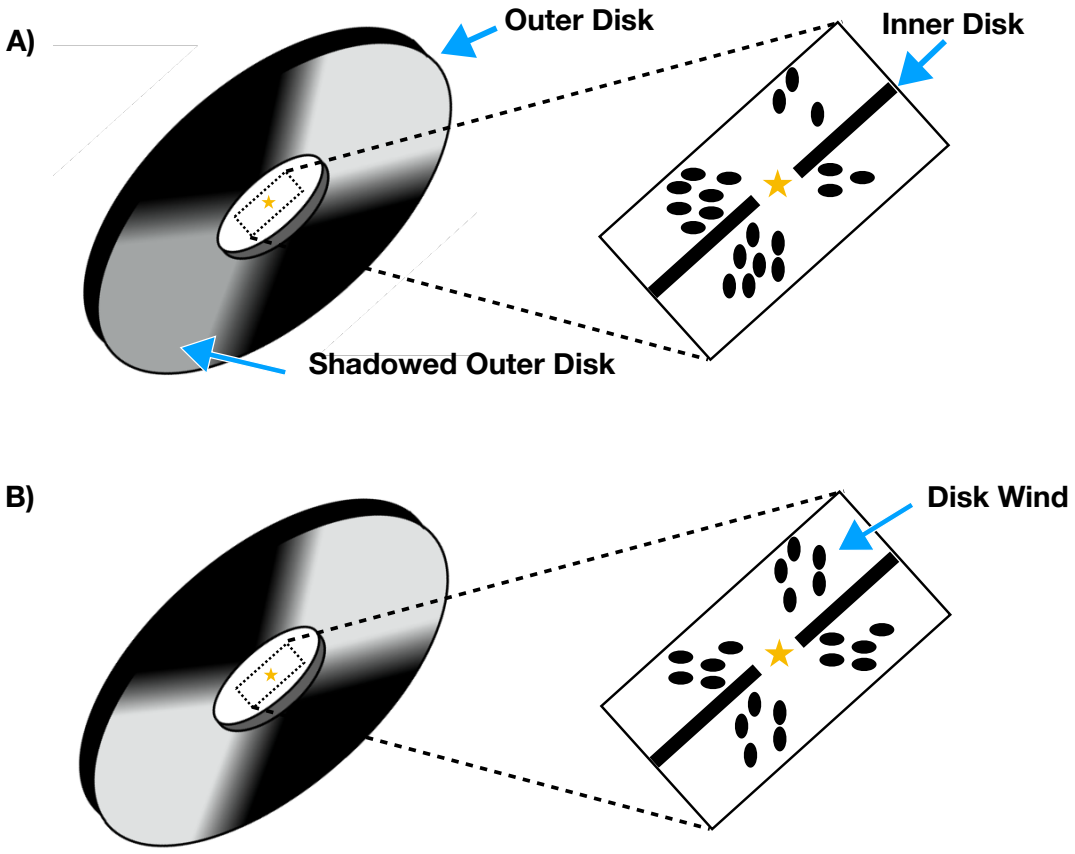


Fig. 4.13.— Diagram of the disk wind model. A) shows the disk wind which is asymmetric which shadows the SE portion of the disk. B) shows a symmetric disk wind where the both sides of the disk are equally illuminated. The left hand side of the diagram shows the outer portion of the disk where the right hand side of the diagram shows a zoomed in version of the disk. The outer disk as been rotated and inclined to match the observed orientation of HD 163296 shown in Figure 4.1.

# Chapter 5

# The Disk and Jet Variability of the Protoplanetary Disk HD163296

## 5.1 Introduction

Protoplanetary disks are dust and gas disks found around young stars, and these systems host the birthplace of planets. Direct imaging of these protoplanetary systems can reveal a disk structure that can constrain the planet formation process. Intermediate-mass stars, Herbig Ae/Be (Herbig , 1960), are more massive analogs to T-Tauri stars and not only host protoplanetary disks but also commonly host collimated bi-polar jets (Herbig , 1950; Wassell et al., 2006; Ellerbroek et al., 2014; Bally, 2016). A plethora of structure can be seen in resolved imaging of Herbig Ae/Be stars such as spiral arms (Hashimoto et al., 2011) or flat settled disks (Meeus et al., 2001). Protoplanetary disks with rings and gaps (e.g., TW Hydrae; Andrews et al. 2016) are of much interest as they may host some of the Jovian protoplanets within the protoplanetary disk itself (Quanz et al., 2013; Currie et al., 2015).

HD 163296 is a young ($5.1^{+0.3}_{-0.8}$ Myr old Montesinos et al. 2009 to $9 \pm 0.5$ Myr old Pikhartova et al. 2019) Herbig Ae protoplanetary disk system located at a distance of 101.5 $\pm$ 1.2 *pc* (Gaia Collaboration et al., 2016, 2018). The disk has been spatially resolved by ground- and space-based observing platforms at a multitude of wavelengths, including: optical (HST/STIS: Grady et al. 2000, HST/ACS Wisniewski et al. 2008), near-infrared (IR) (Subaru/HiCIAO: Rich et al. 2019, Subaru/CHARIS: Rich et al. 2019, VLT/NACO: Garufi et al. 2014, 2017, Gemini/GPI: Monnier et al. 2017, VLT/SPHERE: Muro-Arena et al. 2018,

Subaru/CIAO: Fukagawa et al. 2010, Keck/NIRC2: Guidi et al. (2018)), and radio wavelengths (VLA: Guidi et al. 2016, ALMA: Guidi et al. 2016; Isella et al. 2016, 2018).

The disk structure is highly complex consisting of an inner disk and an outer disk. The inner disk has a small dust ring at 0.″14 (15 AU) inside a continuous inner disk region (Isella et al., 2018)). The outer disk region begins with a gap between the continuous inner disk and the first of two dust rings located at 0.″66 and 1.″0 (67 AU, 101 AU; Isella et al. 2018). The first dust ring at 0.″66 has been detected at both radio (Guidi et al., 2016; Isella et al., 2016, 2018) and near-IR observations (Garufi et al., 2014, 2017; Monnier et al., 2017; Muro-Arena et al., 2018; Rich et al., 2019). The disk extends to at least 4.″4 (447 AU) (Wisniewski et al., 2008) and two ansae (broken rings) have been detected at 2.″9 (294 AU) SE of the star and 3.″2 (325 AU) NW of the star (Grady et al., 2000). We note that we choose to refer to these features as ansae to keep labeling consistent between published works (e.g. (Grady et al., 2000),(Wisniewski et al., 2008)), but alternatively could be labeled as a 3rd dusty ring. Finally, the disk has exhibited time-dependent flux variability. First, HST/ACS observations observed only one ansa in one imaging epoch and no ansae in the next epoch (Wisniewski et al., 2008), and a 1 STMag/" dimming of the disk flux between the HST/ACS and HST/STIS observations. Next, Rich et al. (2019) showed that the near-IR scattered images of the first ring varied on a timescale $< 4$ yr.

The HD 163296 system hosts three planetary candidates. Modeling of ALMA gas emission data suggest Jovian-mass planets at 0.″82 and 1.″35 (83 and 137 AU; Teague et al. 2018) and a single Jovian mass planet on an even wider orbit at 2.″56 (260 au Pinte et al., 2018). Additionally, there was a fourth candidate detected with Keck/NIRC2 thermal infrared imaging (7 $M_{\rm J}$; (Guidi et al., 2018)) just

outside the first dust ring, but follow up imaging did not detect the planet (Rich et al., 2019).

HD 163296 is also associated with an active bi-polar jet HH409 first discovered through space based corographic images and verified with long slit spectroscopy (Grady et al., 2000; Devine et al., 2000). Since then, several studies have detected more knots and properties of the jet (Wassell et al., 2006; Günther et al., 2013). In particular, Ellerbroek et al. (2014) measured the proper motion and radial velocities of the 11 HH-knots associated with HD 163296 and predict that HD 163296 periodically ejects its HH-knots with a regular period of 16 $\pm$ 0.7 yr. With the last HH-knot thought to have been ejected in 2002, we expect the next HH-knot launch to occur within 2018. Optical photometric and IR spectroscopic monitoring revealed suggestive evidence of optical flux dimming and IR flux increasing on similar timescales to the ejection of the HH-knots (Sitko et al., 2008; Ellerbroek et al., 2014). Fianlly, Ellerbroek et al. (2014) also identified additional decreasing flux events. These could be "dipper" events that have previously been seen other protoplanetary systems (Cody et al., 2014; Pinilla et al., 2018).

In this paper, we present two new epochs of Hubble Space Telescope (HST) coronagraphic imaging of HD 163296's protoplanetary disk with the Space Telescope Imager and Spectrograph (STIS). Additionally, we present new multi-wavelength monitoring of the star from 2016-2018 to search for the launch of the predicted HH-knot. Finally we re-analyze an older epoch of HST/STIS imagery and previous multi-wavelength observations of the star. Observations and reductions of the data are discussed in section 5.2. Next we analyze the HST/STIS data in section 5.3 and the multi-wavelenght observations in section 5.4. Finally, we discuss our results in section 5.5 and conclude in section 5.6.

## 5.2 Observations and Reductions

### 5.2.1 AAVSO Observations

Optical observations of HD 163296 were taken from 2018 March 18th to 2018 November 7th in B-, V-, and I- bands with an observing cadence of 1 observation per day. Data were obtained through a request through AAVSO and taken by observers part of AAVSO. Standard stars UCAC4 341-118672 and UCAC4 340-118109 were utilized in the reduction. Data was reduced using the photometry reduction software *LESVEPHOTOMETRY* V1.2.0.90 [a]. All of the optical photometric observations are plotted in Figure 5.1.

### 5.2.2 HST/STIS Observations

The protoplanetary disk around HD 163296 was observed with HST/STIS three times at optical wavelengths. Two new epochs of observations were taken on 2018 April 14th and 2018 July 18th (2018 Apr. and 2018 Jul. epochs). Both of these epochs consisted of 4 consecutive orbits with orbits 1, 2, and 4 observing HD 163296 and the 3rd orbit observing the PSF star HD 141653. Each orbit observed the targets with occulting bar positions A1.0 and A0.6 where the width of the bars are 1.″0 and 0.″6 respectivly. The exposure times for the 2018 Jul. epoch are slightly shorter to allow for the entire CCD to be readout where as the 2018 Apr. epoch only had the bottom half of the CCD readout. Additionally, HD 163296 was previously observed in 1998 September 2nd and 3rd (1998 Sep. epoch), which was first presented in Grady et al. (2000). These observations only utilized the A1.0 occulting bar and did not include contemporaneous PSF star observation. Additionally, the final orbit of the epoch was a day after the first two orbits. A

[a] http://www.dppobservatory.net/

full list of the observations can be found in Table 5.1.

Our reduction method subtracted the PSF from the science image in the science image frame, following the techniques outlined Grady et al. (2000). The target stars were centroided by using the "x" marks the spot method developed by Schneider et al. (2009). The flux of the PSF star was scaled based on the V-band observed magnitude and the V-band observed magnitude of HD 163296, which will be discussed further in the subsequent paragraphs. The PSF star's were chosen based on their similar B-V color to HD 163296. Examples of the PSF subtracted science frames are shown in Figures 5.2, 5.3, 5.4, 5.5, and 5.6 with a red cross denoting the location of the star HD 163296. After the science frames have been PSF subtracted, the images are centered, the spider arms and occulting bars are masked, and the images are de-rotated to the North up East left positions. The reduced science frames were median combined creating 4 final images, one for each combination of wedge position and epoch shown in Figures 5.7, 5.8, 5.9, 5.10, and 5.11. Note that while 2018 Apr. and 2018 Jul. epochs were taken as part of the same observing program, we choose not to stitch these observations together as has previously been done by Schneider et al. (2009). There is evidence of disk flux variability over time between the two 2018 epochs that we will discuss below in sub-sections 5.3.1 and 5.5.1.

We reduced the 2018 Apr. and Jul. epochs of HD 163296 using the method described above. HD 163296 is a known aperiodic variable star as shown by (Ellerbroek et al., 2014) and in our 2018 optical light curve in Figure 5.1. Thus without high precision contemporaneous optical photometry, it remains difficult to scale the PSF star to match the flux of the science target. The 2018 Jul. epoch observations has contemporaneous photometry taken on 2018 July 15th with measured V-band magnitudes of 6.797 $\pm$ 0.013 mag and 6.729 $\pm$ 0.013. We found the best scaling factor was 0.1773 (PSF star V-band = 4.928 mag) by

varying the scaling factor of the PSF and selecting the one that resulted in the most star flux removed while minimizing over-subtraction of the disk. Our best scaling factor is equivalent to a V-band magnitude of 6.80 mag for HD 163296 matching well with the contemporaneous photometry. The same methodology was applied to the 2018 Apr. epoch. The closest photometry points were from the AAVSO optical photometry with values of 6.714 ± 0.011 mag and 6.812 ± 0.01 mag on 2018 April 15th. We found that these values over-subtracted the PSF and found the best scale values of 0.1680 with a corresponding V-band magnitude of V = 6.87 mag. This result is within 0.1 mag of the observed photometry the day before the 2018 Jul. epoch. We looked for variation in flux from HD 163296 within a given observing window epoch and did not detect any significant brightness changes.

We re-reduced the 1998 Sep. epoch data which was originally presented in Grady et al. (2000). The 1998 Sep. epoch does not have contemporaneous observations of a PSF star thus making the residual noise of the PSF subtracted final image noticeably larger than compared to the 2018 epoch data. We tested several other PSF stars previously observed with HST/STIS (HD 135298, HD 36546, HD 145570, and HD 141653) using the A1.0 wedge to try and reduce the residual noise. We concluded that the PSF star HD 141653 used in Grady et al. (2000) was still the best PSF match. We found the same scaling factor of 0.213 utilized by Grady et al. (2000) (PSF V = 5.194 mag, Science V = 6.873 mag) best removed the stellar light from the science images. We visually compared the new final image using our new reduction to that of Grady et al. (2000) and found that we reduced the number of residual speckles around the ansae region of the disk, or the "wagon wheel spoke" effect. We will utilize our new reduction of the 1998 Sep. epoch data for the rest of this work.

### 5.2.3 Near IR Reduction

We performed a near-IR monitoring campaign from 2016-2018 on HD 163296 using NASA's Infrared Telescope Facility (IRTF) and at Apache Point Observatory (APO). We performed a total of 11 observations from 2016 April to 2018 September using SpeX spectrograph (Rayner et al., 2003) at IRTF in its short-wavelength mode (0.8 - 2.4 $\mu m$) and long-wavelength mode (2.3-5.5 $\mu m$) (see Table 5.2) using an $0\farcs8$ wide slit. Additionally, we performed 3 observations in 2018 April and 2018 May with the TripleSpec spectrograph (Wilson et al., 2004) at the APO 3.5m telescope, covering a spectral range of (0.95 - 2.46 $\mu m$) (see Table 5.2). We observed A0V star HD 163336 for telluric corrections and flux calibration for all observations. Observations noted in Table 5.2 had contemporaneous IRTF/SpeX prism spectra taken with a $3\farcs0$ wide slit, which was utilized to correct for absolute flux variations. Observations without prism spectra were scaled to match the observations with prism data based on their optical flux component of their spectra (0.8-0.9 $\mu m$). These observations were reduced and calibrated using the standard reduction packages *Spextool* and *Triplespectool* respectivly (Vacca et al., 2003; Cushing et al., 2004). Near-IR observations on 2018 May 16 and 2018 June 24 were previously presented in Rich et al. (2019). Sample SpeX and TripleSpec spectra are plotted in Figure 5.12.

### 5.2.4 VLA Reduction

HD 163296 was observed with VLA using the C-band receiver 6 times between 2018 March to 2018 November, with 3 observations in A configuration and 3 observations D configuration described in Table 5.2. The two 1 GHz band-passes were centered at 4.76 and 7.36 GHz. J1820-2528 was observed to calibrate the complex gain, and 3C286 was observed to calibrate the bandpass and absolute flux

density scale. Observations were intended to be scheduled one month apart and to coincide with the HST/STIS observations, but due to instrument difficulties at VLA, observations were not possible between May and September of 2018. We utilized the standard CASA 5.1.2 reduction pipeline (McMullin et al., 2007) to analyze the data. Fluxes were measured from cleaned images by fitting a gaussian profile to the flux images using the *imfit* tool. Measured fluxes are shown in Table 5.3.

## 5.3 HST/STIS Analysis

### 5.3.1 Disk geometry

Optical scattered light disk flux is observed in all of the HST/STIS epochs as shown in Figures 5.7, 5.8, 5.9, 5.10, and 5.11. For all epochs, we observe disk flux from the masked wedge region ( 0.5") to 5" (500 au). The disk major axis is oriented approximately at PA of 132° similar to what has previously been observed (Isella et al., 2016) and is inclined. In the re-reduction of the 1998 Sep. epoch, we observe the two ansae (SE and NW ansae) originally presented by Grady et al. (2000), located at a projected distance of 3.″3 (330 au). Additionally, we observe the SE ansae in the 2018 Apr. epoch and the NW ansae in the 2018 Jul. epoch. These ansae form a broken ring structure located at a projected semi-major axis of 3.″3 (330 AU). The disk ring flux distribution appears similar to the broken ring structures seen at smaller radii (0.″65, 66 AU) in near-IR observations (Rich et al., 2019; Muro-Arena et al., 2018; Garufi et al., 2017; Monnier et al., 2017). Assuming that the broken ring is circular and the projected the disk inclination of 42° and PA of 132° (Isella et al., 2016), we plotted an ellipse on the 1998 Sep. epoch image (Figure 5.13) and found that the broken ring disk is consistent with

a minor axis offset of 0.″7. The 2018 Apr. and 2018 Jul. observations are also consistent with this minor axis offset. Minor axis offests for HD 163296 have been measured before on an interior radii ring located at 0.″65 (66 au) (0.″0432 ± 0.″0016, Rich et al. 2019; 0.″06, Garufi et al. 2014; 0.″105 ± 0.″045, Muro-Arena et al. 2018; 0.″1, Monnier et al. 2017). The minor axis offset is due to an inclined thick disk being projected onto the sky.

There is an additional non-azimuthal flux of the disk that can be found north of the NW ansa, increasing in intensity as it approaches the NE minor axis. These features can be observed in all five final images (Figures 5.7, 5.8, 5.9, 5.10, and 5.11). Figure 5.14 annotates the peripheral disk feature in the 2018 Jul. epoch with the 1.0A wedge disk excess feature. This feature only appears in the forward (closest) portion of the disk and is more prominent on the north side of the minor axis. Additionally, this feature is broader than the ansae interior to the disk excess described above.

### 5.3.2 Disk Surface Brightness Asymmetry

We investigated disk surface brightness asymmetry along the azimuth axis of the disk for both the ansae region (300-360 au) and the peripheral disk region (420 - 500 au). We plotted the binned flux in elliptical annuli with an assumed inclination of 42° and PA of 132° from (Isella et al., 2016) shown in Figures 5.15, 5.16, 5.17, and 5.18. An example of the projected elliptical annuli is shown in Figure 5.13. In the surface brightness plots, we used 3-$\sigma$ error bars for the elliptical annuli regions with the error propagation including photon noise, read noise, and dark noise. Finally, we note that a few of the azimuthal bins are contaminated by background stars causing these regions to have abnormally high flux. Specifically, the minor south-east axis has three stars that contaminate the total amount of

flux.

The azimuthal surface brightness from the ansae region of the disk (3rd dusty ring; 300-360 AU) are plotted in Figures 5.15 and 5.16 for both wedge A1.0 and A0.6 respectively. We see variation in the surface brightness of the ansae region of the disk both azimuthally and in time. Starting with the 1998 Sep. epoch, the disk is brighter towards the NE minor axis than the SW minor axis. Additionally, the SE and NW ansae appear to be approximately equally bright with the SE ansa being 19.65 ± 0.11 STMag/" (PA=124°) and the NW ansa being 19.29 ± 0.10 STMag/" (PA=332°). However, the slope of the ansa's increasing surface brightness from the SW minor axis to the NE minor axis is different. For the 2018 Apr. epoch, only the SE ansa is observed but is dimmer (20.40±0.02 STMag/"; PA= 124°) than the 1998 Sep. epoch. Additionally, the SE ansa is increasing in surface brightness from the SW minor axis to the NE minor axis just like the SE ansa in the 1998 Sep. epoch. The surface brightness were the NW ansa should be located is flat and is much dimmer (20.68±0.02 STMag/"; PA=332°) than the 1998 Sep. epoch. Finally for the 2018 Jul. epoch, only the NW ansa is observed but is dimmer (20.08±0.01 STMag/"; PA=332°) than then 1998 Sep. epoch. The SE ansa region in the 2018 Jul. epoch is dimmer (20.78±0.02 STMag/"; PA=124°) than both the 1998 Sep. and 2018 Apr. epochs. Additionally, the 2018 Jul. epoch surface brightness around the SE ansa has a dip in surface brightness. For the 2018 Apr. and Jul. epochs, the results of the larger 1.0A wedge observations are consistent with the smaller 0.6A wedge observations. Thus none of the epochs presented above have the same disk surface brightness distribution. We will discuss these results in subsection 5.5.1.

The peripheral disk brightness located at a projected semi-major axis of 420-500 AU appears to be similar in structure in all three epochs as shown in Figures 5.17, and 5.18. We note that all epochs show the same trend, the disk brightness

increases as you approach the NE minor axis. We note that the NE minor axis is the forward scattering portion of the disk. While the major axis flux points are consistent with the background flux, the surface brightness towards the north-east minor axis exhibits an excess. Additionally, we see little to no surface brightness variability with time as compared to the ansa region described above. The 2018 Jul. and Apl. epochs are still dimmer (2018 Apr.: 20.54±0.02 STMag/", 2018 Jul. 20.17±0.02 STMag/") than the 1998 Sep. epoch (19.85 ± 0.10 STMag/") at a PA= 12°, but have little variation between the two 2018 epochs azimuthally. Note that the south-west minor axis also exhibits an excess however this is due to the presence of background stars within the bins along that minor axis. Due to its non-azimuthal nature, it is unlikely that this excess is an effect of a poor PSF subtraction.

### 5.3.3 HH-knots

We observe 2 HH-knots in the 1998 Sep. image wedge 1.0A image located along the minor axis (see Figures 5.7, 5.8, and 5.9) which were first reported by Grady et al. (2000) and further discussed by Devine et al. (2000). However, we do not see any HH-knots in the 2018 Apr. and 2018 Jul. epochs. Due to the measured high proper motion of the HH-knots (Ellerbroek et al., 2014), (Red Jet: $v_{t,red} = 0.28 \pm 0.01"/yr$, Blue jet: $v_{t,blue} = 0.49 \pm 0.01"/yr$), we do not anticipate observing the C HH-knot that was observed in 1998 Sep. in the field of view plotted in Figures 5.7, 5.8, and 5.9. However, since the 1998 Sep. imaging, HH-knots have been launched from HD 163296 and have been observed by Ellerbroek et al. (2014) and Wassell et al. (2006).

Utilizing the HH-knot proper-motion analysis from Ellerbroek et al. (2014) and citations therein, we indicated the predicted locations of the HH-knots for summer

2018 in Figure 5.19 with blue arrows along a minor axis crosscut. Note that we only used the full frame images from the 2018 Jul. epoch for this comparison. We inserted fake HH-knots into the images at the predicted locations of HH-knots B, and C and performed aperture photometry and found that the knots could presently be 15 times dimmer and be detected at 3-$\sigma$ above the background. We will discuss further the non-detection of the HH-knots in sub-subsection 5.5.3.

## 5.4 Optical, Near-IR, and Radio Analysis

We performed a multi-wavelength monitoring campaign in the optical, near-IR, and radio wavelengths to try and detect the predicted launch of an HH-knot from HD 163296. Below we will describe the optical, near-IR, and radio variability along with the measured accretion history.

### 5.4.1 Optical variability

Optical photometry in B-, V-, and I-bands from an AAVSO monitoring campaign is shown in Figure 5.1. The light curve remains relatively flat with the exception of one dipper event around 2018 June 7th and a second potential dipper event around 2018 August 7th. The first event is partially seen rising from a dimmer state to the average brightness state over a several day period. We note that the first dipper event occurs between the 2018 Apr. and 2018 Jul. HST/STIS epochs. The second dipper event is only observed by a single night observation. The second dipper event could have resulted from poor seeing conditions thus we only mark it as a tentative detection. Both of these dipper events are hampered by gaps in the observing cadence. We note that analysis of the dipper events themselves such as their reddening and occurrence rate will be analyzed by Pikhartova et al. (2019).

The largest dipper event currently known for HD 163296 occurred in 2001 with

a magnitude change of  1 mag and lasted several months (Ellerbroek et al., 2014). Smaller dipper events such as the one we detected around 2018 June 7th have also occurred before (Ellerbroek et al., 2014). Since dipper events are thought to be caused by dust, they do not have instinct shapes; thus we cannot predict how deep the 2018 June 7th dipper event was. This first dipper event in our optical sample dipped down to at least 7.22 mag. The depth of these dippers are at least as deep as the 4 previous dipper events reported in Ellerbroek et al. (2014).

### 5.4.2 Near-IR Variability

We quantified the variability of our near-IR spectra taken with IRTF/SpeX and APO/Triplespec by convolving a K-band filter with the flux calibrated spectra to extract a magnitude. The extracted magnitudes are listed in Table 5.4 and plotted in Figure 5.20. We have also included historical K-band magnitudes previously accumulated and presented in Ellerbroek et al. (2014) and citations therein. Note that the K-band magnitudes from Ellerbroek et al. (2014) did not have error bars provided with the publication, thus we assumed 10% errors for their data, similar to the size of our error bars. The K-band light curve from 2003 to 2018 has some some variation on a timescale of months, with increased flux around 2012. Additionally, we see a drop in flux in 2016 as compared to the last observations in 2012, and we see a slow increase in near-IR flux from 2016 to 2018. However, given the size of our uncertainties, these trends cannot be certain. We do not see any outburst events such as the 2002 outburst that possibly coincided with the launch of an HH-knot (Ellerbroek et al., 2014; Pikhartova et al. , 2019).

### 5.4.3 Accretion History of HD 163296

We calculate the mass accretion rate outlined in Ellerbroek et al. (2014). Equivalent widths (EW) of the Br$\gamma$ line were measured using *IRAF splot* tool using a gaussian function. The measured equivalent widths are listed in Table 5.4. In order to calculate the line luminosity, we first correct our measured $EW_{obs}$ by removing the effect the photospheric line as shown in Equation **5.1**. We adopt the same photospheric EW ($EW_{phot}$ = -22 Å) as Mendigutía et al. (2013) and the same reddening ($A_V$ = 0.5 mag) as Ellerbroek et al. (2014). We use these values to calculate the line luminosity ($L_{line}$; Equation **5.2**). We then converted the line luminosity into the accretion luminosity in Equation **5.3** utilizing the relation by Mendigutía et al. (2011). Finally, the mass accretion rate is calculated in Equation **5.4** assuming an $R_*$ = 1.7 $R_\odot$ Pikhartova et al. (2019). The values are listed in Table 5.4 and plotted in Figure 5.20. We recalculated the accretion rates previously presented in Ellerbroek et al. (2014) and included the updated distance and $R_*$ values. We see a constant accretion rate from 2003 to 2018 as shown in Figure 5.20.

$$EW_{\rm cs} = EW_{\rm obs} - EW_{\rm phot} 10^{-0.4|\Delta K|} \tag{5.1}$$

$$L_{\rm line} = 4\pi d^2 EW_{cs} F_K 10^{0.4 A_K} \tag{5.2}$$

$$\log(\frac{L_{\rm acc}}{L_\odot}) = 3.55(\pm 0.80) + 0.91(\pm 0.27) \times \log(\frac{L_{\rm Br\gamma}}{L_\odot}) \tag{5.3}$$

$$\dot{M}^*_{\rm acc} = \frac{L_{\rm acc} R_*}{G M_*} \tag{5.4}$$

### 5.4.4 Radio Flux Variability

Fluxes from the C-band VLA observations are listed in Table 5.3. During the launch of an HH-knot, we estimated to observe the radio flux increase by 50% based on previous measurements of HH-knot launches (Devine et al., 2000). Additionally, we should observe a change in the spectral index, with the value possibly becoming negative. We do not observe any significant changes in the C-band flux to suggest the launch of an HH-knot. Additionally, our spectral index values are positive which is consistent with flux originating as thermal emission. Our radio observations are consistent with no HH-knot being launched during its observing window in 2018.

## 5.5 Discussion

### 5.5.1 Disk Structure and Illumination

We measured a minor axis offset value of $0\farcs7$, which is larger than minor axis offset values measured for the 1st dust ring in the near-IR ($0\farcs0432 \pm 0\farcs0016$, Rich et al. 2019; $0\farcs06$, Garufi et al. 2014; $0\farcs105 \pm 0\farcs045$, Muro-Arena et al. 2018; $0\farcs1$, Monnier et al. 2017). With our minor axis offset and the assumed inclination and orientation of the disk, we find that the ansae are consistent with a broken ring structure. Thus we conclude that the ansae previously observed by Grady et al. (2000) and Wisniewski et al. (2008) are part of a 3rd ring that has not previously been detected by radio or near-IR observations of the system. We cannot verify our minor axis offset value for the 3rd ring as observations of the 1st ring are of a different region of the disk and of a different bandpass than our observations. We can state that the 1st ring must be shorter in height above the midplane, therefor a smaller minor axis offset, than the ansae region, which is similar to what we

observe. These measurements can be used for future modeling of HD 163296 to constrain the small grains hight above the midplane of the disk.

Our data are consistent with time variable disk flux described in section 5.3.2 were we observe both ansae in the 1998 Sep. epoch but only a single ansa in the 2018 Apr. and Jul. epochs. Disk illumination variations now can occur in HD 163296 in $< 3$ months timescale. Previously, Wisniewski et al. (2008) observations with HST/ACS detected the SE ansae in one epoch but did not detect either ansae in a second epoch. However, these epochs of observations were in different color filters leaving the possibility that this could be a color effect. As shown in Rich et al. (2019) and Wisniewski et al. (2008), the disk around HD 163296 exhibits variability. Due to the similar illumination of the 3rd outer ring as compared to the illumination of the 1st ring observed in the near-IR, we conclude that a similar variable illumination mechanism is at play. As discussed in Rich et al. (2019), the mechanisms at play could be a warped inner disk structure shadowing the outer disk (Sitko et al., 2008), or dust ejected above the mid-plane of the disk that shadows the outer disk (Ellerbroek et al., 2014).

### 5.5.2 Optical and Near-IR light curve variability

The optical and near-IR light curves, Figures 5.1 and 5.20 respectively, remain relatively constant over time. Thus we see no evidence of the launch of an new HH-knots within our observing windows. The optical light curve exhibits two dipper events in 2018 June 7th and 2018 August 7th. We do not have any contemporaneous near-IR observations during those dipper events. Additionally, there is possibly long term variability in the near-IR flux observations. Our observations at the beginning of 2016 are a few tenths of a magnitude dimmer and the K-band flux increases with time from 2016-2018. Long term variability in the IR

light curves of disk hosting stars has previously been found by Cody et al. (2014). Thus if the optical lightcurve observations do not also have these long term variations, then it is possible that there are two mechanisms at work causing the variability of HD 163296.

Hd 163296 joins a small group of protoplanetary disk hosting stars that exhibit variability in their optical/near-IR resolved disk flux and also exhibit dipper events (e.g. RX J1604.3-2130; Pinilla et al. (2018)). These dipper events and time variable disk illumination possibly share the same shadowing mechanism (eg. warped inner disk, asymmetric disk wind). Thus it is clear that when we interpret direct imaging of protoplanetary disks in optical and near-IR wavelengths, we must consider the entire system. In some cases, as for HD 163296, we need contemporaneous observations to help interpret our results and multiple direct images of the protoplanetary disk as given the plethora of times HD 163296 has been imaged, it hardly ever shows the same disk flux distribution twice.

### 5.5.3 Jet Activity

We have not detected the launch of a new HH-knot as of 2018 Nov. 3rd. Ellerbroek et al. (2014) predicted that the system should launch a knot every 16 $\pm$ 0.7 yr calculated from proper motion and radial velocity of current HH-knots. With the last known launch of an HH-knot predicted to have occurred  2002; thus the next launch should occur  2018. Additionally, it is predicted from Ellerbroek et al. (2014) that there should be an observed decrease in optical flux from the reddening due to the disk wind and an increase in the near-IR flux from thermal radiation from dust in the disk wind. Instead, we see two minor optical dimming events in 2018 (see Figure: 5.1) and see a general decrease in near-IR flux from 2016-2018 as compared to Ks-band photometry before 2013. Additionally, we

do not detect any HH-knot activity in the HST/STIS images (see Figure 5.19). It remains possible that the HH-knot predicted in 2018 will occur in 2019 and continued monitoring of the system is needed.

We do not detect any of the previously lanunched HH-knots in our 2018 Apr. and Jul. HST/STIS imaging. Günther et al. (2013) notes if an HH-knot is not shock-heated, the knot itself can cool on a timescale of $\tau = 0.4$ yr, thus it is possible that the HH-knots have cooled sufficiently such that they are no longer visible. We strongly note that the lack of detection of HH -knots does not necessarily correlate with a change in the activity of the Jet itself. As the HH-knots are primarily fed energy through shock heating and cool on relatively short timescales, the HH-knots could be interacting with less ISM material than previously and they have cooled sufficiently to no longer be detectable with our 2018 Apr. and Jul. epoch imagery. Alternatively, we could be observing the end of the Jet activity for HD 163296. Future observations of to directly measure the current jet activity and confirmation of the dimmed HH-knots with deeper ground-based slit-spectroscopy are necessary steps to constrain what is occurring with the HH-knots and jet associated with HD 163296.

### 5.5.4 Effects of Planet Candidate on Disk

Pinte et al. (2018) proposed a 2 $M_{jup}$ mass planet located at 260 AU based on a kink keplerian velocity of the gas around HD 163296. We do not observe any excess flux at this region of our image, which is expected as such a planet is too dim to be detected with our HST/STIS observations. We can look for effects of the planet on the disk. In Figure 5.14, we have placed a dimond at the approximate separation and position angle of the proposed planet. Interestingly, the planet is located between the 2nd dusty disk ring and the ansae region (3rd ring). Much

like the 1st, and 2nd rings Teague et al. (2018), the 3rd ring could be formed through dynamics of the Pinte et al. (2018) planet. New dynamic modeling of the disk that includes the Pinte et al. (2018) planet and the two proposed planets by Teague et al. (2018) in the two inner gaps and replicates the inner disk structure observed in the near-IR and the disk structure in the optical presented in this work could be very interesting to constrain the dynamics of the system.

## 5.6 Conclusions

We report two new HST/STIS coronagraphic imaging epochs taken of HD 163296. We also report a multiwavelength (optical, near-IR, radio) monitoring campaign of HD 163296 taken from 2016-2018. Finally, we reprocessed archival HST/STIS coronagraphic imaging epoch taken in 1999 Sep. and recalculate accretion measurements from the Br$\gamma$ line taken from 2003-2013.

- Ansae features previously identified by (Grady et al., 2000) are a 3rd ring in the outer disk with semi-major axis of $3\farcs$ and a minor axis offset of $0\farcs7$.

- We observed disk flux illumination variability between all three of the HST/STIS epochs with drastically different flux distributions between the 2018 Apr. epoch and the 2018 Jul. epoch. Though disk illumination has previously been reported for HD 163296 (Rich et al., 2019; Wisniewski et al., 2008), this is the shortest time interval for the disk illumination has occurred. Thus disk illumination variations now can occur in HD 163296 in $<$ 3 months timescale.

- We do not detect the an ejection of any new HH-knots, that was predicted to occur in 2018 (Ellerbroek et al., 2014). More monitoring of HD 163296 is still needed to see if the knot launch in 2019.

- We do not detect any of the HH-knots previously launched from HD 163296. The HH-knots could be experiencing less shock-heating and have cooled sufficiently to not be observable with our HST/STIS observations.

- We partially detected dipper event and a potential second dipper event in our optical light curve over the 2018 summer. These dipper events were similar to other small dipper events previously presented by Ellerbroek et al. (2014), but not as large as the 2001 outburst.

- The predicted Pinte et al. (2018) planet is projected to be located within the gap between the second and third rings. This is possibly further evidence of the 2 $M_{jup}$ mass planet's existence.

The authors recognize and acknowledge the significant cultural role and reverence that the summit of Maunakea has always had within the indigenous Hawaiian community. We are most fortunate to have the opportunity to conduct observations from this mountain.

| Telescope /Instrument | Target Name | Date | Total Exposure (sec) | Notes |
|---|---|---|---|---|
| HST/STIS | HD 163296 | 1998 Sep. 02 | 864; ··· | Wedge A1.0 |
| HST/STIS | HD 141653 | 1999 Jun. 28 | 782; ··· | Wedge A1.0; PSF Star |
| HST/STIS | HD 163296 | 2018 Apr.14 | 4050; 552 | Wedges A1.0 and A0.6 |
| HST/STIS | HD 145570 | 2018 Apr. 14 | 896; 134.4 | Wedges A1.0 and A0.6; PSF Star |
| HST/STIS | HD 163296 | 2018 Jul. 18 | 3780; 552 | Wedges A1.0 and A0.6 |
| HST/STIS | HD 145570 | 2018 Jul. 18 | 896; 134.4 | Wedges A1.0 and A0.6; PSF Star |

Table 5.1:: HST/STIS observations of the three epochs. The total exposure is the sum total of the exposures for that epoch with that wedge posisition, for that target. Note that for 3 of the exposures in epoch 20180718 for wedge A1.0, the exposures were smaller to allow for the entire CCD to be read out.

| Telescope/Instrument | Target Name | Date | Spectral Coverage |
|---|---|---|---|
| IRTF/SpeX | HD163296 | 20160404 | 0.7 - 5.3 ($\mu m$) |
| IRTF/SpeX | HD163296 | 20160504 | 0.7 - 5.3 ($\mu m$) |
| IRTF/SpeX | HD163296 | 20160609 | 0.7 - 5.3 ($\mu m$) |
| IRTF/SpeX | HD163296 | 20160810 | 0.7 - 5.3 ($\mu m$) |
| IRTF/SpeX | HD163296 | 20160907 | 0.7 - 5.3 ($\mu m$) |
| IRTF/SpeX | HD163296 | 20170525 | 0.7 - 5.3 ($\mu m$) |
| IRTF/SpeX | HD163296 | 20170727 | 0.7 - 5.3 ($\mu m$) |
| IRTF/SpeX | HD163296 | 20170814 | 0.7 - 5.3 ($\mu m$) |
| IRTF/SpeX | HD163296 | 20170912 | 0.7 - 5.3 ($\mu m$) |
| IRTF/SpeX | HD163296 | 20180417 | 0.7 - 5.3 ($\mu m$) |
| IRTF/SpeX | HD163296 | 20180811 | 0.7 - 5.3 ($\mu m$) |
| IRTF/SpeX | HD163296 | 20180922 | 0.7 - 5.3 ($\mu m$) |
| APO/Triplespec | HD163296 | 20180408 | 0.95-2.46 ($\mu m$) |
| APO/Triplespec | HD163296 | 20180416 | 0.95-2.46 ($\mu m$) |
| APO/Triplespec | HD163296 | 20180516 | 0.95-2.46 ($\mu m$) |
| VLA | HD163296 | 20180306 | 3.76-5.76, 6.36-8.36 GHz |
| VLA | HD163296 | 20180414 | 3.76-5.76, 6.36-8.36 GHz |
| VLA | HD163296 | 20180515 | 3.76-5.76, 6.36-8.36 GHz |
| VLA | HD163296 | 20180927 | 3.76-5.76, 6.36-8.36 GHz |
| VLA | HD163296 | 20181020 | 3.76-5.76, 6.36-8.36 GHz |
| VLA | HD163296 | 20181103 | 3.76-5.76, 6.36-8.36 GHz |

Table 5.2:: Near-IR and Radio observations.

Table 5.3: VLA Flux

| Epoch | Flux (Jy) | Spectral Index ($\alpha$) |
|---|---|---|
| 2018 March 06 | $2.35 \times 10^{-4} \pm 5.63 \times 10^{-5}$ | $0.817 \pm 0.092$ |
| 2018 April 14 | $1.873 \times 10^{-4} \pm 8.60 \times 10^{-5}$ | $0.715 \pm 0.082$ |
| 2018 May 15 | $2.299 \times 10^{-4} \pm 7.15 \times 10^{-5}$ | $0.708 \pm 0.021$ |
| 2018 September 27 | $3.434 \times 10^{-4} \pm 3.23 \times 10^{-5}$ | $1.0104 \pm 0.0488$ |
| 2018 October 20 | $3.065 \times 10^{-4} \pm 2.61 \times 10^{-5}$ | $1.080 \pm 0.0246$ |
| 2018 November 03 | $3.164 \times 10^{-4} \pm 2.83 \times 10^{-5}$ | $1.219 \pm 0.029$ |

Table 5.4. Near-IR accretion measurements

| HJD | $K_{obs}$ (mag) | EW(Br$\gamma$)$_{obs}$ Å | EW(Br$\gamma$)$_{cs}$ Å | L(Br$\gamma$) ($10^{-3}$ $L_\odot$) | log $M_{acc}$(Br$\gamma$) ($M_\odot$ yr$^{-1}$) |
|---|---|---|---|---|---|
| 2002 Mar. 23 [a] | 4.5 | -3.0 | -7.2 ± 1.2 | 1.8 ± 0.3 | -6.57 ± 0.89 |
| 2002 Jul. 18 [b] | 4.5 | -3.1 | -7.3 ± 1.2 | 1.8 ± 0.3 | -6.56 ± 0.89 |
| 2004 Jun. 09 [c] | 4.8 | -4.7 | -10.2 ± 1.2 | 1.9 ± 0.2 | -6.54 ± 0.89 |
| 2005 Jul. 06 [b] | 4.6 | -4.2 | -8.8 ± 1.2 | 2.0 ± 0.3 | -6.53 ± 0.89 |
| Mar 2008 [d] | 4.8 | -4.3 | -9.8 ± 1.2 | 1.8 ± 0.2 | -6.55 ± 0.89 |
| 2008 May 13 [d] | 4.8 | -4.3 | -9.8 ± 1.2 | 1.8 ± 0.2 | -6.55 ± 0.89 |
| 2009 Jul. 15 [e] | 4.8 | -3.2 | -8.7 ± 1.2 | 1.6 ± 0.2 | -6.60 ± 0.89 |
| 2011 Oct. 12 [f] | 4.8 | -4.2 | -9.7 ± 1.2 | 1.8 ± 0.2 | -6.56 ± 0.89 |
| 2011 Oct. 14 [f] | 4.5 | -3.3 | -7.5 ± 1.2 | 1.8 ± 0.3 | -6.55 ± 0.89 |
| 2011 Oct. 16 [f] | 4.3 | -3.9 | -7.4 ± 1.2 | 2.2 ± 0.4 | -6.49 ± 0.88 |
| 2012 Mar. 24 [f] | 4.3 | -3.7 | -7.2 ± 1.2 | 2.1 ± 0.4 | -6.50 ± 0.89 |
| 2012 May 17 [f] | 4.2 | -3.7 | -6.9 ± 1.2 | 2.2 ± 0.4 | -6.48 ± 0.88 |
| 2012 Jul. 05 [g] | 4.7 | -4.3 | -9.3 ± 1.2 | 1.9 ± 0.2 | -6.54 ± 0.89 |
| 2016 Apr. 04 | 5.07 ± 0.11 | -4.22 | -11.28 ± 1.2 | 1.6 ± 0.2 | -6.59 ± 0.89 |
| 2016 May 04 | 5.11 ± 0.11 | -5.33 | -12.66 ± 1.2 | 1.8 ± 0.2 | -6.56 ± 0.89 |
| 2016 Jun. 09 | 5.05 ± 0.11 | -4.37 | -11.33 ± 1.2 | 1.7 ± 0.2 | -6.59 ± 0.89 |
| 2016 Aug. 10 | 5.0 ± 0.11 | -3.56 | -10.23 ± 1.2 | 1.6 ± 0.2 | -6.61 ± 0.89 |
| 2016 Sep. 07 | 5.14 ± 0.11 | -4.18 | -11.76 ± 1.2 | 1.6 ± 0.2 | -6.6 ± 0.89 |
| 2017 May 25 | 5.13 ± 0.11 | -4.49 | -11.99 ± 1.2 | 1.6 ± 0.2 | -6.59 ± 0.89 |
| 2017 Sep. 12 | 4.96 ± 0.11 | -4.21 | -10.63 ± 1.2 | 1.7 ± 0.2 | -6.58 ± 0.89 |
| 2018 Apr. 08 | 4.94 ± 0.11 | -5.76 | -12.04 ± 1.2 | 2.0 ± 0.2 | -6.52 ± 0.89 |
| 2018 Apr. 16 | 5.01 ± 0.11 | -5.23 | -11.91 ± 1.2 | 1.8 ± 0.2 | -6.55 ± 0.89 |
| 2018 May 16 | 4.76 ± 0.11 | -3.97 | -9.31 ± 1.2 | 1.8 ± 0.2 | -6.56 ± 0.89 |
| 2018 June 24 | 4.77 ± 0.11 | -5.17 | -10.54 ± 1.2 | 2.0 ± 0.2 | -6.51 ± 0.89 |
| 2018 Aug. 11 | 4.95 ± 0.11 | -3.35 | -9.69 ± 1.2 | 1.6 ± 0.2 | -6.61 ± 0.89 |

Table 5.4—Continued

| HJD | $K_{obs}$ (mag) | EW(Br$\gamma$)$_{obs}$ Å | EW(Br$\gamma$)$_{cs}$ Å | L(Br$\gamma$) ($10^{-3}$ $L_\odot$) | log $M_{acc}$(Br$\gamma$) ($M_\odot$ yr$^{-1}$) |
|---|---|---|---|---|---|
| 2018 Sep. 22 | 4.85 ± 0.11 | -4.58 | -10.37 ± 1.2 | 1.8 ± 0.2 | -6.55 ± 0.89 |

Note. — Near-IR accretion measurements using Br$\gamma$.
Original magnitude and equivalent width measurements was taken from *a*: Brittain et al. 2007, *b*: Sitko et al. 2008, *c*: Garcia Lopez et al. 2006, *d*: Donehew & Brittain 2011, *e*: Mendigutía et al. 2013, *f*: Ellerbroek et al. 2014.
The accretion values originally previously presented by Ellerbroek et al. (2014) were recalculated above to include updated distance and radius values for HD 163296.

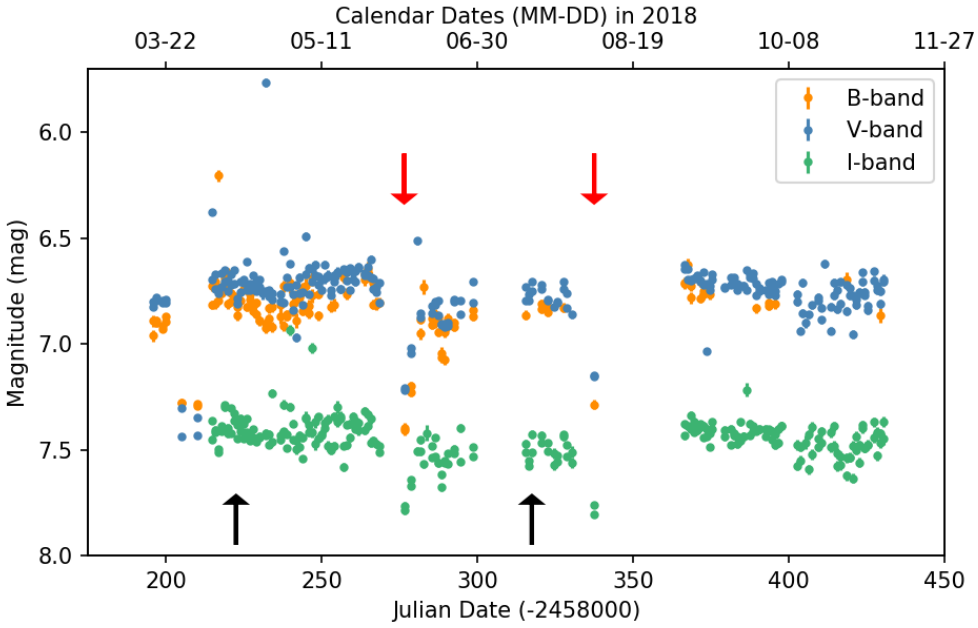


Fig. 5.1.— Optical light curve for HD 163296 in 2018 in B-,V-, and I-, bands. The two black arrows note when the 2018 Apr. and 2018 Jul. HST/STIS epochs were taken. We note two potential dipper events around 2018 Jun. 7th and 2018 Aug. 7th which are identified in the light curve by the downward pointing red arrows.

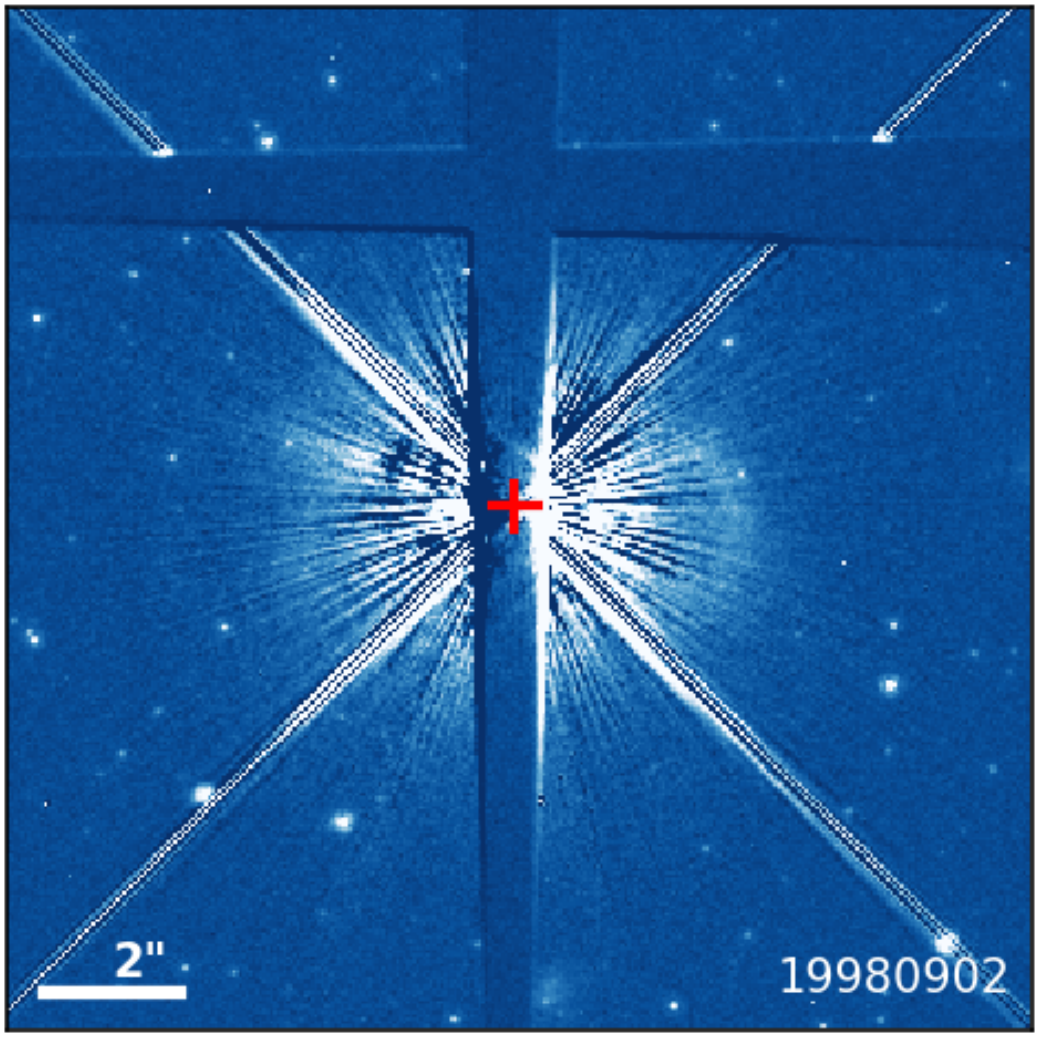


Fig. 5.2.— PSF subtracted image examples from the 1998 Sep. 02 with the A1.0 Wedge. The images are all in the detector frame and are unmasked showing the wedges and the spider arms. A red '+' sign marks the location of the central star utilizing the 'x' marks the spot methodology. The field of view of the figure is $15\farcs2 \times 15\farcs2$.

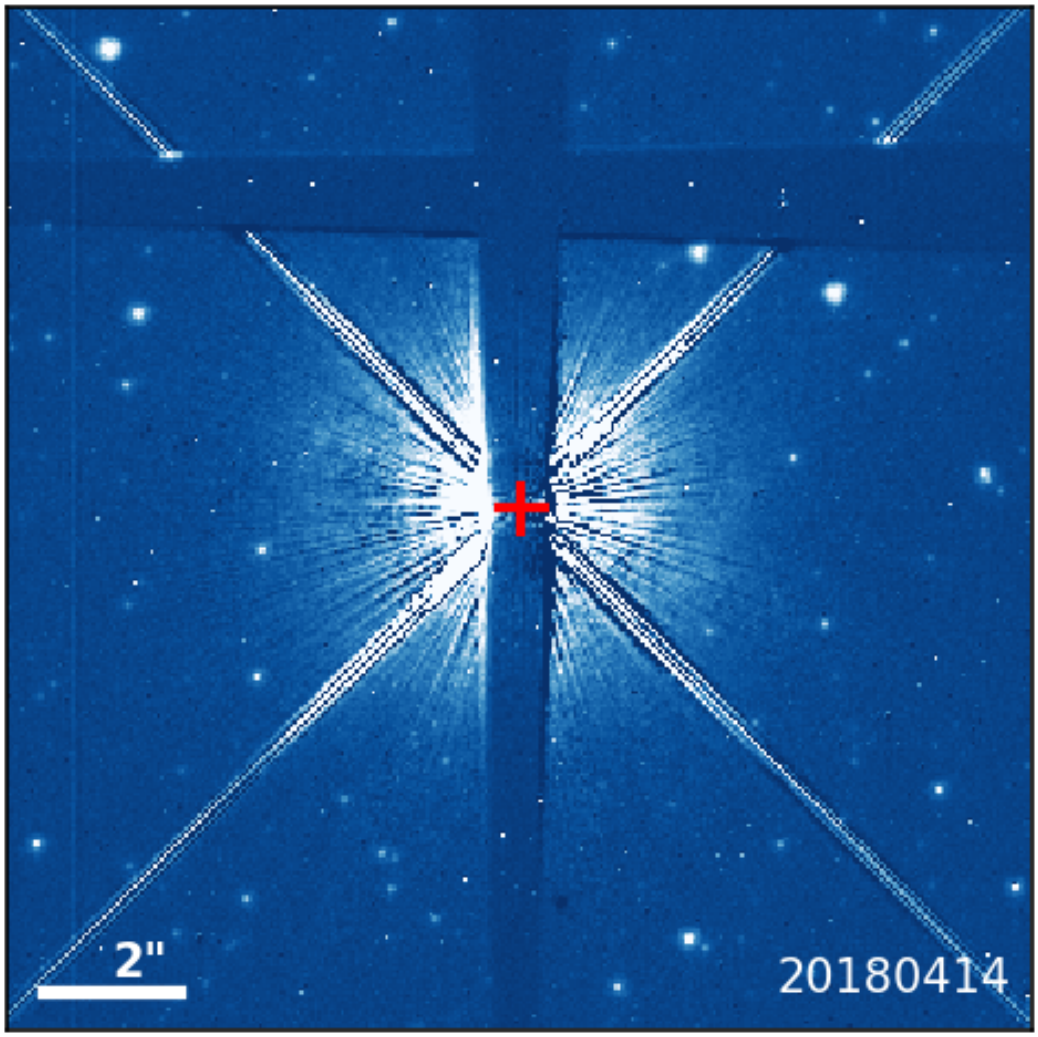


Fig. 5.3.— PSF subtracted image examples from the 2018 Apr. 14 with the A1.0 Wedge. The images are all in the detector frame and are unmasked showing the wedges and the spider arms. A red '+' sign marks the location of the central star utilizing the 'x' marks the spot methodology. The field of view of the figure is $15\farcs2 \times 15\farcs2$.

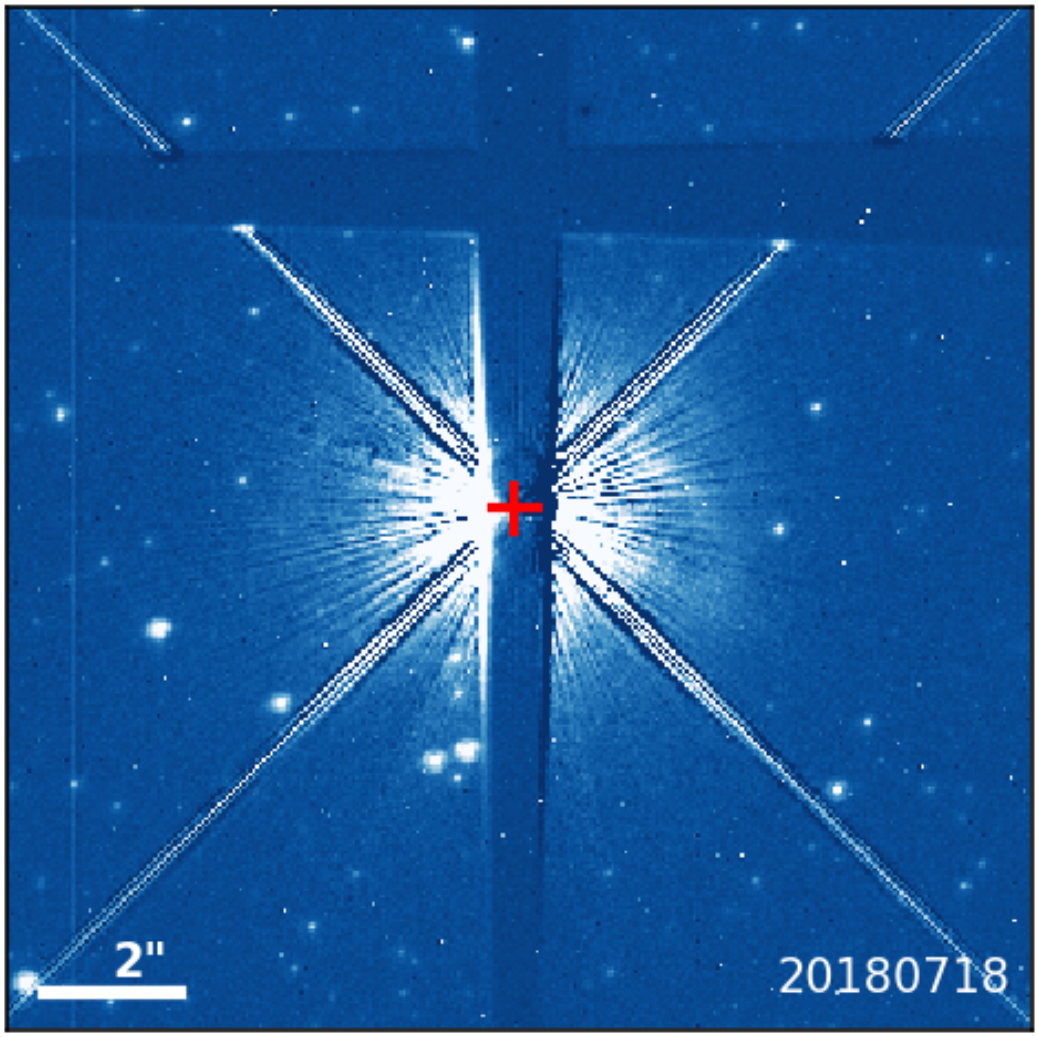


Fig. 5.4.— PSF subtracted image examples from the 2018 Jul. 18 with the A1.0 Wedge. The images are all in the detector frame and are unmasked showing the wedges and the spider arms. A red '+' sign marks the location of the central star utilizing the 'x' marks the spot methodology. The field of view of the figure is $15\farcs2 \times 15\farcs2$.

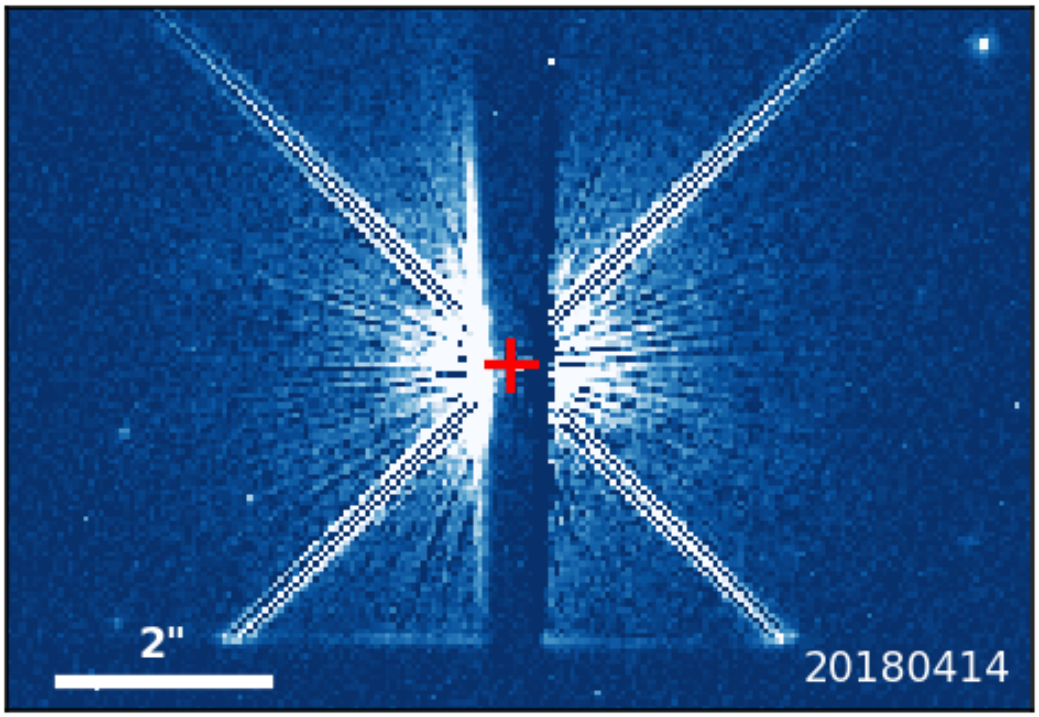


Fig. 5.5.— PSF subtracted image examples from the 2018 Apr. 18 with the A0.6 Wedge. The images are all in the detector frame and are unmasked showing the wedges and the spider arms. A red '+' sign marks the location of the central star utilizing the 'x' marks the spot methodology. The field of view of this image is $10\farcs1 \times 7\farcs0$.

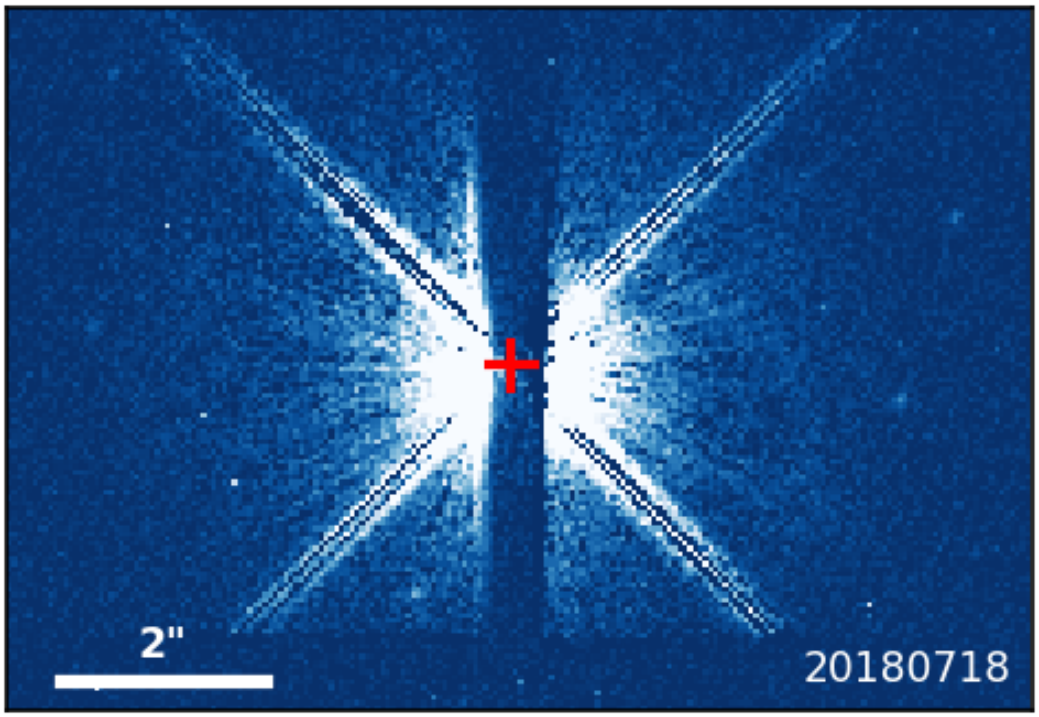


Fig. 5.6.— PSF subtracted image examples from the 2018 Jul. 18 with the A0.6 Wedge. The images are all in the detector frame and are unmasked showing the wedges and the spider arms. A red '+' sign marks the location of the central star utilizing the 'x' marks the spot methodology. The field of view of this image is $10\farcs1 \times 7\farcs0$.

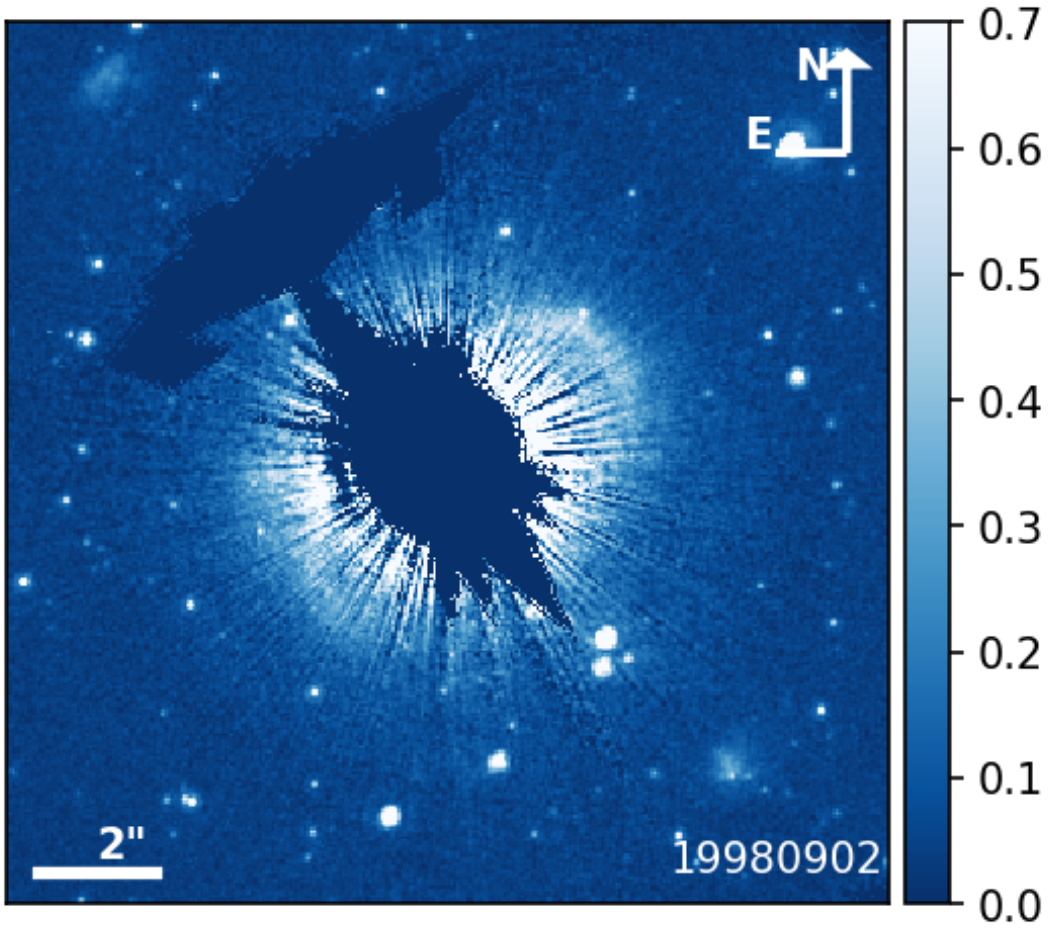


Fig. 5.7.— Combined images of the three epochs epochs from 19980902 (left), 20180414 (middle), and 20180718 (right) with the A1.0 Wedge. The white regions are masked out where the wedge was located. The images are plotted linearly. The field of view of the figure is $15\farcs2 \times 15\farcs2$.

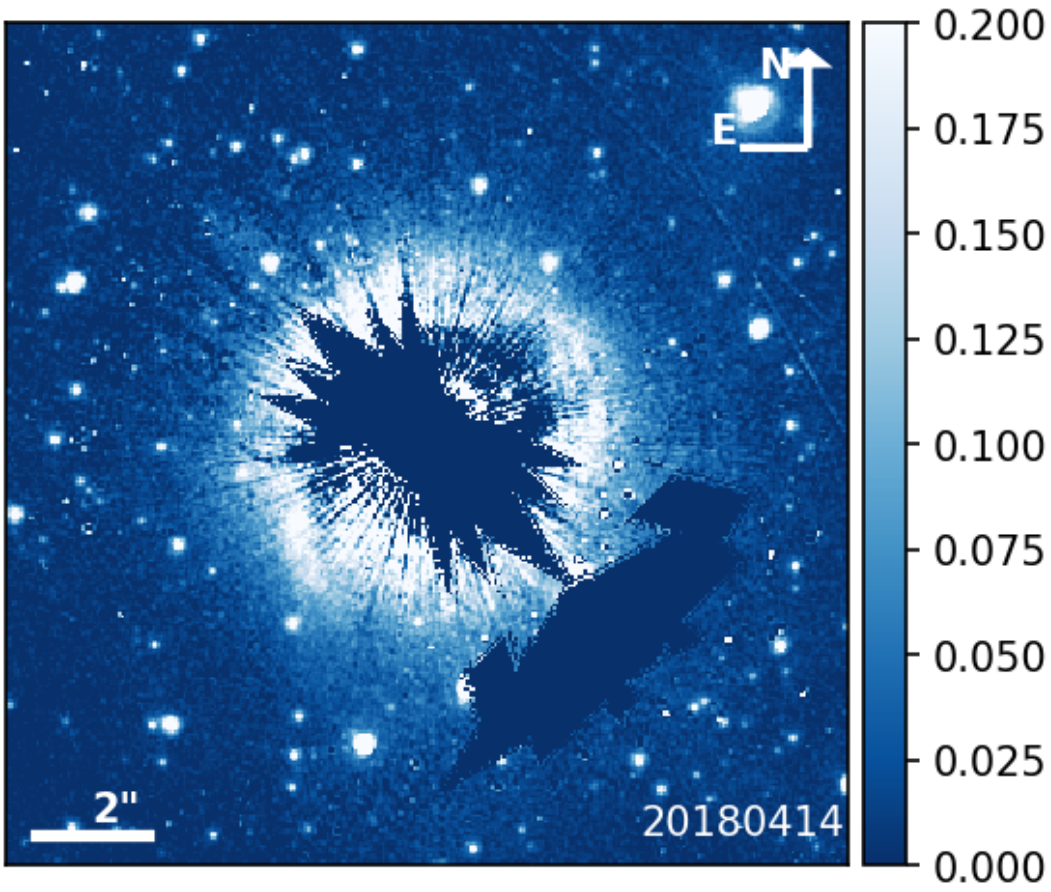


Fig. 5.8.— Combined images of the three epochs epochs from 19980902 (left), 20180414 (middle), and 20180718 (right) with the A1.0 Wedge. The white regions are masked out where the wedge was located. The images are plotted linearly. The field of view of the figure is 15.″2 × 15.″2.

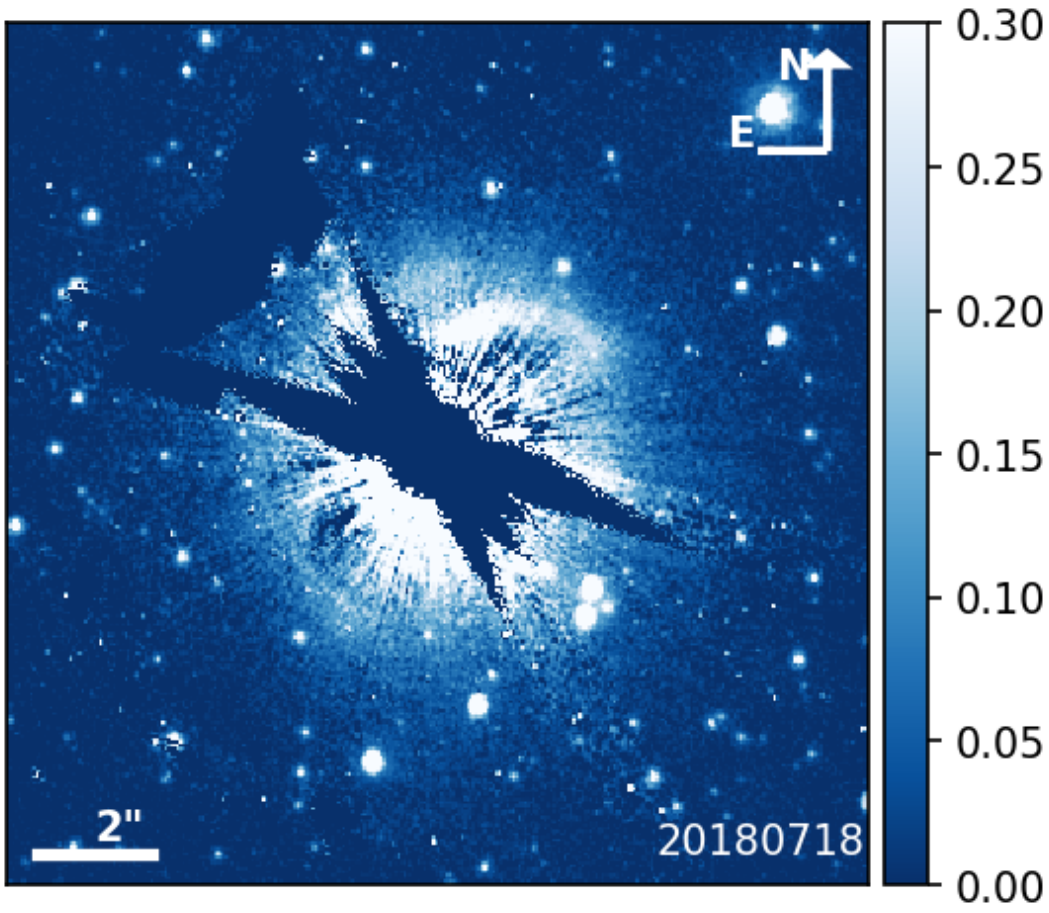


Fig. 5.9.— Combined images of the three epochs epochs from 19980902 (left), 20180414 (middle), and 20180718 (right) with the A1.0 Wedge. The white regions are masked out where the wedge was located. The images are plotted linearly. The field of view of the figure is $15\farcs2 \times 15\farcs2$.

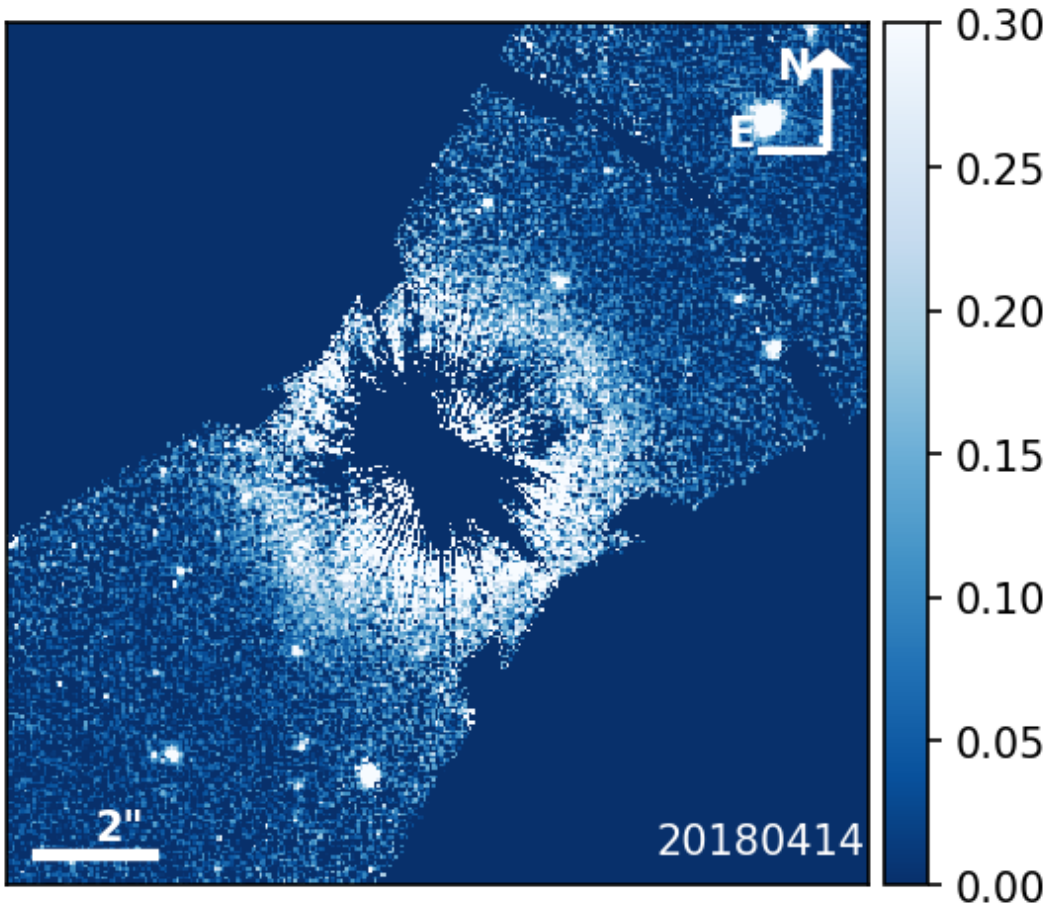


Fig. 5.10.— Combined images of the two epochs epochs from 20180414 (left), and 20180718 (right) with the A0.6 Wedge. The white regions are masked out where the wedge was located or where the image was not readout with the CCD. The images are plotted linearly. The field of view of the figure is $15\farcs2 \times 15\farcs2$.

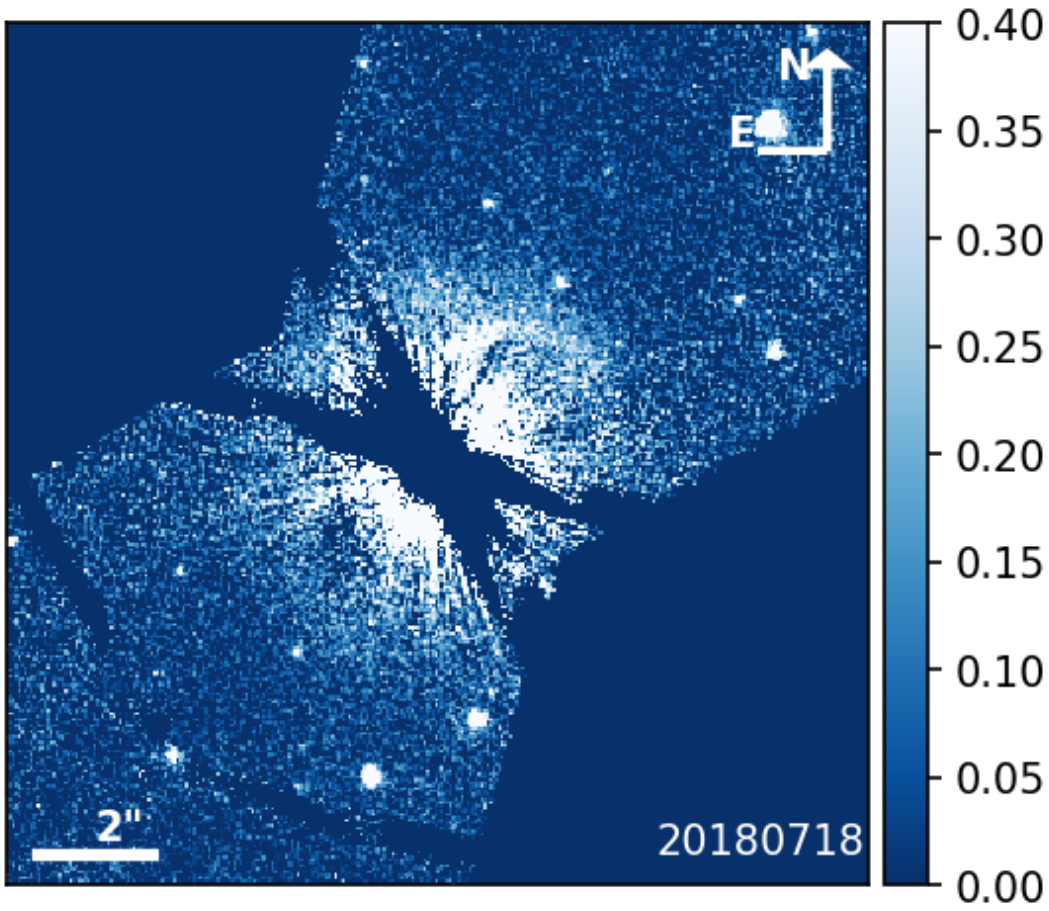


Fig. 5.11.— Combined images of the two epochs epochs from 20180414 (left), and 20180718 (right) with the A0.6 Wedge. The white regions are masked out where the wedge was located or where the image was not readout with the CCD. The images are plotted linearly. The field of view of the figure is $15\farcs2 \times 15\farcs2$.

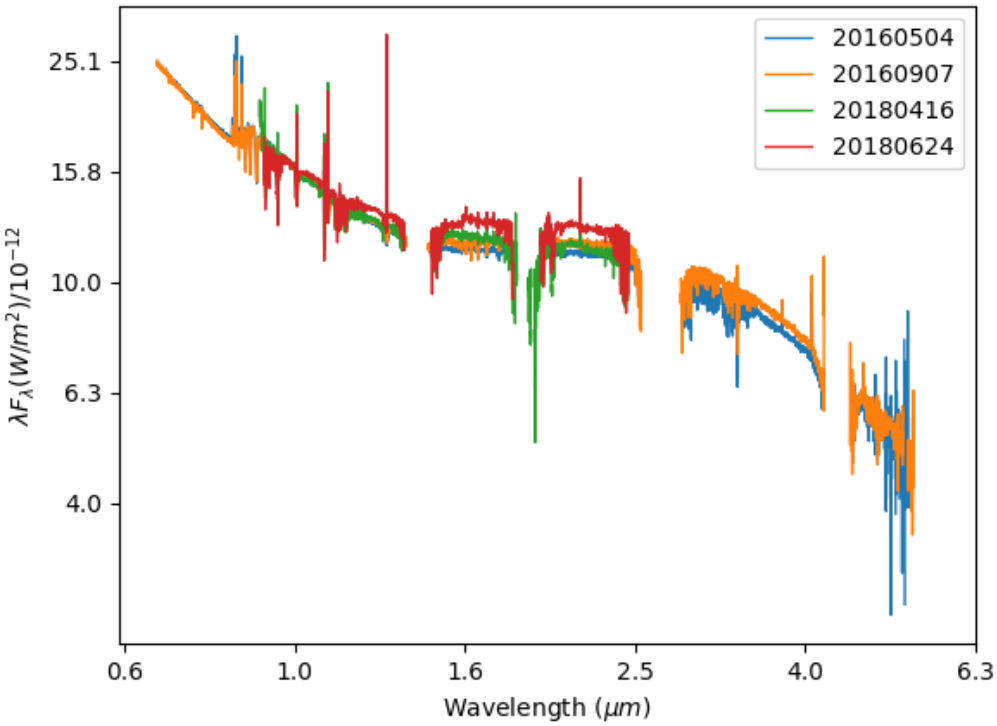


Fig. 5.12.— 4 epochs of flux calibrated near-IR spectra taken with IRTF/SpeX and APO/Triplespec are plotted in this figure. Note that epoch 20180624 is the highest near-IR flux we observed and 20160504 is the lowest near-IR flux we observed between 2016 and 2018.

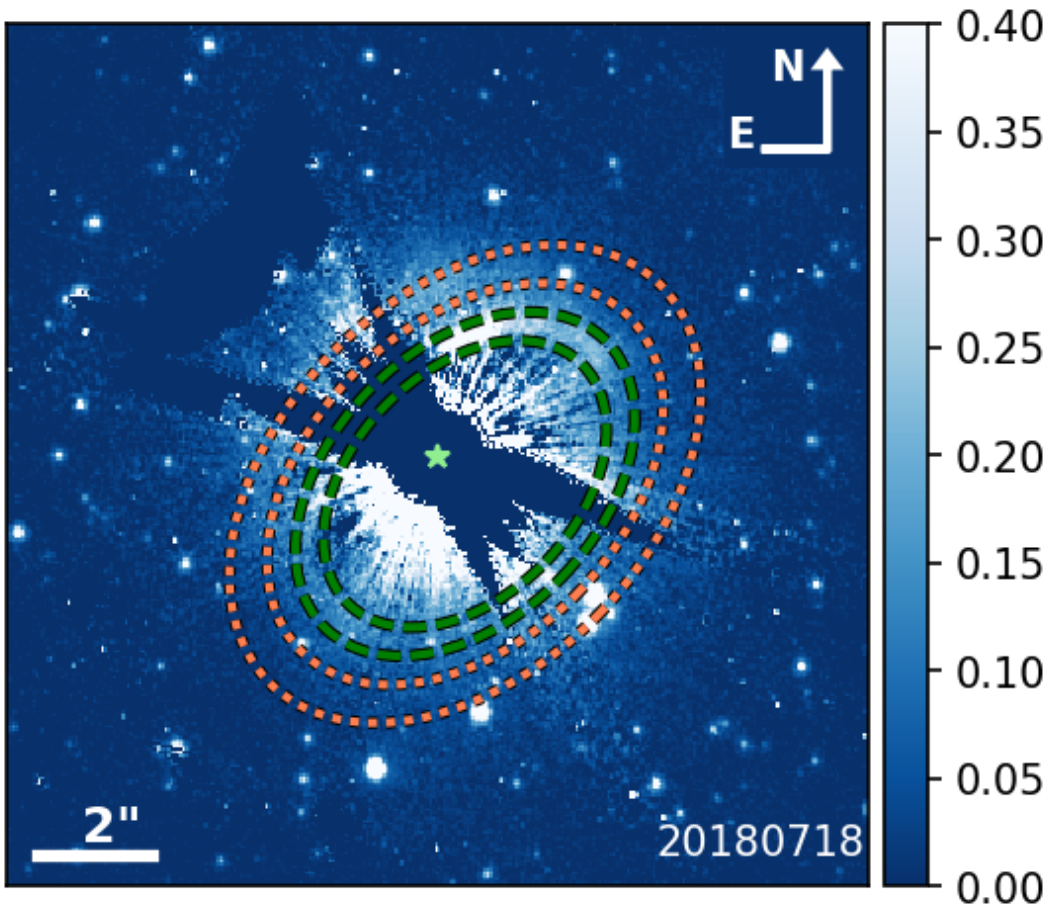


Fig. 5.13.— The 2018 Jul. epoch image with the two disk regions (ansae and peripheral) outlined by ellipses. The ansae region is outlined by the two dashed green ellipses located at 300 and 360 au. The surface brightness of the ansae region is plotted in Figures 5.15 and 5.16. The peripheral region (disk excess) is outlined by the two dotted orange ellipses located at 420 and 500 au. The surface brightness of the disk excess region is plotted in Figures 5.17 and 5.18. We assumed a disk inclination of 42°, a disk PA of 132 ° (Isella et al., 2016), and a disk minor axis offset of 0.″7 . The green star labels the location of the central star. The field of view of the figure is 15.″2 × 15.″2.

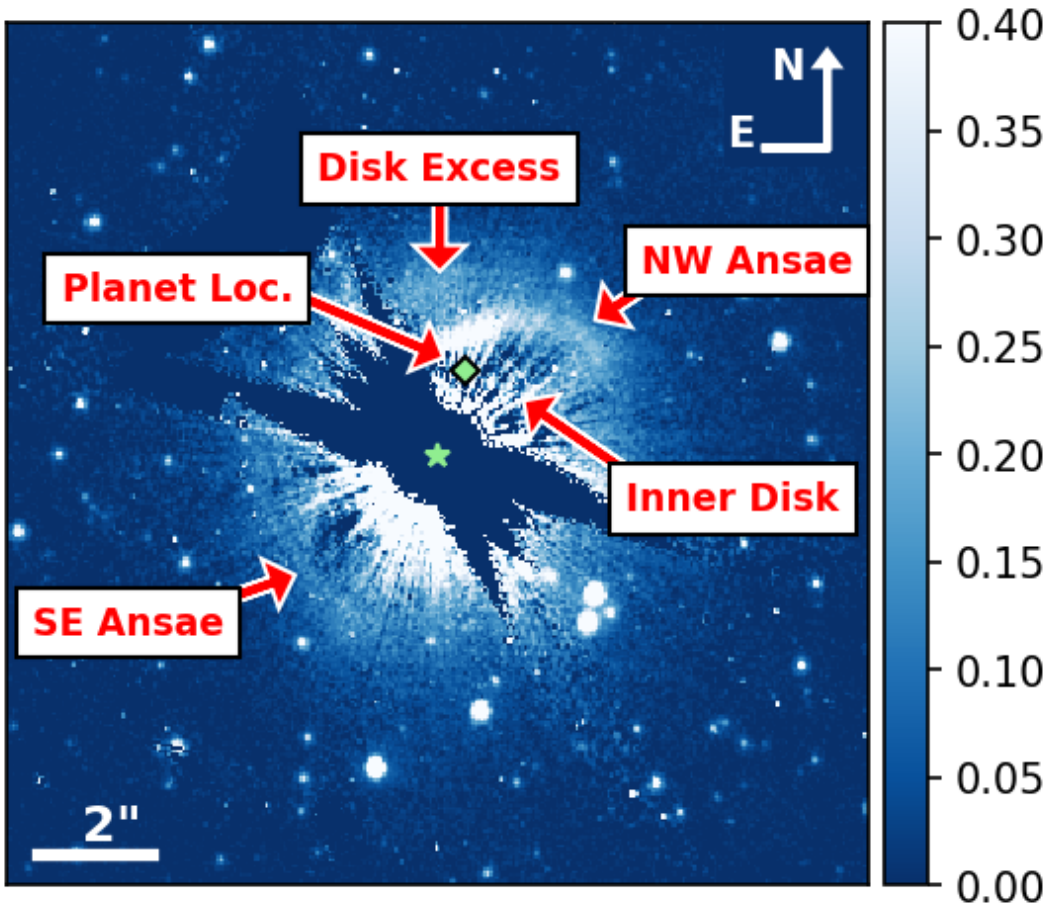


Fig. 5.14.— The 2018 Jul. epoch image with the 1.0A wedge where the the NW Ansa, SE Ansa, disk excess, inner disk, central star location (green star) and the approximate location of Pinte et al. (2018) planet candidate (green diamond) are located. The field of view of the figure is $15\farcs2 \times 15\farcs2$.

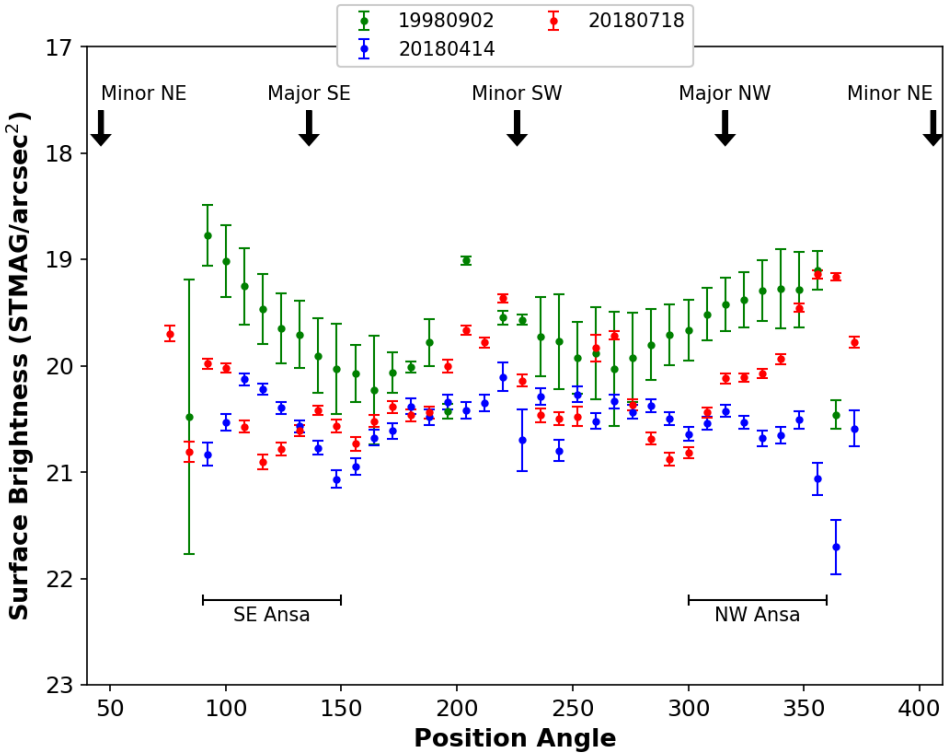


Fig. 5.15.— Surface brightness of the ansae (3rd ring) region of the disk of the wedge 1.0A images (Figures 5.7, 5.8, 5.9). The surface brightness is binned azimuthally with each bin being 132° wide in the azimuthal angle and 2.″96 - 3.″55 (300 - 360 au) in the radial direction. We assumed that the disk ring is circular and thus assumed inclination of 42° and PA of 132° from (Isella et al., 2016). See Figure 5.13 which overlays the annulus region onto the image of the disk. The error bars are $3\sigma$.

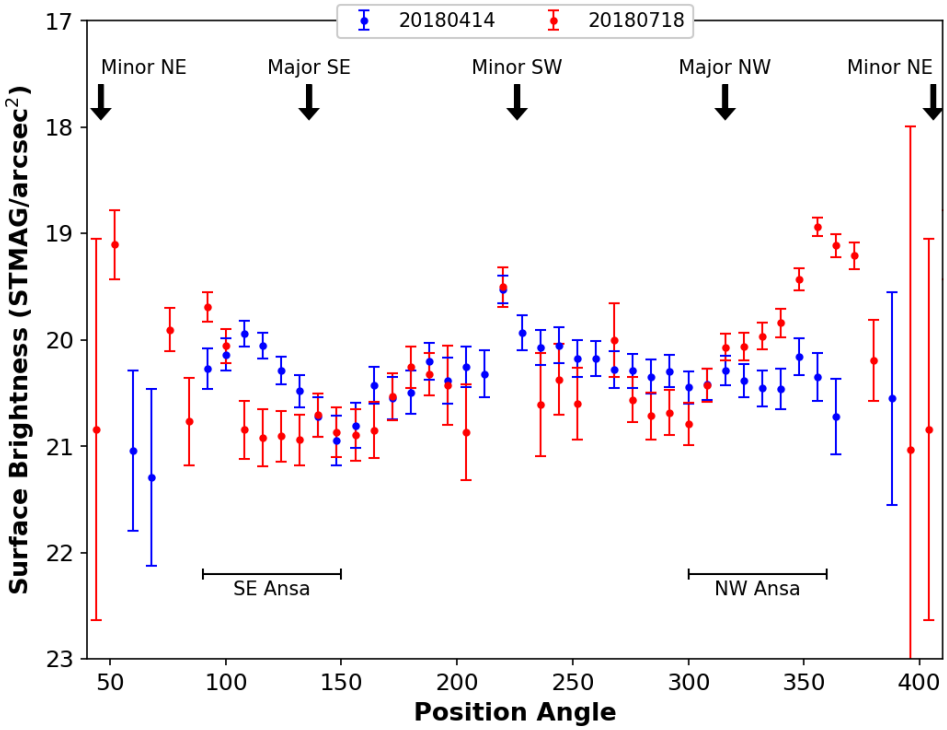


Fig. 5.16.— Surface brightness of the ansae (3rd ring) region of the disk of the wedge 1.0A images (Figures 5.10, 5.11). The surface brightness is binned azimuthally with each bin being 132° wide in the azimuthal angle and 2.″96 - 3.″55 (300 - 360 au) in the radial direction. We assumed that the disk ring is circular and thus assumed inclination of 42° and PA of 132° from (Isella et al., 2016). See Figure 5.13 which overlays the annulus region onto the image of the disk. The error bars are $3\sigma$.

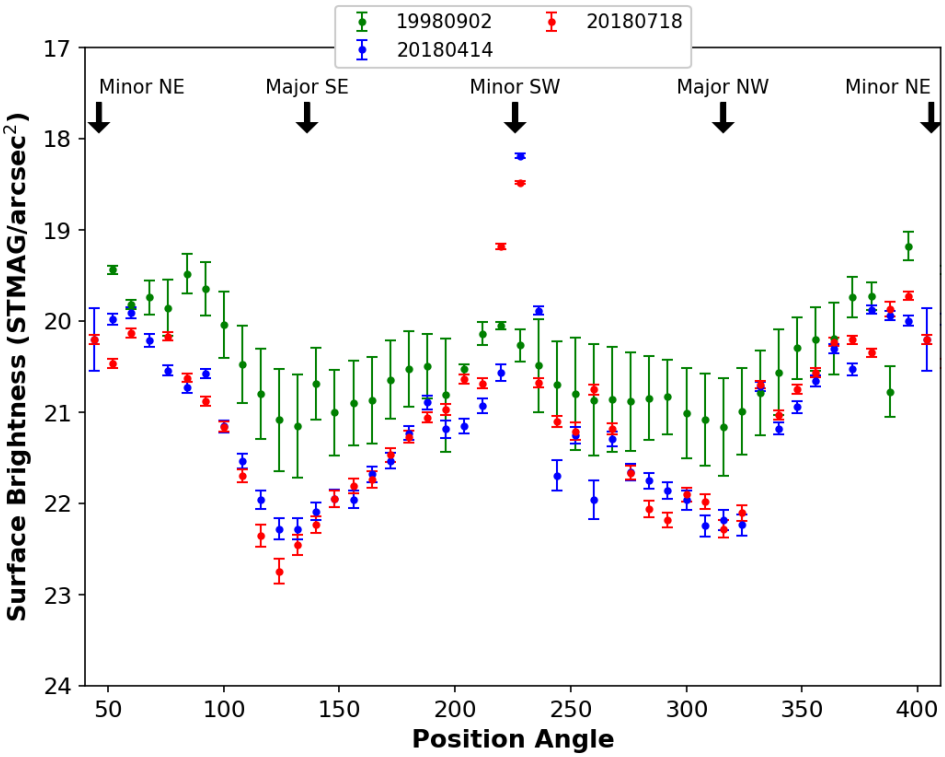


Fig. 5.17.— Surface brightness of the disk for two projected radii plotted azimuthally. We assumed that the disk ring is circular and thus assumed inclination of 42° and PA of 132° from (Isella et al., 2016). The colored regions are the $3\sigma$ error bars. The solid black line is the $3\sigma$ background flux. The red points are from a projected radius from 300 - 360 AU which traces the broken ring feature first identified by Grady et al. (2000). The green points are from a projected radius of 420 - 500 AU and trace the excess flux detected on each side of the NW minor axis. Note that all three epochs have different total exposures leading to different background surface brightness levels.

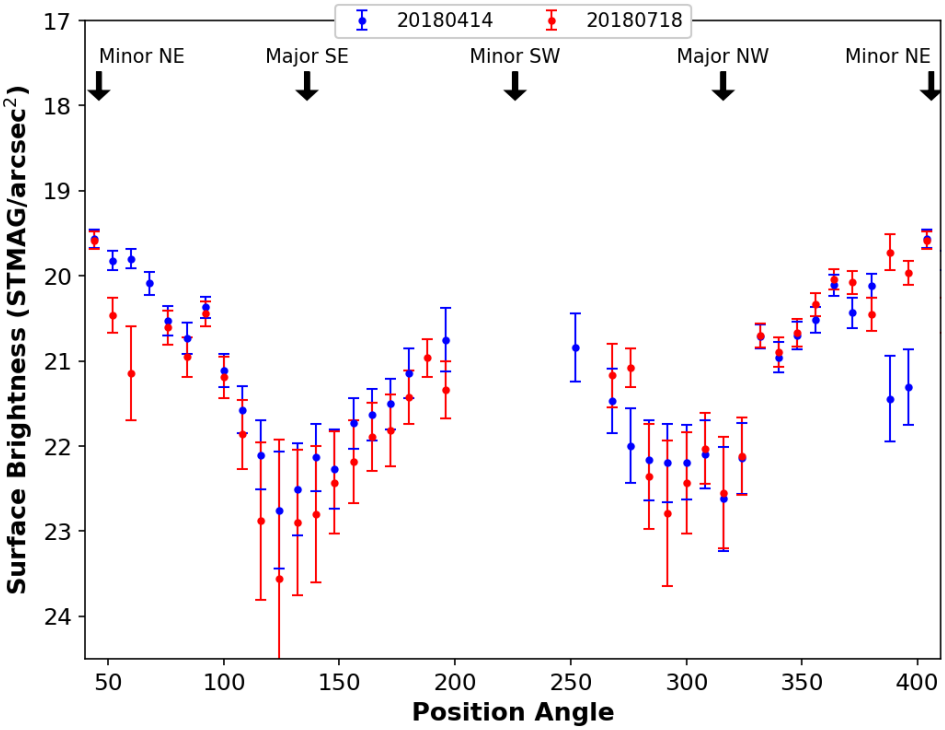


Fig. 5.18.— Surface brightness of the disk for two projected radii plotted azimuthally. We assumed that the disk ring is circular and thus assumed inclination of 42° and PA of 132° from (Isella et al., 2016). The colored regions are the $3\sigma$ error bars. The solid black line is the $3\sigma$ background flux. The red points are from a projected radius from 300 - 360 AU which traces the broken ring feature first identified by Grady et al. (2000). The green points are from a projected radius of 420 - 500 AU and trace the excess flux detected on each side of the NW minor axis. Note that all three epochs have different total exposures leading to different background surface brightness levels.

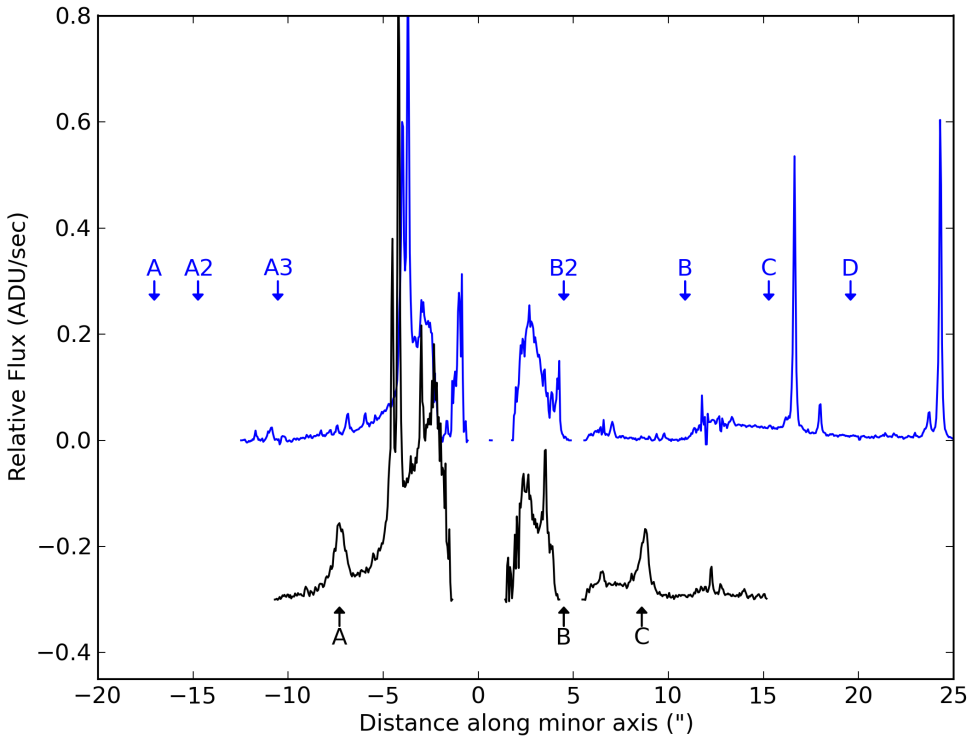


Fig. 5.19.— Crosscut along the minor axis from the epochs in 1998 Sep. (black) and 2018 Jul. (blue). The HH knot locations are provided for the measured location in the 1998 Sep. epoch and the projected location in 2018 summer from Ellerbroek et al. (2014). While we observe clear evidence of two HH-knots in the 19980902 epoch, but do not see any of the 5 HH-knots predicted to be observed in the 2018 Jul. epoch. The large thin spikes located around HH-knots C and D are background stars.

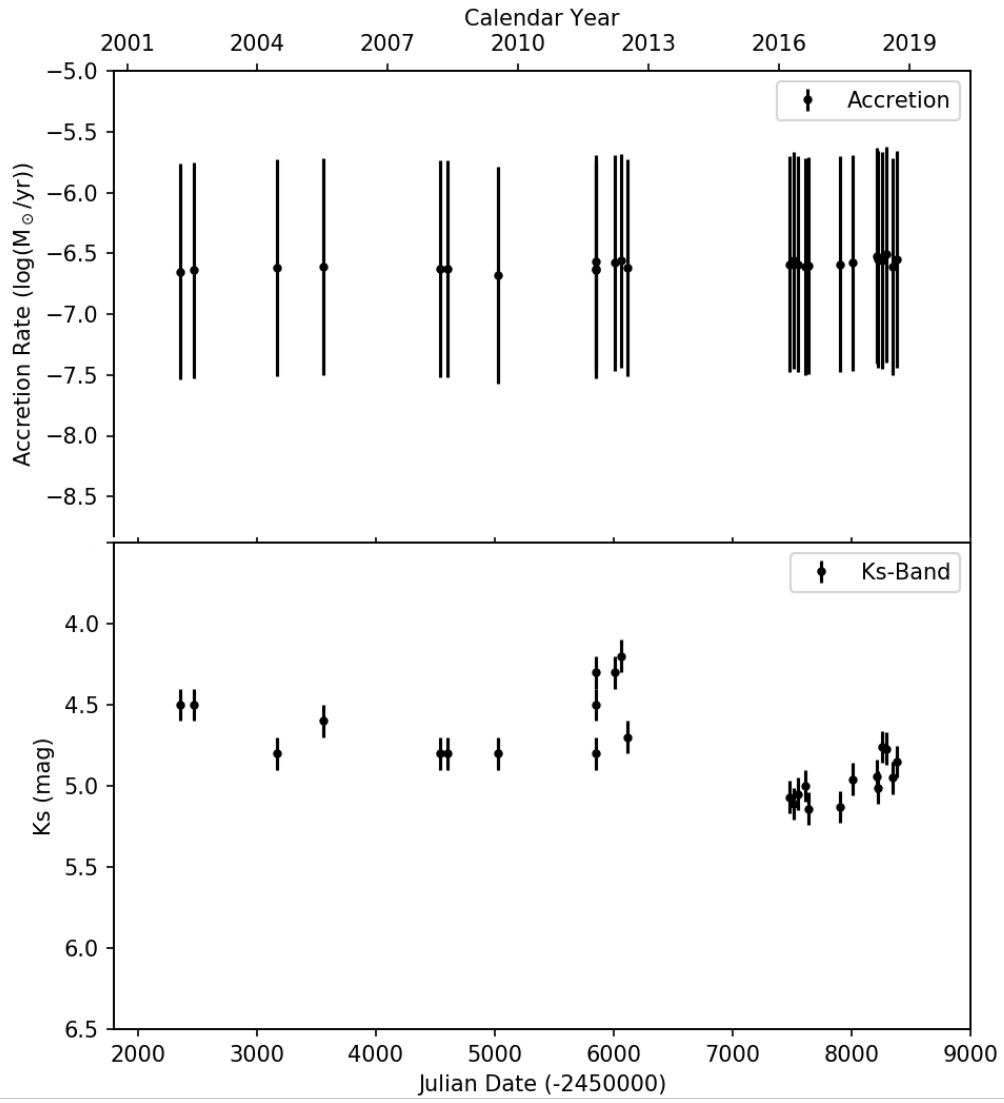


Fig. 5.20.— Top panel shows the accretion rate for HD 163296 measured with the Br$\gamma$ line. Accretion rates before 2013 were originally presented by Ellerbroek et al. (2014) and were recalculated by this work to incorporate new distance and $R_{\odot}$values. The bottom panel shows the lightcurve in the Ks-band. Ks-band magnitudes before 2013 were taken from Ellerbroek et al. (2014) (see Table 5.4).

# Chapter 6

# Conclusion

## 6.1 Chapter Summaries

In Chapter 2, we presented the first spatially resolved near-IR scattered light observation of DoAr 28 transitional disk. We detected the scattered light disk from 0.″10 (13 AU) out to 0.″50 (65 AU), which is slightly interior to the location of the system's gap inferred by another group's SED modeling (15 AU). Although we detected a point source companion 1.″1 northwest of the system, our second epoch of imagery of the system found that the proper motion point source is consistent with a background star. We modeled the observed SED and H-band PI imagery of the system using the HOCHUNK3D Monte Carlo Radiative Transfer code. We found that our best fit model has an inclined disk of 50° and 0.01 M$\odot$ disk. Additionally, we find a best fit inner gap of $\sim$8 au. These results of the transitional disk around DoAr 28 help contribute to the plethora of information still being learned about transitional disks. Follow-up imaging of DoAr 28 with higher contrast and higher inner working angle scattered light imagers (eg. VLT/SPHERE, Subaru/SCExAO) could help further investigate the non-azimuthal asymmetries we observed. Finally, sub-mm observations with ALMA will help trace the large grain dust distribution to see if its distribution matches with our observations of the small dust grain population.

In Chapter 3 we presented Subaru/IRCS $L'$and $M'$ of the nearby M dwarf VHS J125601.92-125723.9 (VHS 1256), which was recently claimed to have a $\sim$11 $M_J$ companion (VHS 1256 b) at $\sim$102 au separation. We find that our adaptive optics images partially resolve the central M dwarf star as a binary. We find

that the components are nearly equal in brightness and separated by $0\farcs106 \pm 0\farcs001$. Combined with the previous non-detection of lithium in the primary, we estimate that the system is at least older than 200 Myr and the masses of the stars comprising the central binary are at least 58 $M_J$ each. Moreover, we find some of the properties of VHS 1256 are inconsistent with the recent suggestion that it is a member of the AB Dor moving group. Given the possible ranges in distance (12.7 *pc* vs. 17.1 *pc*), the lower mass limit for VHS 1256 b ranges from 10.5 $M_J$ to 26.2 $M_J$. VHS 1256 is most likely a very low mass (VLM) hierarchical triple system, and could be the third such system in which all components reside in the brown dwarf mass regime.

In Chapter 4, we presented H-band scattered light observation of HD 163296 and contemporaneous infrared spectra observations. Our 2011 H-band scattered light imagery resolved a broken ring structure surrounding HD 163296 that peaks at a distance along the major axis of $0\farcs65$ (66 au) and extended out to $0\farcs98$ (100 AU) along the major axis. Our 2011-epoch H-band imagery exhibited clear axisymmetry, with the NW- and SE-side of the disk exhibiting similar intensities. Our 2011 epoch H-band data are thus clearly different than the 2016 epoch H-band data from VLT/SPHERE reported by Muro-Arena et al. (2018), that exhibit a strong 2.7x asymmetry between the NW- and SE-side of the disk. These results indicate the presence of time variable, non-azimuthally symmetric illumination of the outer disk. We modeled the contemporaneous near-IR spectra and spatially resolved H-band scattered light imagery of HD 163296 with a 3D MCRT code HOCHUNK3D. We found that our data can be reproduced with a model that approximated the features of a disk wind via an envelope and did not specifically require an inclined inner disk component. We speculated that a variable, non-axisymmetric distribution of dust clouds elevated by a disk wind could produce

the diversity of morphological appearances of the outer disk now reported in the literature for this system. Finally, our 2018 epoch SCExAO/CHARIS observations easily recovered the disk but they fail to recover the candidate 6–7 $M_{\rm J}$ protoplanet identified from Keck/NIRC2 data (Guidi et al., 2018).

Finally, in Chapter 5 we reported two new HST/STIS coronagraphic imaging epochs taken of HD 163296 and photometric and spectroscopic multiwavelength monitoring campaign of HD 163296 from 2016 to 2018. Additionally, we presented reprocessed archival HST/STIS coronagraphic imaging epoch taken in 1999 Sep. and recalculate accretion measurements from the Br$\gamma$ line taken from 2002-2013. We found that the observed disk flux illumination variability between all three of the HST/STIS epochs with the shortest disk illumination variations now can occur in HD 163296 in $< 3$ months. We did not detect the launch of any new HH-knots in optical, near-IR, or radio bandpasses, that were predicted to launch 2018 (Ellerbroek et al., 2014). Additionally, we did not detect any of the previously launched HH-knots in the HST/STIS epochs in 2018 Apr. and 2018 Jul. suggesting a change in the HH-knot flux from previous observations. Finally, the predicted Pinte et al. (2018) planet is projected to be located within the gap between the second and third rings. This is possibly further evidence of the 2 $M_{jup}$ mass planets existence. It remains difficult to directly image expolanets within the gaps of protoplanetary disks. As detector capabilities improve, HD 163296 remains a prime candidate for future planet imaging. Finally, the plethora of disk illumination variability that HD 163296 has exhibited along with its "dipper" events has been observed by a small subset of other protoplanetary disks (eg. RX J1604.3-2130; Pinilla et al. (2018). Further investigations of these types of disks is necessary as it will help constrain the mechanisms at play within the inner disks of these protoplanetary disks.

## 6.2 Future Work: Investigating Variable Illuminated Disks

Several variably illuminated protoplanetary disks have been observed within the last few years (eg. RX J1604.3-2130; Pinilla et al. (2018), TW Hya; Debes et al. 2017, HD 163296; Rich et al. 2019), yet we do not fully understand the mechanisms that are causing these shadowing events. In order to start answering these questions, the YSOVAR project (Morales-Calderón et al., 2011) utilized high cadence optical and mid-IR observations of YSO's searching for flux variability. Cody et al. (2014) found stars in cluster NGC 2264 that exhibited optical "dippers" in their time-series photometry, where the continuous flux dips significantly for 1-5 days. These same dippers could also shadow the outer disk as well. Unfortunately, to fully understand the mechanisms causing the dippers, several degeneracies need to be broken such as: inclination of the disk, variability mechanism amplitudes, disk flux, and disk geometry (inner wall radius, flaring, gaps). Direct imaging observations of nearby YSO's can help break many of these degeneracies and allow for investigation into the mechanisms causing shadowing.

To break the degeneracies and fully identify the mechanisms involved with shadowing of the outer disk, a comprehensive campaign is needed to identify nearby YSOs that exhibit dipper behavior. Only a handful of protoplanetary disks are known to have shadowing of the outer disk, thus we must first identify new candidates. By identifying YSO's that exhibit dipper behavior first, we can create a target list to follow up with direct scattered light observations. The recent Gaia data release 2 allows us to identify objects of interest that are close by ($< 200$ pc), and the TESS mission allows us to look for dipper stars in its 30 minutes survey frames. Figure 6.1 shows different types of stars hosing protoplanetary disks that are in the TESS southern field of view. I estimate that there could be 190 dipper objects in the southern TESS field alone. The final target list will include 10-20

objects, selected based on their distance from earth, their compatibility for direct imaging, and the number of dippers that were observed.

Once the 10-20 target objects have been identified, we can begin comprehensive direct imaging observations of the disks with contemporaneous optical or near-IR photometry. We can directly image the outer disks of the variable shadowed YSO targets with a plethora of instruments. Currently, telescopes and instruments that are available for these types of observations are Gemini/GPI, Subaru/SCExAO, VLT/SPHERE, and VLT/NACO instruments. We will analyze the direct imaging of our YSO targets to constrain the shadowing mechanisms. The direct imaging observations will help constrain the geometry of the disk (eg. gaps, walls, inclination). Finally, we want to investigate if the shadowing varies on any Keplarian timescales, which would be highly suggestive of the shadowing mechanisms being driven by a companion within the disk.

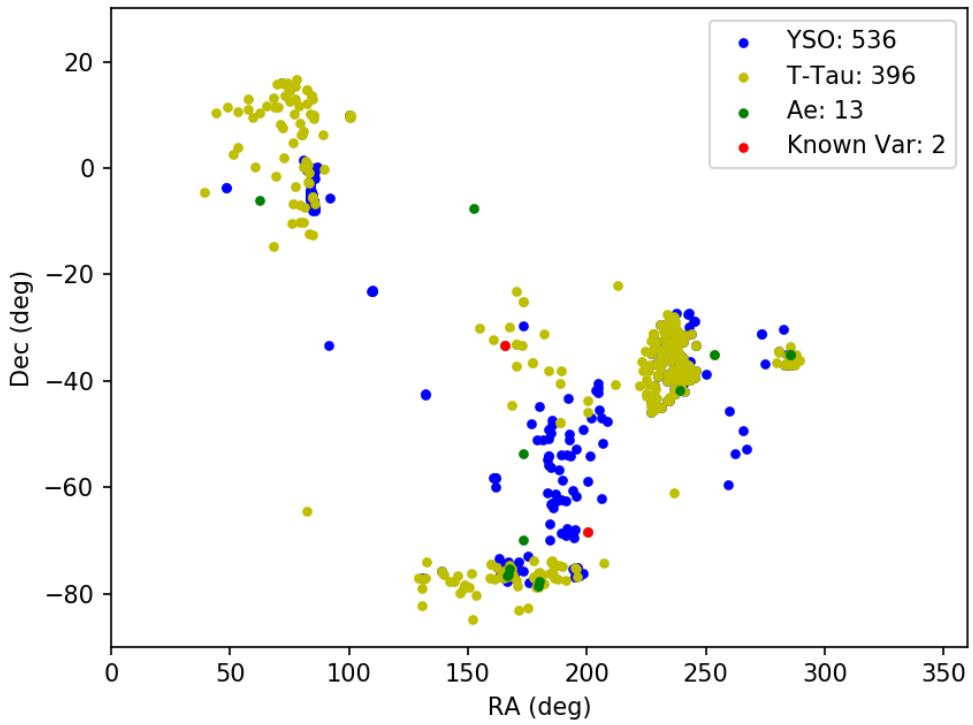


Fig. 6.1.— This figure shows the YSO, T-Tauri (T-Tau), and Herbig Ae (Ae) stars that are visible in the TESS southern field.

# References


Allard, F., Homeier, D., & Freytag, B. 2011, 16th Cambridge Workshop on Cool Stars, Stellar Systems, and the Sun, 448, 91

Allard, F. 2014 in Exploring the Formation and Evolution of Planetary Systems, IAU Proc. 299, 271

Andrews, S. M., & Williams, J. P. 2007, ApJ, 671, 1800

Andrews, S. M., Rosenfeld, K. A., Wilner, D. J., & Bremer, M. 2011, ApJ, 742, L5

Andrews, S. M., Wilner, D. J., Zhu, Z., et al. 2016, ApJ, 820, L40

Anthes Rich, E., Wisniewski, J. P., Hashimoto, J., et al. 2015, AAS/Division for Extreme Solar Systems Abstracts, 3, 117.10

Armstrong, D.J., Osborn, H.P., Brown, D.J.A., Faedi, F., Gomez Maqueo Chew, Y., Martin, D.V., Pollacco, D., & Udry, S. 2014, MNRAS, 444, 1873

Avenhaus, H., Quanz, S., Schmid, H., Meyer, M., Garufi, A., Wolf, S., & Dominik, C. 2014 ApJ, 781, 87

Bailey, V., Meshket, T., Reiter, M. et al. 2014, ApJL, 780, 4

Bally, J. 2016, ARAA, 54, 491

Baraffe, I., Chabrier, G., Barman, T. S., et al., 2003, A&A, 402, 701

Bate, M. R., Bonnell, I. A., & Bromm, V. 2003, MNRAS, 339, 577

Bate, M. R. 2009, MNRAS, 392, 590

Bate, M. R. 2009, MNRAS, 392, 590

Bell, C.P.M., Mamajek, E.E., & Naylor, T. 2015, MNRAS, 454, 593

Berardo, D., Cumminng, A., Marleau, G.-D., 2017, ApJ, 834, 149

Beuzit, J.-L., Feldt, M., Dohlen, K., et al. 2008, Proc. SPIE, 7014, 701418

Biller, B. A., Liu, M. C., Wahhaj, Z., et al. 2013, ApJ, 777, 160

Birnstiel, T., Andrews, S. M., & Ercolano, B. 2012, A&A, 544, A79

Bonnefoy, M., Chauvin, G., Lagrange, A.-M., et al., 2014, A&A, 562, 127

Bonnefoy, M., Zurlo, A., Baudino, J.-L., et al., 2016, A&A, in press

Bontemps, S., André, P., Kaas, A. A., et al. 2001, A&A, 372, 173

Borucki, W. J., Koch, D., Jenkins, J., et al. 2009, Science, 325, 709

Borucki, W. J., Koch, D., Basri, G., et al. 2010, Science, 327, 977

Borucki, W. J., Koch, D. G., Basri, G., et al. 2011, ApJ, 728, 117

Boss, A. P. 2001, ApJ, 563, 367

Bouy, H., Martin, E.L., Brandner, W., & Bouvier, J. 2005, AJ, 129, 511

Bowler, B. P., Liu, M. C., Shkolnik, E. L., & Tamura, M. 2015, ApJS, 216, 7

Brandt, T. D., McElwain, M., Turner, E. L., et al., 2013, ApJ, 764, 183

Brandt, T.D., Kuzuhara, M., McElwain, M.W. et al. 2014, ApJ, 786, 1

Brandt, T. D., Rizzo, M., Groff, T., 2017, JATIS, 3, 8002

Brittain, S. D., Simon, T., Najita, J. R., & Rettig, T. W. 2007, ApJ, 659, 685

Bruderer, S., van der Marel, N., van Dishoeck, E. F., & van Kempen, T. A. 2014, A&A, 562, A26

Bryan, M., et al., 2016, ApJ, in press

Burrows, A., Hubbard, W. B., Lunine, J. I., Liebert, J., 2001, Review of Modern Physics, 73, 719

Burrows, A., Sudarsky, D., Hubeny, I., 2006, ApJ, 640, 1063

Calvet, N., D'Alessio, P., Watson, D. M., et al. 2005, ApJ, 630, L185

Canovas, H., Menard, F., Hales, A., Jordan, A., Schreiber, M., Casassus, S., Gledhill, T., & Pinte, C. 2013, A&A, 556, 123

Cardelli, J.A., Clayton, G.C., & Mathis, J.S. 1989, ApJ, 345, 245

Carson, J., Thalmann, C., Janson, M., et al. 2013, ApJ, 763, L32

Chabrier, G., Baraffe, I., Allard, F., & Hauschildt, P. 2000, ApJ, 542, 464

Clarke, C. J., Gendrin, A., & Sotomayor, M. 2001, MNRAS, 328, 485

Cody, A. M., Stauffer, J., Baglin, A., et al. 2014, AJ, 147, 82

Currie, T., Burrows, A., Itoh, Y., et al., 2011, ApJ, 729, 128

Currie, T., Debes, J. H., Rodigas, T. J., et al., 2012, ApJ, 760, L32

Currie, T., Burrows, A., Madhusudhan, N., et al., 2013, ApJ, 776, 15

Currie, T., Daemgen, S., Debes, J., et al. 2014, ApJ, 780, L30

Currie, T., Muto, T., Kudo, T., et al. 2014, ApJ, 796, LL30

Currie, T., Daemgen, S., Debes, J., Lafreniere, D., Itoh, Y., Jayawardhana, R., Ratzka, T., & Correia, S. 2014, ApJL, 780, 30

Currie, T., Burrows, A., Girard, J. H., et al. 2014, ApJ, 795, 133

Currie, T., Cloutier, R., Brittain, S., et al., 2015, ApJ, 814, L7

Currie, T., Cloutier, R., Grady, C., et al., 2015, ApJ, 814, L27

Currie, T., Lisse, C., Kuchner, M., et al., 2015, ApJ, 807, L7

Currie, T., Guyon, O., Tamura, M., et al., 2017a, ApJ, 836, L15

Currie, T., Brittain, S., Grady, C., et al., 2017b, RNAAS, 1, 40

Currie, T., Kasdin, N. J., Groff, T., et al., 2018, PASP, 130, 044505

Currie, T., Brandt, T. D., Uyama, T., et al., 2018, AJ, in press, arxiv:1810.09457

Cushing, M. C., Vacca, W. D., & Rayner, J. T. 2004, PASP, 116, 362

Cutri, R. M., & et al. 2012, VizieR Online Data Catalog, 2311, 0

Cutri, R. M., Skrutskie, M. F., van Dyk, S., et al. 2003, VizieR Online Data Catalog, 2246

D'Alessio, P., Calvet, N., Hartmann, L., Franco-Hernández, R., & Servín, H. 2006, ApJ, 638, 314

de Gregorio-Monsalvo, I., Ménard, F., Dent, W., et al. 2013, A&A, 557, A133

Debes, J. H., Poteet, C. A., Jang-Condell, H., et al. 2017, ApJ, 835, 205

De Rosa, R., Rameau, J., Patience, J., et al., 2016, ApJ, 824, 121

Devine, D., Grady, C. A., Kimble, R. A., et al. 2000, ApJ, 542, L115

Donehew, B., & Brittain, S. 2011, AJ, 141, 46

Dong, R., Rafikov, R., Zhu, Z., et al. 2012, ApJ, 750, 161

Doyle, L.R., Carter, J.A., Fabrycky, D.C. et al. 2011, Science, 333, 1602

Duchene, G. & Kraus, A. 2013, ARA&A, 51, 269

Dullemond, C. P., & Dominik, C. 2004, A&A, 421, 1075

Dullemond, C. P., & Dominik, C. 2004, Extrasolar Planets: Today and Tomorrow, 321, 361

Dullemond, C. P., & Dominik, C. 2005, A&A, 434, 971

Dupuy, T. J., & Liu, M. C. 2012, ApJS, 201, 19

Dupuy, T. J., Liu, M. C., Bowler, B. P., et al. 2010, ApJ, 721, 1725

Dupuy, T., Brandt, T. D., Kratter, K., Bowler, B. P., 2019, ApJ, 871, L4

Eisner, J. A., Monnier, J. D., Woillez, J., et al. 2010, ApJ, 718, 774

Ellerbroek, L. E., Podio, L., Dougados, C., et al. 2014, A&A, 563, A87

Espaillat, C., Calvet, N., D'Alessio, P., et al. 2007a, ApJ, 664, L111

Espaillat, C., Calvet, N., D'Alessio, P., Hernandez, J., Qi, C., Hartmann, L., Furlan, E., & Watson, D. 2007b, ApJL, 670, 135

Evans, N. J., II, Allen, L. E., Blake, G. A., et al. 2003, PASP, 115, 965

Evans, N. J., II, Dunham, M. M., Jørgensen, J. K., et al. 2009, ApJS, 181, 321

Fűrész, G., Hartmann, L. W., Megeath, S. T., Szentgyorgyi, A. H., & Hamden, E. T. 2008, ApJ, 676, 1109

Fabrycky, D. C., & Murray-Clay, R. A. 2010, ApJ, 710, 1408

Faherty, J. K., Riedel, A. R., Cruz, K. L., et al. 2016, arXiv:1605.07927

Fernandes, R. B., Long, Z. C., Pikhartova, M., et al. 2018, ApJ, 856, 103

Fischer, D. A., & Valenti, J. 2005, ApJ, 622, 1102

Follette, K. B., Tamura, M., Hashimoto, J., et al. 2013, ApJ, 767, 10

Follette, K. B., Grady, C. A., Swearingen, J. R., et al. 2015, ApJ, 798, 132

Fortney, J. J., Marley, M. S., Saumon, D., & Lodders, K. 2008, ApJ, 683, 1104

Fukagawa, M., Tamura, M., Itoh, Y., et al. 2006, ApJ, 636, L153

Fukagawa, M., Tamura, M., Itoh, Y., et al. 2010, PASJ, 62, 347

Günther, H. M., Schneider, P. C., & Li, Z.-Y. 2013, A&A, 552, A142

Gagne, J., Lafreniere, D., Doyon, r., Malo, L., & Artigau, E. 2014, ApJ, 783, 121

Gaia Collaboration, Prusti, T., de Bruijne, J. H. J., et al. 2016, A&A, 595, A1

Gaia Collaboration, Brown, A. G. A., Vallenari, A., et al. 2018, arXiv:1804.09365

Galicher, R., Marois, C., Macintosh, B., et al., 2011, ApJ, 739, L41

Garcia Lopez, R., Natta, A., Testi, L., & Habart, E. 2006, A&A, 459, 837

Garufi, A., Quanz, S. P., Schmid, H. M., et al. 2014, A&A, 568, A40

Garufi, A., Meeus, G., Benisty, M., et al. 2017, A&A, 603, A21

Gauza, B., Bejar, V.J.S., Perez-Garrido, A. et al. 2015, ApJ, 804, 96

Goebel, S., Currie, T., Guyon, O., et al., 2018, AJin press, arxiv:1810.09458

Gonzalez, G. 1997, MNRAS, 285, 403

Grady, C. A., Devine, D., Woodgate, B., et al. 2000, ApJ, 544, 895

Grady, C. A., Muto, T., Hashimoto, J., et al. 2013, ApJ, 762, 48

Grankin, K. N., Melnikov, S. Y., Bouvier, J., Herbst, W., & Shevchenko, V. S. 2007, A&A, 461, 183

Groff, T. D., Kasdin, N. J., Limbach, M., et al., 2015, SPIE, 9605, 1

Guidi, G., Tazzari, M., Testi, L., et al. 2016, A&A, 588, A112

Guidi, G., Ruane, G., Williams, J.P. et al. 2018, MNRAS, 479, 1505

Halif, R., Flusser, J., 1998. Numerically stable direct least squares fitting of ellipses. In: Proc. Sixth Intl Conf. Computer Graphics and Visualization, 125132

Hashimoto, J., Tamura, M., Muto, T., et al. 2011, ApJ, 729, L17

Hashimoto, J., Dong, R., Kudo, T., et al. 2012, ApJ, 758, L19

Hashimoto, J., Tsukagoshi, T., Brown, J. M., et al. 2015, ApJ, 799, 43

Hayano, Y., Takami, H., Guyon, O., et al. 2008, Proc. SPIE, 7015, 701510

Hayano, Y., Takami, H., Oya, S., et al. 2010, Proc. SPIE, 7736, 77360N

Hayashi, M., Hasegawa, T., Gatley, I., Garden, R., & Kaifu, N. 1985, MNRAS, 215, 31P

Hein Bertelsen, R. P., Kamp, I., van der Plas, G., et al. 2016, MNRAS, 458, 1466

Helou, G., & Walker, D. W. 1988, Infrared astronomical satellite (IRAS) catalogs and atlases. Volume 7, p.1-265, 7, 1

Herbig, G. H. 1950, ApJ, 111, 11

Herbig, G. H. 1960, ApJS, 4, 337

Herbig, G. H., & Bell, K. R. 1988, Third catalog of emission-line stars of the Orion population., by G.H. gerbig and K.R. Bell. Lick Observatory Bulletin #1111, Santa Cruz: Lick Observatory, Jun 1988, 90 p.,

Hinz, P., Rodigas, T.J., Kenworthy, M.A. et al. 2010, ApJ, 716, 417

Hodapp, K. W., Suzuki, R., Tamura, M., et al. 2008, Proc. SPIE, 7014, 701419

Howard, A. W., Johnson, J. A., Marcy, G. W., et al. 2010, ApJ, 721, 1467

Howard, A.W., Marcy, G.W., Bryson, S.T. et al. 2012, ApJS, 201, 15

Isella, A., Testi, L., Natta, A., Neri, R., Wilner, D., & Qi, C. 2007, A&A, 469, 213

Isella, A., Guidi, G., Testi, L., et al. 2016, Physical Review Letters, 117, 251101

Isella, A., Huang, J., Andrews, S. M., et al. 2018, ApJ, 869, L49

Jang-Condell, H., & Turner, N. J. 2012, ApJ, 749, 153

Jang-Condell, H., & Turner, N. J. 2013, ApJ, 772, 34

Johnson, J. A., Aller, K. M., Howard, A. W., & Crepp, J. R. 2010, PASP, 122, 905

Jones, B. F., & Walker, M. F. 1988, AJ, 95, 1755

Jones, B. F. 1970, AJ, 75, 563

Jovanovic, N., Martinache, F., Guyon, O., et al., 2015, PASP, 127, 890

Jovanovic, N., Guyon, O., Martinache, F., et al., 2015, ApJ, 813, L24

Kafka, S., 2018, Observations from the AAVSO International Database, https://www.aavso.org

Kalas, P.G., Graham, J.R., Chiang, E. et al. 2008, Science, 322, 1345

Keane, J. T., Pascucci, I., Espaillat, C., et al. 2014, ApJ, 787, 153

Keppler, M., Benisty, M., Müller, A., et al. 2018, A&A, 617, A44

Kim, S.-H., Martin, P. G., & Hendry, P. D. 1994, ApJ, 422, 164

Kim, K. H., Watson, D. M., Manoj, P., et al. 2013, ApJ, 769, 149

Knapp, G. R., Leggett, S. K., Fan, X., et al. 2004, AJ, 127, 3553

Kobayashi, H., Kawaguchi, N., Fujisawa, K. et al. 2000, in Proc. SPIE, Optical and IR Telescope Instrumentation and Detectors, eds M. Iye & A. F. Moorwood, Vol. 4008, 1056

Konishi, M., Matsuo, T., Yamamoto, K., et al. 2016, PASJ,

Kratter, K., & Lodato, G. 2016, ARA&A, 54, 271

Kraus, A. L., & Ireland, M. J. 2012, ApJ, 745, 5

Kusakabe, N., Grady, C. A., Sitko, M. L., et al. 2012, ApJ, 753, 153

Kuzuhara, M., Tamura, M., Kudo, T., et al. 2013, ApJ, 774, 11

Lafrenière, D., Marois, C., Doyon, R., Nadeau, D., & Artigau, É. 2007, ApJ, 660, 770

Lafrenière, D., Jayawardhana, R., & van Kerkwijk, M. H. 2008, ApJ, 689, L153

Lagrange, A.-M., Gratadour, D., Chauvin, G., et al. 2009, A&A, 493, L21

Lagrange, A.-M., Bonnefoy, M., Chauvin, G., et al., 2010, Science, 329, 57

Laughlin, G., Bodenheimer, P., & Adams, F.C. 2004, ApJL, 612, 73

Lazareff, B., Berger, J.-P., Kluska, J., et al. 2017, A&A, 599, A85

Leggett, S. K., Golimowski, D. A., Fan, X., et al. 2002, ApJ, 564, 452

Leggett, S. K., Burningham, B., Saumon, D., et al., 2010, ApJ, 710, 1627

Liu, M.C., Magnier, E. A¿, Neacon, N. R., et al., 2013, ApJ, 777, L20

Lomax, J. et al. 2015, ApJ, submitted

Low, C., & Lynden-Bell, D. 1976, MNRAS, 176, 367

Lucy, L. B. 1999, A&A, 344, 282

Macintosh, B., Graham, J. R., Ingraham, P., et al. 2014, Proceedings of the National Academy of Science, 111, 12661

Macintosh, B., Graham, J.R., Barman, T. et al. 2015, Science, 350, 64

Madhusudhan, N., Burrows, A., Currie, T., 2011, ApJ, 737, 34

Makarov, V. V., & Fabricius, C. 2001, A&A, 368, 866

Malo, L., Doyon, R., Lafreniere, D., et al. 2013, ApJ, 762, 88

Mamajek, E.E. 2008, AN, 329, 10

Marsh, K. A., Van Cleve, J. E., Mahoney, M. J., Hayward, T. L., & Houck, J. R. 1995, ApJ, 451, 777

Marley, M. S., Fortney, J. J., Hubickyj, O., Bodenheimer, P., Lissauer, J. J., 2007, ApJ, 655, 541

Marley, M., Saumon, D., Cushing, M., et al., 2012, ApJ, 754, 135

Marois, C., Lafreniére, D., Duyon, R., al., 2006, ApJ, 641, 556

Marois, C., Zuckerman, B., Konopacky, Q., Macintosh, B., Barman, T., 2010, Nature, 468, 1080

Marois, C., Correia, C., Veran, J.-P., Currie, T. 2014, Exploring the Formation and Evolution of Planetary Systems, Proceedings of the International Astronomical Union, IAU Symposium, Volume 299, pp. 48-49

Mawet, D., Milli, J., Wahhaj, Z., et al., 2014, ApJ, 792, 97

McClure, M. K., Furlan, E., Manoj, P., et al. 2010, ApJS, 188, 75

McMullin, J. P., Waters, B., Schiebel, D., Young, W., & Golap, K. 2007, Astronomical Data Analysis Software and Systems XVI, 376, 127

Meeus, G., Waters, L. B. F. M., Bouwman, J., et al. 2001, A&A, 365, 476

Meeus, G., Salyk, C., Bruderer, S., et al. 2013, A&A, 559, A84

Mendigutía, I., Calvet, N., Montesinos, B., et al. 2011, A&A, 535, A99

Mendigutía, I., Brittain, S., Eiroa, C., et al. 2013, ApJ, 776, 44

Min, M., Dullemond, C. P., Dominik, C., de Koter, A., & Hovenier, J. W. 2009, A&A, 497, 155

Monet, D. et al. 1998, VizieR Online Data Catalog, 1252, 0

Monnier, J. D., Harries, T. J., Aarnio, A., et al. 2017, ApJ, 838, 20

Montesinos, B., Eiroa, C., Mora, A., & Merín, B. 2009, A&A, 495, 901

Morales-Calderón, M., Stauffer, J. R., Hillenbrand, L. A., et al. 2011, ApJ, 733, 50

Muro-Arena, G. A., Dominik, C., Waters, L. B. F. M., et al. 2018, A&A, 614, A24

Muto, T., Grady, C. A., Hashimoto, J., et al. 2012, ApJ, 748, L22

Naud, M.-E., Artigau, E., Malo, L. et al. 2014, ApJ, 787, 5

Nielsen, E. L., Close, L. M., Biller, B. A., Masciadri, E., & Lenzen, R. 2008, ApJ, 674, 466-481

Nielsen, E. L., Liu, M. C., Wahhaj, Z., et al. 2013, ApJ, 776, 4

Ohta, Y., Fukagawa, M., Sitko, M. L., et al. 2016, PASJ, 68, 53

Pérez, L. M., Isella, A., Carpenter, J. M., & Chandler, C. J. 2014, ApJ, 783, LL13

Papaloizou, J. C. B. 2007, A&A, 463, 775

Perryman, M. A. C., Brown, A. G. A., Lebreton, Y., et al. 1998, A&A, 331, 81

Pikhartova, M., Sitko, M., In Preparation

Pinilla, P., Benisty, M., de Boer, J., et al. 2018, ApJ, 868, 85

Pinte, C., Ménard, F., Duchêne, G., & Bastien, P. 2006, A&A, 459, 797

Pinte, C., Price, D. P., Menard, F., eta l., 2018, ApJ, 860, L13

Pollack, J. B., Hubickyj, O., Bodenheimer, P., et al. 1996, Icarus, 124, 62

Pueyo, L., 2016, AJ, 824, 114

Qi, C., D'Alessio, P., Öberg, K. I., et al. 2011, ApJ, 740, 84

Qi, C., Öberg, K. I., Andrews, S. M., et al. 2015, ApJ, 813, 128

Quanz, S., Amara, A., Meyer, M. R., et al., 2013, ApJ, 766, L1

Quanz, S., Amara, A., Meyer, M., et al., 2015, ApJ, 807, 64

Radigan, J., Jayawardhana, R., Lafreniere, D. et al. 2013, ApJ, 778, 36

Raghavan, D., McAlister, H.A., Henry, T.J. et al. 2010, ApJS, 190, 1

Ratzka, T., Kohler, R., & Leinert, C. 2005, A&A, 437, 611

Rayner, J. T., Toomey, D. W., Onaka, P. M., et al. 2003, PASP, 115, 362

Reipurth, B. & Mikkola, S. 2015, AJ, 149, 145

Rich, E. A., Wisniewski, J. P., Currie, T., et al. 2018, arXiv:1811.07785

Robitaille, T. P. 2011, A&A, 536, A79

Rosenfeld, K.A., Andrews, S.A., Hughes, M.A. Wilner, D.J., & Qi, C. 2013, ApJ, 774, 16

Samus', N. N., Goranskii, V. P., Durlevich, O. V., et al. 2003, Astronomy Letters, 29, 468

Schmid, H. M., Joos, F., & Tschan, D. 2006, A&A, 452, 657

Schneider, G., Weinberger, A. J., Becklin, E. E., Debes, J. H., & Smith, B. A. 2009, AJ, 137, 53

Setterholm, B. R., Monnier, J. D., Davies, C. L., et al. 2018, ApJ, 869, 164

Shakura, N. I., & Sunyaev, R. A. 1973, A&A, 24, 337

Simon, M., Ghez, A.M., Leinert, C. et al. 1995, ApJ, 443, 625

Sitko, M. L., Carpenter, W. J., Kimes, R. L., et al. 2008, ApJ, 678, 1070

Skemer, A., Hinz, P.M., Esposito, S. et al. 2012, ApJ, 753, 14

Snellen, I. A. G., Brown, A. G. A, 2018, Nature Astronomy, 2, 883

Soummer, R., Pueyo, L., Larkin, J., 2012, ApJ, 755, L28

Sparks, W., Ford, H., 2002, ApJ, 578, 543

Spiegel, D. S., & Burrows, A. 2012, ApJ, 745, 174

Stone, J., et al., 2016, ApJŁ, 818, 12

Strom, K. M., Margulis, M., & Strom, S. E. 1989, ApJ, 346, L33

Strom, K. M., Strom, S. E., & Margulis, M. 1989, European Southern Observatory Conference and Workshop Proceedings, 33, 423

Strom, K. M., Strom, S. E., Edwards, S., Cabrit, S., & Skrutskie, M. F. 1989, AJ, 97, 1451

Suzuki, T. K., Muto, T., & Inutsuka, S.-i. 2010, ApJ, 718, 1289

Takami, M., Karr, J. L., Hashimoto, J., et al. 2013, ApJ, 772, 145

Takami, M., Hasegawa, Y., Muto, T., et al. 2014, ApJ, 795, 71

Takami, M., Fu, G., Liu, H.B. et al. 2018, ApJ, 864, 20

Tamura, M. 2009, in Exoplanets and Disks: Their Formation and Diversity, ed. T. Usuda, M. Tamura, & M. Ishii, AIP Conf Proc. 1158, 11

Tamura, M. 2016, Proceeding of the Japan Academy, Series B, 92, 45

Tannirkulam, A., Monnier, J.D., Millan-Gabet, R. et al. 2008, ApJ, 677 51

Teague, R., Bae, J., Bergin, E.A., Birnstiel, T., & Foreman-Mackey, D. 2018, ApJL, 860, 12

Thalmann, C., Carson, J., Janson, M., et al. 2009, ApJ, 707, L123

Thalmann, C., Grady, C. A., Goto, M., et al. 2010, ApJ, 718, L87

Thalmann, C., Desidera, S., Bonavita, M. et al. 2014, A&A, 572, 91

Thalmann, C., Mulders, G. D., Hodapp, K., et al. 2014, A&A, 566, AA51

Thalmann, C., Janson, M., Garufi, A., et al. 2016, ApJ, 828, L17

Todorov, K., Luhman, K. L., & McLeod, K. K. 2010, ApJ, 714, L84

Tsukagoshi, T., Momose, M., Hashimoto, J., et al. 2014, ApJ, 783, 90

Turner, N. J., Benisty, M., Dullemond, C. P., & Hirose, S. 2014, ApJ, 780, 42

Vacca, W. D., Cushing, M. C., & Rayner, J. T. 2003, PASP, 115, 389

van der Bliek, N.S., Manfroid, J., & Bouchet, P. 1996, A&AS, 119, 547

van der Marel, N. et al. 2014, Science, 340, 1199

van Leeuwen, F. 2007, A&A, 474, 653

Vigan, A., Bonnefoy, M., Ginski, C., et al. 2016, A&A, 587, A55

Vioque, M., Oudmaijer, R.D., Baines, D., Mendigutia, I., & Perez-Martinez, R. 2018, A&A, in press (astro-ph:1808.00476)

Wagner, K. R., Sitko, M. L., Grady, C. A., et al. 2015, ApJ, 798, 94

Wang, S., Hildebrand, R.H., & Hobbs, L.. et al. 2003, Proc SPIE, 4841, 1145

Wang, J., Graham, J., Dawson, R., et al., 2018, AJ, 156, 192

Wassell, E. J., Grady, C. A., Woodgate, B., Kimble, R. A., & Bruhweiler, F. C. 2006, ApJ, 650, 985

Whitney, B. A., Wood, K., Bjorkman, J. E., & Wolff, M. J. 2003, ApJ, 591, 1049

Whitney, B. A., Robitaille, T. P., Bjorkman, J. E., et al. 2013, ApJS, 207, 30

Wilking, B. A., Lebofsky, M. J., & Rieke, G. H. 1982, AJ, 87, 695

Wilking, B. A., Schwartz, R. D., & Blackwell, J. H. 1987, AJ, 94, 106

Williams, J. P., & Cieza, L. A. 2011, ARA&A, 49, 67

Wilson, J. C., Henderson, C. P., Herter, T. L., et al. 2004, Proc. SPIE, 5492, 1295

Winn, J.N. & Fabrycky, D.C. 2015, ARAA, 53, 409

Wisniewski, J. P., Clampin, M., Grady, C. A., et al. 2008, ApJ, 682, 548

Wolf, S., & Hillenbrand, L. A. 2003, ApJ, 596, 603

Wolk, S. J., & Walter, F. M. 1996, AJ, 111, 2066

Wood, K., Wolff, M. J., Bjorkman, J. E., & Whitney, B. 2002, ApJ, 564, 887

Wright, E. L., Eisenhardt, P. R. M., Mainzer, A. K., et al. 2010, AJ, 140, 1868-1881

Wright, J. T., Veras, D., Ford, E. B., et al. 2011, ApJ, 730, 93

Zhu, Z., Nelson, R. P., Hartmann, L., Espaillat, C., & Calvet, N. 2011, ApJ, 729, 47

Zhu, Z., Stone, J. M., & Rafikov, R. R. 2012, ApJ, 758, L42